

Montana Tech Library

Digital Commons @ Montana Tech

Graduate Theses & Non-Theses

Student Scholarship

Fall 2021

FABRICATION AND CHARACTERIZATION OF MANGANESE OXIDE SURFACES FROM POLYMER-BASED FIBER PRECURSORS

Molly C. Brockway

Follow this and additional works at: https://digitalcommons.mtech.edu/grad_rsch



Part of the [Materials Science and Engineering Commons](#), and the [Philosophy Commons](#)

FABRICATION AND CHARACTERIZATION OF MANGANESE OXIDE
SURFACES FROM POLYMER-BASED FIBER PRECURSORS

by

Molly C. Brockway

A dissertation submitted in partial fulfillment of the
requirements for the degree of

Doctor of Philosophy:
Materials Science

Montana Technological University

2021



FABRICATION AND CHARACTERIZATION OF MANGANESE OXIDE SURFACES
FROM POLYMER-BASED FIBER PRECURSORS

By

MOLLY CARRON BROCKWAY

B.S. Metallurgical and Materials Engineering, Montana Tech of the University of Montana,
Butte, MT, 2017

Dissertation
presented in partial fulfillment of the requirements
for the degree of

Doctor of Philosophy
in Materials Science

Montana Technological University
Butte, MT

Graduation Month and Year

Approved by:

Jack L. Skinner, Chair
Mechanical Engineering, Montana Technological University

David F. Bahr
Materials Engineering, Purdue University

Jerome P. Downey
Metallurgical and Materials Engineering, Montana Technological University

John D. Kirtley
Chemistry and Geochemistry, Montana Technological University

Atish J. Mitra
Mathematical Sciences, Montana Technological University

Rob A. Walker
Chemistry and Biochemistry, Montana State University

Angela Lueking, Dean
Montana Technological University Graduate School

Brockway, Molly, B.S. Metallurgical and Materials Engineering, 2017

Fabrication and Characterization of Manganese Oxide Surfaces from Polymer-Based Precursors

Chairperson: Jack L. Skinner

Supercapacitors are an energy storage technology combining properties of both capacitors and batteries to deliver high power and energy densities. Supercapacitors store charge through electrostatic and faradaic interactions between the electrode and ionic electrolyte. By improving the physical structure of electrodes, the interfacial area where energy storage occurs can be increased and electrochemical performance improved. New, fibrous, manganese oxide web-based structures tested for use as a supercapacitor electrode were fabricated by electrospinning and direct calcination of metal salt-containing polymer fibers, and the effects of fabrication parameters on electrochemical performance were investigated. Data show that high polymer concentrations and low oxide precursor concentrations during electrospinning form porous fibers with increased surface area, resulting in capacitance values up to 76 % greater than electrodes prepared with low polymer and high precursor concentrations. Post-electrospinning vapor melting treatments improved mechanical stability of the fiber mats to prevent delamination during calcination, increasing active mass of the prepared electrodes and improving performance by over 50 %. Calcining the structures for at least 4 h improves structural and electrical properties, increasing capacitance by up to 140 % compared to 2 h calcination, but extended calcination times past 4 h have no further beneficial effects.

Electrochemical impedance spectroscopy and linear sweep voltammetry on electrospun web electrodes are used to extract system parameters including double layer capacitance and charge transfer resistance. The measured parameters are combined with mathematical models to develop a theoretical description of discharge behavior in electrospun electrodes with varying fiber sizes, porosities, and materials. Modeled discharge curves are used to calculate power and energy densities over current densities ranging from 5 to 5000 A/g and predict that the electrospun electrodes should exhibit remarkably stable power density over a large range of energy densities. The geometry of a fabricated electrode is used to predict relationships between fiber diameter,

porosity, and surface area. The predictions are used to examine the effect of fiber diameter on the performance of an electrospun system. At low porosity, electrode energy density is maximized by minimizing void space in the electrode. Parametric manipulation of the model shows that improvements to electrode conductivity and the material's specific capacitance are promising, high-impact areas for optimization, while electrolyte conductivity and exchange current density have minimal effects. The model is also expanded to MnO_2 , Fe_2O_3 , Co_3O_4 , V_2O_5 , and WO_3 in order to predict suitability for use in electrospun web electrodes. The unexpectedly good performance of low-capacitance materials with high conductivities reveals the complex relationship between material parameters and electrospun electrode performance. The model is useful for predicting the effects of changing electrospun electrode parameters while decreasing the amount of necessary experimentation.

The work presented in this dissertation has demonstrated the suitability of electrospun structures for use as supercapacitor electrodes and provides insight into the fabrication conditions that improve capacitance. The model produced is a powerful tool for predicting materials and fiber sizes that are well-suited to the application, providing the potential for electrospun electrode fabrication methods to be expanded into higher-performing materials for improved low cost energy storage.

Keywords: Electrospinning, Nanofiber, Electrode, Supercapacitor, Manganese, Oxides

© COPYRIGHT

by

Molly C. Brockway

2021

All Rights Reserved

Dedication

This work is dedicated to my grandfather, who was the first scientist in my life. I know he would be proud of me.

Acknowledgements

Research was sponsored by the Combat Capabilities Development Command Army Research Laboratory and was accomplished under Cooperative Agreement Number W911NF-15-2-0020. The views and conclusions contained in this document are those of the authors and should not be interpreted as representing the official policies, either expressed or implied, of the Combat Capabilities Development Command Army Research Laboratory or the U.S. Government. The U.S. Government is authorized to reproduce and distribute reprints for Government purposes notwithstanding any copyright notation herein.

I would like to acknowledge Dr. Jack Skinner for his guidance and mentorship, as well as the many members of the Montana Tech Nanotechnology Laboratory that have come and/or gone during my time as a student. I would also like to acknowledge Gary Wyss for his frequent help and scheduling accommodations; Dr. Jerry Downey and Dr. Grant Wallace for their assistance with the flammable parts of my work; and all of the many faculty members who have provided expertise and encouragement over the past four years. Finally, I would like to acknowledge my family and partner for their support, without which I would undoubtedly have lacked the emotional fortitude to finish this.

Table of Contents

| | |
|---|------------|
| DEDICATION | VI |
| ACKNOWLEDGEMENTS | VII |
| LIST OF TABLES | XI |
| LIST OF FIGURES..... | XII |
| LIST OF EQUATIONS | XX |
| | |
| 1. INTRODUCTION | 1 |
| 1.1. Motivation..... | 1 |
| 1.1.1. Load Leveling / Power Smoothing | 3 |
| 1.1.2. Transportation..... | 3 |
| 1.2. Background | 4 |
| 1.2.1. Supercapacitors..... | 4 |
| 1.2.1.1. Operating Principles..... | 4 |
| 1.2.1.2. Electrode Materials | 8 |
| 1.2.2. Supercapacitor Energy Storage Models | 11 |
| 1.2.3. Electrospinning | 12 |
| 1.2.3.1. Fundamentals and operating principles..... | 12 |
| 1.2.3.2. Fiber Morphology..... | 15 |
| 1.2.3.3. Fiber Alignment..... | 16 |
| 1.2.3.4. Non-polymeric fibers | 18 |
| 1.3. Research Goals | 18 |
| | |
| 2. EXPERIMENTAL..... | 22 |
| 2.1. Electrospinning..... | 22 |
| 2.1.1. Single-composition | 22 |
| 2.1.2. Variable Composition | 23 |
| 2.2. Thermal Treatment | 25 |

| | | |
|------|--|----|
| 2.3. | <i>Variable Pressure Calcination</i> | 25 |
| 2.4. | <i>Post-Processing</i> | 26 |
| 2.5. | <i>Imaging</i> | 27 |
| | 2.5.1.1. Transmission Electron Microscopy (TEM) | 27 |
| | 2.5.1.2. Scanning Electron Microscopy (SEM) | 27 |
| 2.6. | <i>X-ray Diffraction (XRD)</i> | 28 |
| 2.7. | <i>Thermogravimetric Analysis</i> | 29 |
| 2.8. | <i>Electrochemistry</i> | 29 |
| | 2.8.1. Composite Electrodes | 29 |
| | 2.8.2. Freestanding Electrodes | 30 |
| | 2.8.2.1. Three Electrode Cell | 30 |
| | 2.8.2.2. Two-Electrode Symmetrical Cell | 30 |
| 2.9. | <i>Model Implementation</i> | 31 |
| 3. | RESULTS AND DISCUSSION | 32 |
| 3.1. | <i>Effects of Fabrication Parameters on Electrospun Electrodes</i> | 32 |
| | 3.1.1. Solution Composition | 36 |
| | 3.1.2. Electrospinning Deposition Time | 43 |
| | 3.1.3. Calcination Time | 45 |
| | 3.1.4. Multivariable Interactions | 49 |
| | 3.1.5. Comparison to Planar Structures | 51 |
| 3.2. | <i>Calcination Environment</i> | 53 |
| | 3.2.1. Environment Pressure | 53 |
| | 3.2.2. Environment Composition | 60 |
| 3.3. | <i>Post-Processing of Electrospun Electrodes</i> | 66 |
| | 3.3.1. Electrochemical Performance | 69 |
| | 3.3.2. Electrode Wettability | 72 |
| 3.4. | <i>Cycling Stability of Freestanding Electrospun Electrodes</i> | 74 |
| 3.5. | <i>Modeling</i> | 75 |

| | | |
|--------|---|-----|
| 3.5.1. | System Parameter Measurement | 76 |
| 3.5.2. | Model Derivation | 81 |
| 3.5.3. | Effect of Fiber Diameter | 87 |
| 3.5.4. | Modeling System Parameters | 95 |
| 3.5.5. | Modeling Energy Storage Oxides..... | 102 |
| 4. | CONCLUSIONS..... | 105 |
| 4.1. | <i>Electrode Fabrication Parameters</i> | 105 |
| 4.2. | <i>Electrospun Electrode Modeling</i> | 107 |
| 4.3. | <i>Future work</i> | 109 |
| 4.3.1. | Improving Electrode Performance | 109 |
| 4.3.2. | Improving Model Fidelity | 110 |
| 4.3.3. | Solid State Electrolytes | 111 |
| 4.3.4. | Fiber Alignment..... | 111 |
| 5. | REFERENCES CITED..... | 113 |
| 6. | APPENDIX A..... | 127 |
| 7. | APPENDIX B: R CODE FOR ELECTROSPUN FIBER MODELING | 131 |

List of Tables

| | |
|---|-----|
| Table I: Observed specific capacitances and approximate conductivities of supercapacitor electrode materials in aqueous electrolyte. Note that both properties are highly dependent on structure and processing, and conductivity can vary by several orders of magnitude. ²⁸ | 9 |
| Table II: Design matrix for examination of solution composition, electrospinning deposition time, and calcination time on freestanding web electrodes. Nineteen standards were required for a full 2^4 factorial design with three midpoints. | 23 |
| Table III: List of model parameters used to describe discharge of freestanding electrospun electrodes. | 86 |
| Table IV: Material parameters used to predict performance of energy storage oxides in freestanding electrospun electrodes. | 102 |
| Table V: Areal capacitance values of the nineteen standards tested, as described in the DOE table in the Experimental section. Each reported value is the average of three samples prepared for each standard. | 127 |
| Table VI: Assumed model values used for comparison of various metal oxide electrode materials. Separator porosity and thickness are taken from measured values; all other are based on the assumptions made in the exemplary model by Lin, et al. ⁵⁹ | 127 |

List of Figures

- Figure 1: Total annual anthropogenic greenhouse gas emissions for the years 1970-2010, measured in gigatonne of CO₂ equivalent per year. CO₂ emissions from fossil fuels and industrial processes account for well over half of global emissions yearly. Adapted from the Intergovernmental Panel on Climate Change's 2014 synthesis report.¹2
- Figure 2: Ragone plot of commonly used energy storage technologies, adapted from the *Handbook of Clean Energy Systems*.¹⁴5
- Figure 3: Schematic of electrochemical capacitor construction. (a) Uncharged capacitor, consisting of two electrodes separated by electrolyte and an ionically conducting separator. (b) Charged capacitor, with electrolyte ions migrated to the oppositely charged electrodes.7
- Figure 4: Schematic of a typical vertical electrospinning setup, adapted from Skinner, et al.⁸⁵ The syringe and collector may also be positioned horizontally without any significant modifications to the schematic setup.13
- Figure 5: Image showing Taylor cone, transition zone or stable region, and fiber jet. a_b and a_c represent the droplet radii at the respective locations, adapted from Han, Yarin & Reneker.⁸⁶14
- Figure 6: Examples of electrospun fibers with varying morphologies. (a) nanosprings fabricated by coaxial electrospinning of Nomex and thermoplastic polyurethane, adapted from Chen, et al.;⁸⁸ (b) beaded nanofibers produced from polystyrene in tetrahydrofuran, adapted from Lee, et al.;⁸⁹ (c) hollow polycaprolactone (PCL) nanofibers produced by coaxial electrospinning of PCL and polyethylene oxide, adapted from Dror, et al.;⁹⁰ (d)

- porous PCL microfibers produced by electrospinning at 75 % relative humidity, adapted from Nezarati, Eifert & Cosgriff-Hernandez.⁹¹15
- Figure 7: (a) Parallel plate electrodes and (b) rotating drum electrode used for aligned fiber deposition during electrospinning, adapted from Aminu, et al.¹⁰⁸17
- Figure 8: Scanning electron micrograph (SEM) of electrospun fiber mat electrode before (a) and after (b) thresholding used to measure porosity by calculating ratio of black pixels to total pixels on the thresholded image.....28
- Figure 9: Thermogravimetric analysis plot of as-received $\text{Mn}(\text{ac})_2$, as-received PVP, and as-electrospun composite fibers.....32
- Figure 10: X-ray diffractogram of powder-processed 1:1 PVP: $\text{Mn}(\text{ac})_2$ to determine phase of oxide produced during calcination of electrospun composite fibers. Planes associated with each major diffraction peak are labeled. The diffractograms for the 1:2.5 and 2.5:1 compositions are not presented due to lack of variation between conditions. The observed X-ray diffractogram is characteristic of Mn_2O_334
- Figure 11: A typical cyclic voltammogram under the examined conditions. Scan displayed is of electrode prepared from 8 % PVP/ 8 % $\text{Mn}(\text{ac})_2$, deposited for 30 min and calcined for 120 min. The inclined shape and lack of redox peaks are typical for all samples.35
- Figure 12: Scanning electron micrographs of as-electrospun PVP/ $\text{Mn}(\text{ac})_2$ composite fibers deposited for 30 min from solution composed of (A) 8 % PVP / 8 % $\text{Mn}(\text{ac})_2$, 69 nm average diameter; (B) 20 % PVP / 8 % $\text{Mn}(\text{ac})_2$, 340 nm average diameter; (C) 8 % PVP / 20 % $\text{Mn}(\text{ac})_2$, 162 nm average diameter; and (D) 20 % PVP / 20 % $\text{Mn}(\text{ac})_2$, 154 nm average diameter. All scale bars are 10 μm . As-spun fiber morphologies were not affected by deposition time, so the 10 min condition is not presented.37

Figure 13: Scanning electron micrographs of samples prepared with (A) 8 % PVP / 8 % Mn(ac)₂; (B) 20 % PVP / 8 % Mn(ac)₂; (C) 8 % PVP / 20 % Mn(ac)₂; and (D) 20 % PVP/ 20 % Mn(ac)₂, deposited for 30 min and calcined for 240 min. All scale bars are 10 μm. Trends exhibited by solution composition modification were consistent for the 10 min deposition and 120 min calcination conditions and are therefore not shown.....38

Figure 14: Detail of electrodes (A) prepared with 20% PVP and 20 % Mn(ac)₂, showing the slight porosity evident in nearly all the examined conditions; (B) prepared with 20 % PVP and 8 % Mn(ac)₂, with high porosity unique to the fibrous structures fabricated from low-Mn(ac)₂ electrospinning solutions. Scale bars are 2 μm.40

Figure 15: Graphical representation of the effect of PVP concentration on areal capacitance of electrospun Mn₂O₃ electrodes across multiple scan rates. Each data point is the average of eight conditions, with three measurements for each standard.41

Figure 16: Graphical representation of the effect of Mn(ac)₂ concentration on areal capacitance of electrospun Mn₂O₃ electrodes across multiple scan rates. Each data point is the average of eight conditions, with three measurements for each standard.42

Figure 17: Graphical representation of the effect of electrospinning deposition time on areal capacitance of electrospun Mn₂O₃ electrodes across multiple scan rates. Each data point is the average of eight conditions, with three measurements for each standard. ...44

Figure 18: Morphologies of samples prepared with 20 % PVP / 20 % Mn(ac)₂ electrospinning solutions, deposited for 10 min and calcined for (A) 120 min, and (B) 240 min. Samples electrospun from the same solution composition and deposited for 30 min display morphologies nearly identical to that observed in (B) and are therefore not presented. Scale bars are 10 μm.45

- Figure 19: Graphical representation of the effect of fiber calcination time on areal capacitance of electrospun Mn_2O_3 electrodes across multiple scan rates. Each data point is the average of eight conditions, with three measurements for each standard.46
- Figure 20: Effect of calcination time on areal capacitance of electrospun freestanding Mn_2O_3 electrodes fabricated from 20 % PVP/ 8 % $\text{Mn}(\text{ac})_2$ solutions. Areal capacitances were measured from cyclic voltammograms collected at 10 mV/s; error bars indicate 95 % confidence intervals.48
- Figure 21: TEM micrographs of electrospun fibers calcined at 600 °C for (a) 120 min and (b) 240 min. Calcination times longer than 240 min did not present visible distinction from (b).49
- Figure 22: XRD diffractogram for MnO_x prepared under different calcination pressures for 4 h calcination times, showing the effect of calcination pressure on composition.53
- Figure 23: Surface detail of electrospun MnO_x fibers calcined at 0.12 atm for (left) 0.5 h, (center) 2 h, and (right) 4 h, showing decrease in surface roughness after 0.5 h...54
- Figure 24: Electrospun MnO_x fibers calcined for 0.5 h at (left) 0.81 atm and (right) 0.12 atm. Calcination at atmospheric pressure results in a smooth fiber and round cross-section, while sub-atmospheric pressures result in wrinkled fiber surfaces and flattened cross-sections.55
- Figure 25: Cyclic voltammograms of fibers calcined for 0.5 h (left) and 4 h (right) at 0.26 atm, showing typical shape profiles observed. Electrode potential is vs Ag/AgCl.57
- Figure 26: Specific capacitance values of composite MnO_x electrodes prepared under varying conditions. Capacitance decreases with increasing calcination time and shows increased performance at a moderate calcination pressure.58

- Figure 27: Phase stability diagram for Mn-C-O at 450 °C. Diagram produced with StabCal thermodynamic equilibrium software.60
- Figure 28: SEM showing electrospun fibers calcined in pure oxygen for 30 min at 600 °C and then 5 h at 450 °C. Fibers exhibit smooth morphologies and minimal porosity. ...61
- Figure 29: SEMs showing manganese oxide electrodes after an 8 h calcination in O₂ at 450 °C. (a) Semi-melted fibers observed throughout fiber mat. (b) Fully melted film-like morphology observed at center of fiber mat. Similar morphologies were observed for fiber mats calcined with the same heating program in air.62
- Figure 30: SEM showing oblique view of mixed fiber-film morphology observed after long calcination in oxygen.63
- Figure 31: X-ray diffractograms of active material calcined in air and in a pure O₂ environment showing additional MnO₂ peaks (red circles).64
- Figure 32: Areal capacitance of electrospun electrodes calcined in air and oxygen for 8 h at 450 °C, as calculated from cyclic voltammograms. Error bars show 95 % confidence intervals.65
- Figure 33: SEMs of electrospun PVP/ Mn(ac)₂ fibers. Scale bars 10 μm. (A) as-spun, without further processing. (B) After hot-pressing treatment, showing fiber melting at junctions. (C) After vapor melting, with similar fiber melting. (D) After vapor melting and hot pressing, showing more complete melting of lower fiber layers from two melting steps.67
- Figure 34: Micrographs of calcined fiber mats after various post-electrospinning treatments. Scale bars 20 μm. (A) no post-spinning treatment; (B) hot pressed; (C) vapor-melted; (D) vapor-melted and hot-pressed.68

- Figure 35: Cyclic voltammogram of a vapor melted Mn_2O_3 fiber mat at varying scan rates. Trace shape is typical of that exhibited for all samples examined from all conditions. Potential is measured vs. Ag/AgCl reference electrode.70
- Figure 36: Goniometer images of water droplets on the calcined fiber mats. From top to bottom: untreated mat, 75.3° contact angle; vapor melted mat, 26.5° contact angle; hot pressed mat, 37.9° contact angle, vapor melted and hot-pressed mat, 47.1° contact angle.73
- Figure 37: Capacity of an electrospun Mn_2O_3 electrode over 100 cycles at 10 A/g, showing approximately 30 % capacity fading.....75
- Figure 38: Example of Bode plots describing an electrospun Mn_2O_3 electrode (points) and the models fit to describe them (lines). Blue data corresponds to the primary Y axis, Z_{mod} , and red data corresponds to the secondary axis, Z_{phz}76
- Figure 39: Nyquist plot describing an electrospun Mn_2O_3 electrode (points) with model overlaid (line).....77
- Figure 40: Equivalent circuit model used to describe electrospun electrodes for extracting variables from Bode and Nyquist plots.....78
- Figure 41: Example of a Tafel plot constructed for a freestanding Mn_2O_3 electrospun electrode. Line of best fit for linear region is shown as a dotted line, and the vertical line indicates the intercept at which exchange current density is measured.80
- Figure 42: Voltage of Mn_2O_3 electrospun electrodes as a function of state of charge, obtained by integrating the LSV curve, with the linear approximation displayed as a dashed line. State of charge, δ represents the content of oxidized or reduced Mn, as described in Equations 9 and 10.....82

- Figure 43: Micrograph images of electrospun Mn_2O_3 fibers. (a) SEM showing fiber porosity and layered structure. (b) TEM showing interior porosity of electrospun oxide fibers.88
- Figure 44: Discharge curves generated from the mathematical model for freestanding web electrodes with fiber diameters of 100, 160, and 220 nm at a current density of 1 A/g. Color available online.89
- Figure 45: (a) Time to fully discharge for electrodes with varying diameter, discharged from 1 V at a constant current density of 1 A/g; (b) discharge time for electrodes with varying fiber diameter, discharged from 1 V at a constant areal current of $20 \mu\text{A}/\text{cm}^2$ of active surface area.90
- Figure 46: Ragone plot for electrospun electrode with fiber diameter $D = 115 \text{ nm}$. Current densities used to generate plot range from 5 A/g to 5000 A/g.....92
- Figure 47: Discharge curve for modeled electrode with fiber diameter $D = 115 \text{ nm}$ vs. measured discharge curve from real electrode with average fiber diameter of 112 nm. Electrodes were discharge from 1 V at a current density of 10 A/g (left) and 1 A/g (right)...94
- Figure 48: Effect of exchange current density, i_0 (A/cm^2), on modelled discharge behavior. Plots generated at $D = 120 \text{ nm}$ and 1 A/g current density.96
- Figure 49: Effect of matrix conductivity, σ (S/cm), on modelled discharge curve. Plots generated at $D = 120 \text{ nm}$ and 1 A/g current density.....97
- Figure 50: Effect of electrolyte conductivity, κ_0 (S/cm), on discharge behavior. Model generated with $D = 120 \text{ nm}$ at 1 A/g current density.98
- Figure 51: Effect of DL capacitance per unit surface area, C_d (F/cm^2), on discharge curve. Model generated with $D = 120 \text{ nm}$ at 1 A/g current density.....100

- Figure 52: Effect of porosity (%) on discharge behavior. Model generated with $D = 120$ nm at 1 A/g current density; changes in porosity represent changes in total mass present as well as a reduction in average pore size.....101
- Figure 53: Predicted discharge curves for freestanding electrospun electrodes fabricated from different energy storage oxides. Discharge curves modeled with 150 nm fibers, 750 nm electrode thickness, and porosity of 0.5 assumed. Discharge is modeled at 1 mA/cm² current density.....104
- Figure 54: Experimental setup for testing composite electrodes in three-electrode cell. (a) Composite electrode in electrode holder with defined area. (b) Fully assembled three-electrode cell with composite working electrode, Ag/AgCl reference electrode, and Pt wire counter electrode.....128
- Figure 55: Two-electrode split cell used for testing freestanding web electrodes. Blue and green leads are working electrode and working sense, respectively, and red and white leads are counter and reference leads.....128
- Figure 56: Vapor chamber used for post-processing electrospun fiber mats. Absorbent substrate is used to increase relative humidity, which is monitored with the humidity and temperature sensor.129
- Figure 57: Manual hot press used for post-processing of electrospun fibers. To tighten uniformly, the press is turned 1/4 rotation after first contact with the sample.129
- Figure 58: Tube furnace setup used for calcination in oxygen environment. After flowing through the furnace, gases are flowed through a bubbler tube to prevent backflow into the tube and maintain pure oxygen atmosphere. For reactions in air, the bubbler is removed and the flange vents are opened to the ambient atmosphere.....130

List of Equations

| | |
|---------------------|----|
| Equation (1) | 35 |
| Equation (2) | 57 |
| Equation (3) | 78 |
| Equation (4) | 78 |
| Equation (5) | 78 |
| Equation (6) | 79 |
| Equation (7) | 81 |
| Equation (8) | 81 |
| Equation (9) | 81 |
| Equation (10) | 81 |
| Equation (11) | 81 |
| Equation (12) | 82 |
| Equation (13) | 83 |
| Equation (14) | 83 |
| Equation (15) | 83 |
| Equation (16) | 83 |
| Equation (17) | 83 |
| Equation (18) | 84 |
| Equation (19) | 84 |
| Equation (20) | 84 |
| Equation (21) | 84 |

| | |
|---------------------|----|
| Equation (22) | 84 |
| Equation (23) | 85 |
| Equation (24) | 85 |
| Equation (25) | 85 |
| Equation (26) | 86 |
| Equation (27) | 86 |
| Equation (28) | 86 |
| Equation (29) | 92 |
| Equation (30) | 92 |
| Equation (31) | 92 |
| Equation (32) | 98 |

1. Introduction

1.1. Motivation

According to the 2014 climate change report by the Intergovernmental Panel on Climate Change (IPCC), a pattern of “robust multi-decadal warming” has contributed significantly to ocean acidification, rising sea levels, ice cap and sheet shrinkage, and melting permafrost.¹ Increased greenhouse gas emissions due to population and economic growth are considered to have substantially contributed to the observed changes in Earth’s climate. The IPCC predicts that continuing greenhouse gas emissions without mitigation will continue to cause “long-lasting changes in all components of the climate system, increasing the likelihood of severe, pervasive, and irreversible impacts for people and ecosystems.”

With or without intervention, oceans will continue to rise, warm, and acidify, and extreme weather events such as droughts and hurricanes will occur more frequently and with greater intensity.² Flora and fauna will increasingly face risk of extinction, especially in the marine landscape. Projections predict that by the mid-21st century, increased food demand from population growth will combine with negatively impacted crop and fishery yields to cause and exacerbate global food insecurity, with additionally reduced water availability in dry subtropical regions. Even if greenhouse gas emissions are completely halted, many aspects of climate change and its impacts will continue for centuries. Clearly, a reduction in greenhouse gas emissions is imperative for preservation of the planet and protection of future generations. CO₂ from burning fossil fuels makes up over half of the annual human contribution to greenhouse gas emissions (Figure 1).

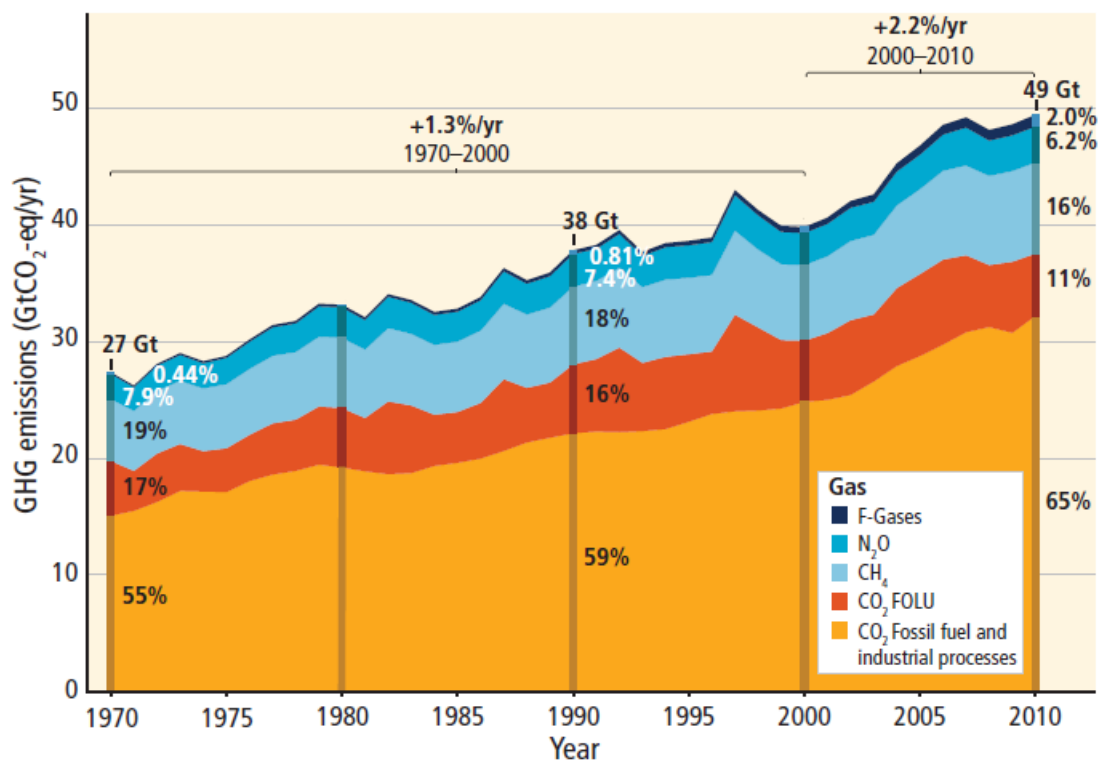


Figure 1: Total annual anthropogenic greenhouse gas emissions for the years 1970-2010, measured in gigatonne of CO₂ equivalent per year. CO₂ emissions from fossil fuels and industrial processes account for well over half of global emissions yearly. Adapted from the Intergovernmental Panel on Climate Change's 2014 synthesis report.¹

As such, innovation in environmentally sound technologies is an essential facet of reducing the carbon intensity of energy consumption and production in order to mitigate climate change and its effects. In 2018, renewable energy sources made up only around 11 % of the US's energy consumption and 15 % globally.³ For electricity generation, the figures rise to 17 % and 28 %, respectively. To increase both figures, it is necessary to implement greener technologies both in electricity generation, which accounts for over half of the annual anthropogenic greenhouse gas emissions, and in transportation, which generates over 30 % of US greenhouse gas emissions.¹

1.1.1. Load Leveling / Power Smoothing

Inexhaustible renewable energy sources such as wind, wave, and solar power will play an essential role in reducing global reliance on fossil fuels. Solar energy experiences a natural oscillation with the day/night cycle, and wind and wave energy generation are inconsistent and highly variable.⁴⁻⁶ Power fluctuations lead to grid frequency fluctuations, causing poor power quality, instability in the power system, and potential interruptions in energy delivery.⁷ To reduce the impact of wind and wave power fluctuations, power smoothing systems are used to attenuate the fast variation in supplied power from renewable resources.^{5,6,8} Supercapacitors are well-suited to power smoothing because of the requirement for fast charge and discharge cycles,⁷ allowing energy to be supplied steadily and continuously. Power smoothing systems employing supercapacitors can store large amounts of power per weight, but have typically short storage time of around 30-60 s,⁶ which is sufficient to smooth frequency fluctuations, but cannot maintain solar-provided power overnight. Instead, supercapacitors are used in hybrid energy storage systems that integrate long-term battery or pressure-based storage with the fast oscillation smoothing of supercapacitors.⁹

1.1.2. Transportation

Hybrid electric vehicles, plug-in hybrids, and full electric vehicles reduce fuel consumption and transport-based greenhouse gas emissions, which is an essential component of slowing the effects of climate change.^{1,9} In vehicles with alternative propulsion systems, the internal combustion engine is supplemented or replaced by supercapacitors or capacitor/battery hybrid electric systems. Wasted energy from braking and shock absorption is harvested, stored, and reapplied to the propulsion system, where the short time requirements of acceleration and deceleration find supercapacitors particularly advantageous.¹⁰ Beyond personal vehicles,

supercapacitors also have regenerative braking applications for rail transport and other forms of public transportation.⁹ Current versions of supercapacitors used in hybrid and electric vehicles are primarily carbon-based, which have limited cell voltages and operating temperatures.¹¹ Consequently, a great deal of research is focusing on alternative supercapacitor materials and structures that can provide high performance while lowering costs.

1.2. Background

1.2.1. Supercapacitors

1.2.1.1. Operating Principles

Supercapacitors, also known as ultracapacitors, electrochemical capacitors, or electric double-layer capacitors, were first developed in the 1960s and 1970s, with more thorough development occurring in the 1990s.¹² In the mid-2000s, porous carbon-based supercapacitors achieved sufficiently high performance to allow their implementation in consumer products and backup power supplies for electronics.^{13,14} Supercapacitors combine the high energy density of batteries with the power density of electrolytic capacitors to bridge the gap between the two technologies (Figure 2).

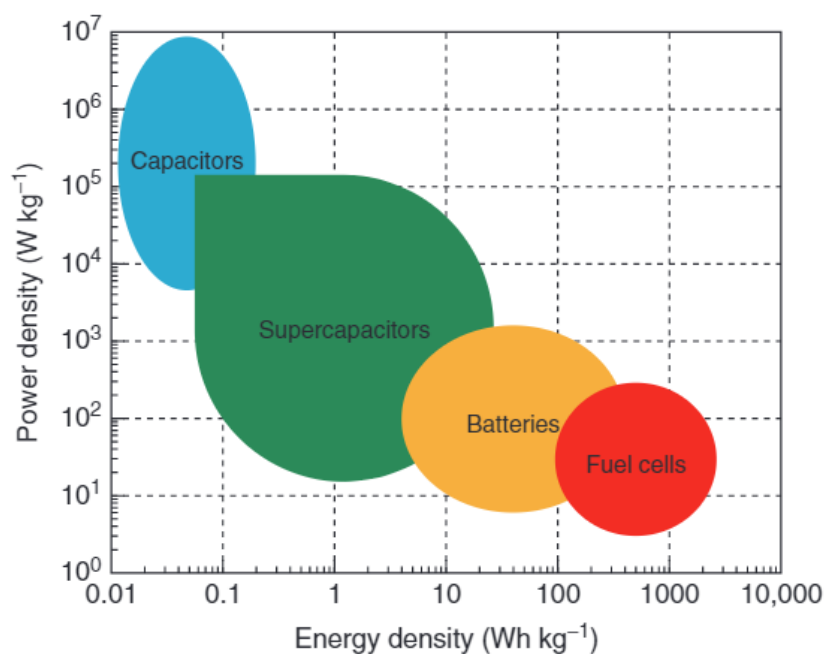


Figure 2: Ragone plot of commonly used energy storage technologies, adapted from the *Handbook of Clean Energy Systems*.¹⁴

In a Ragone plot, the power densities and energy densities of an energy storage device are plotted to compare their total capacity (energy density) and rate capacity (power density). For a generalized Ragone plot such as the one in Figure 2, the general characteristics of different energy storage technologies can be compared. Traditional capacitors have high power densities due to extremely fast discharge capabilities, but low energy densities. Fuel cells and batteries are slow to charge and discharge, but can store large amounts of energy. Supercapacitors have a wide range of potential energy and power densities, but generally possess higher energy densities than capacitors with greater power densities than batteries and fuel cells. Beyond their high power and energy densities, supercapacitors have exceedingly long cycling lives. Because energy storage does not involve chemical reactions or ion intercalation/deintercalation, supercapacitors can withstand millions of cycles before capacity fading becomes debilitating.¹⁵ They also dissipate heat effectively, preventing the thermal runaway issues that plague batteries

in many applications.¹¹ Supercapacitors are capable of operating effectively within a far wider temperature range than batteries, with high power performance down to $-40\text{ }^{\circ}\text{C}$.¹⁶ However, supercapacitors are still unable to provide the energy density of current-generation batteries, seeing them frequently combined into hybrid energy storage systems rather than used individually.

Supercapacitor cells consist of two electrodes separated by an ionically conductive, electronically insulating separator (Figure 3a). An ionic electrolyte soaks the separator and wets the electrode surfaces, creating a conductive pathway between the halves of the cell. The electrodes can be the same (for a symmetric cell) or different, known as an asymmetric cell. When a voltage is applied across the two terminals of the supercapacitor cell, a positive charge is generated on one electrode surface (cathode) and a negative charge on the other (anode). Correspondingly, negative ions in the electrolyte migrate to the cathode and positive ions to the anode, where they are held to the surface by electrostatic interactions (Figure 3b).

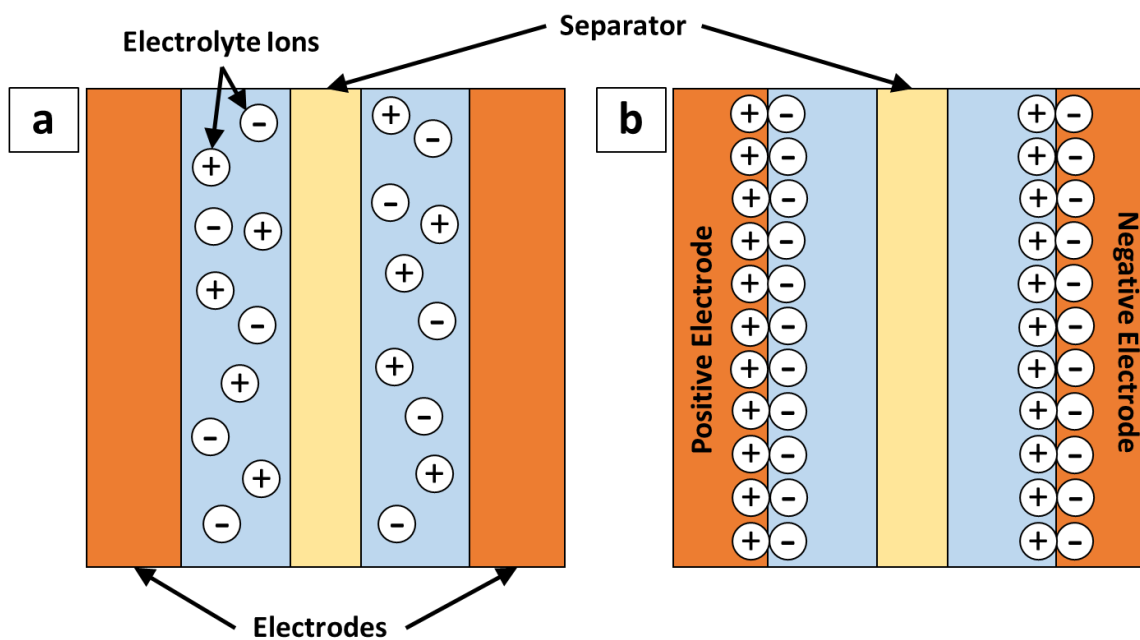


Figure 3: Schematic of electrochemical capacitor construction. (a) Uncharged capacitor, consisting of two electrodes separated by electrolyte and an ionically conducting separator. (b) Charged capacitor, with electrolyte ions migrated to the oppositely charged electrodes.

Upon reversal of the applied polarity, energy discharge is rapid as the ions diffuse from the surface. Because energy is stored as a surface charge, specific surface area of the electrode is paramount to defining the maximum energy density of the electrodes. In addition to simple electrostatic interaction, some electrode materials also exhibit pseudocapacitance, wherein faradaic exchange occurs between the electrolyte and electrode surface. The reactions are fast and highly reversible and differ from the redox reactions observed in batteries by their restriction to surface interactions, without ion intercalation and deintercalation. Pseudocapacitance can increase the energy density of a supercapacitor by 10-100 times, but results in slower charging and discharging due to the relatively slower kinetics of faradaic exchange, as well as shorter cycling life due to dimensional changes from swelling and shrinking caused by modifications to the surface lattice.^{17,18} As the mechanism of energy storage becomes more battery-like, the

overall characteristics of the supercapacitor cell do as well. Intrinsic pseudocapacitance is a material quality observed in a number of transition metal oxides, including RuO_2 ,¹⁹ MnO_2 ,^{20,21} Fe_3O_4 ,²² V_2O_5 ,²³ and Co_3O_4 .²⁴

1.2.1.2. Electrode Materials

Since supercapacitors were developed for commercial use, carbon has been the most widely used electrode material, owing to its relatively low cost and ease of production.¹⁵ Activated carbons with high porosity and specific surface area are easily produced, which is ideal for energy storage applications as it provides a greater number of energy storage sites. However, activated carbons have shown limited capacitance even with optimized porosity, as the entire surface area is not utilized for capacitive energy storage.²⁵ To further improve supercapacitor performance, other carbon-based electrode materials have been closely investigated. Carbide derived carbons are highly tunable structures prepared by extracting metal from carbide precursor structures, allowing for precise control over pore size and surface functionalization.^{26,27} Carbon nanotubes and nanofibers have high electrical conductivities and mesoporous surfaces, and can be grown directly onto a charge collecting substrate, minimizing contact resistance of the electrode and enhancing performance. However, the specific surface area of carbon nanotubes is far lower than that of either activated carbon or carbide-derived carbons, leading to lower overall capacitance.²⁸ Graphene has also been investigated for supercapacitor electrodes and demonstrates good flexibility; chemical, thermal, and electrical stability; large surface area; and surface functionalizability for induction of pseudocapacitance.²⁹ However, it has a propensity to re-stack, causing irreversible capacity loss due to decreased conductivity and surface area.

Metal oxides are another suitable and highly attractive class of material for supercapacitor electrodes as they possess high specific capacitances and conductivities in the semiconducting to metallic range (Table I). One of the most deeply explored oxides is RuO₂, which has the highest specific capacitance measured among supercapacitor electrode materials. It is highly pseudocapacitive, with approximately 90 % of its energy storage originating from faradaic reactions with the electrolyte.³⁰ RuO₂ is thermally and electrically stable, highly conductive, and physically robust.³¹ However, it is also toxic, expensive, and performs best in a strongly acidic electrolyte, severely limiting its utility for widespread implementation.³² NiO films have demonstrated capacitances similar to activated carbon with long cycling lives, but have limited voltage stability windows, limiting it to use as a cathode in asymmetrical supercapacitors.^{33,34} Cobalt oxides, both as crystalline Co₃O₄ and amorphous CoO_x, show similar performance to NiO and carbon-based structures but have wider operating voltage windows, allowing them expanded utility as either anodes or a cathodes.^{35,36} Vanadium oxides, including V₂O₅ and V₃O₇, demonstrate similar capacitances to nickel and cobalt oxides, but with enhanced stability at high charging and discharging rates, making them attractive for high-power applications.²³

Table I: Observed specific capacitances and approximate conductivities of supercapacitor electrode materials in aqueous electrolyte. Note that both properties are highly dependent on structure and processing, and conductivity can vary by several orders of magnitude.²⁸

| | Material | Specific capacitance (F/g) | Conductivity (S/cm) |
|---------------------|---|----------------------------|--|
| Carbons | Activated Carbon | 300 ²⁸ | 10 ⁻⁴ - 10 ³⁷ |
| | CDCs | 220 ²⁷ | ~ 5 ²⁷ |
| | CNTs | 180 ²⁸ | 10 ⁴ - 10 ⁵ ³⁸ |
| | Graphene | 135 ²⁹ | 550 ³⁹ |
| Metal Oxides | RuO ₂ | 1580 ⁴⁰ | 300 ⁴¹ |
| | NiO | 200 ³³ | 10 ⁻⁵ - 10 ⁻² ^{42,43} |
| | Co ₃ O ₄ , CoO _x | ~165 ^{35,36} | 10 ⁻⁹ - 10 ⁻⁶ ⁴⁴ |

| | | | |
|--|--------------------------------|-------------------------|---|
| | VO _x | 167 ²³ | 10 ⁻⁴ - 30 ⁴⁵ |
| | MnO ₂ | 1370 ²¹ | 10 ⁻⁵ - 10 ⁻⁴ ⁴⁶ |
| | Mn ₂ O ₃ | 600 ⁴⁷ | 10 ⁻⁵ ⁴⁸ |
| | Mn ₃ O ₄ | 200 – 600 ⁴⁹ | 10 ⁻⁷ – 10 ⁻⁸ ⁵⁰ |

Aside from RuO₂, manganese oxides are the some of the most widely investigated metal oxides for supercapacitor electrodes.^{15,51} Manganese is naturally abundant, inexpensive, and biologically and environmentally benign. Combined with their relatively good capacitive performances, manganese oxides appear promising for low cost, high-performance supercapacitors. Manganese can exist in oxidation states ranging from Mn²⁺ to Mn⁷⁺, and is stable in many phases, including MnO, MnO₂, Mn₂O₃, Mn₃O₄, Mn₅O₈, and others. MnO₂ holds the most promise for supercapacitor applications, with theoretical capacitances of around 1300 F/g.²¹ With an oxidation state of +4, the manganese in MnO₂ can undergo two oxidation or reduction steps (to Mn²⁺ or Mn⁶⁺), leading to a high degree of potential pseudocapacitance through electron exchange. Compared to MnO₂, Mn₂O₃ has a lower theoretical capacitance of around 600 F/g,^{47,52} owing to lower conductivity and less potential for faradaic exchange, as only one reduction is possible (Mn³⁺ to Mn²⁺). Mn₃O₄ has a mixed Mn³⁺/Mn²⁺ valence, resulting in the least possible pseudocapacitance, as Mn²⁺ cannot be further reduced. Nevertheless, ease of fabrication makes both Mn₂O₃ and Mn₃O₄ attractive for low-cost energy storage.

As semiconductors, manganese oxides are limited by low intrinsic conductivities on the order of 10⁻³ S/m.^{48,53} Poor electrical conductivity detrimentally affects supercapacitor electrode performance by limiting solid state diffusion rates of electrons and ions within the structure.^{54,55} Especially at fast cycling rates, the limited diffusion leads to ineffective charge generation on the electrode surface, preventing full utilization of the voltage range applied.

1.2.2. Supercapacitor Energy Storage Models

Modeling of nanostructured and porous metal oxide supercapacitors has been extensively performed, as accurate simulations of the structures and processes are essential to understanding and improving performance. In 1975, Tiedemann and Newman presented an early model for the double-layer charging behavior of porous lead oxide electrodes.⁵⁶ Later, Srinivasan and Wiedner examined the effects of cell design and operation parameters including electrode thickness, electrode and electrolyte resistances, temperature, and current density on power and energy densities of porous electrodes.⁵⁷ To introduce faradaic reactions into capacitive systems, Pillay and Newman modeled the effects of side reactions on charging and cycling of porous electrodes.⁵⁸

Lin's first model combining pseudocapacitive and double layer processes in a porous metal oxide supercapacitor structure has provided the basis for many further models of metal oxide supercapacitor systems.⁵⁹ The Lin model has been expanded upon by application to oxide/carbon composite systems with proton diffusion effects;^{60,61} asymmetrical supercapacitors;⁶²⁻⁶⁴ hybrid battery/supercapacitor systems;⁶⁵⁻⁶⁷ varying geometries including nanorods,⁶⁸ interdigitated electrodes,⁶⁹ and changes in electrode thickness and porosity;⁷⁰ and to account for self-discharge and side reactions.^{71,72} Other models integrate more complex descriptions of double-layer capacitance to accurately account for ion interactions in the electrolyte and with the electrode surface⁷³ or describe moving reaction fronts through the electrode body.⁷⁴ Conversely, some research has also focused on providing simplified models for easier use.^{75,76}

Most models of supercapacitor charging and discharging utilize hydrous RuO₂, carbon, or RuO₂-carbon composite electrode materials, and to date very few models have been published

for other systems. Hao et al. (2015) produced a model for an asymmetric lithium manganese oxide/ activated carbon supercapacitor, which was unique in its treatment of an asymmetric system as previous models examined only a single electrode of a symmetrical system and assumed mirrored behavior at the other electrode.⁷⁷ The asymmetrical model is important not only for asymmetric supercapacitors but also for electrode materials that have different affinities for positive or negative polarization, and may be an important step towards producing realistic models for both symmetric and asymmetric systems.

A common aspect of analytical models developed to describe supercapacitor behavior is lack of integration with experimental results. Many models are verified by comparison to other theoretical results and use only assumed values that may not describe the system realistically. Several models have been compared to or verified against experimental results^{70,78–80} or use values derived from experimental results,^{81,82} but there is still a lack of widespread mixing between theoretical and experimental models for describing metal oxide-based supercapacitor behavior.

1.2.3. Electrospinning

1.2.3.1. Fundamentals and operating principles

Electrospinning is a polymer processing technique used for fabrication of nano- to micro-scale fibers. It was first patented in 1930⁸³ and since then has been used in many fields including biotechnology, pharmaceuticals, electronics, environmental engineering, textiles, and energy storage and conversion.⁸⁴ Electrospun fibers offer supremely high specific surface areas, tunable fiber size and porosity, and flexibility in polymer selection, making it attractive across a wide range of applications due to its enormous diversity in products. Electrospinning uses electrostatic forces to form fibers from polymer solutions (solution electrospinning) or melted

polymer (melt electrospinning). The polymer solution or melt is held in a syringe with a metallic spinneret through which the polymer is dispensed. The syringe is positioned some distance from a collector surface, and a high-strength electric field is applied between the spinneret and collector. A schematic of a typical electrospinning setup is presented in Figure 4.

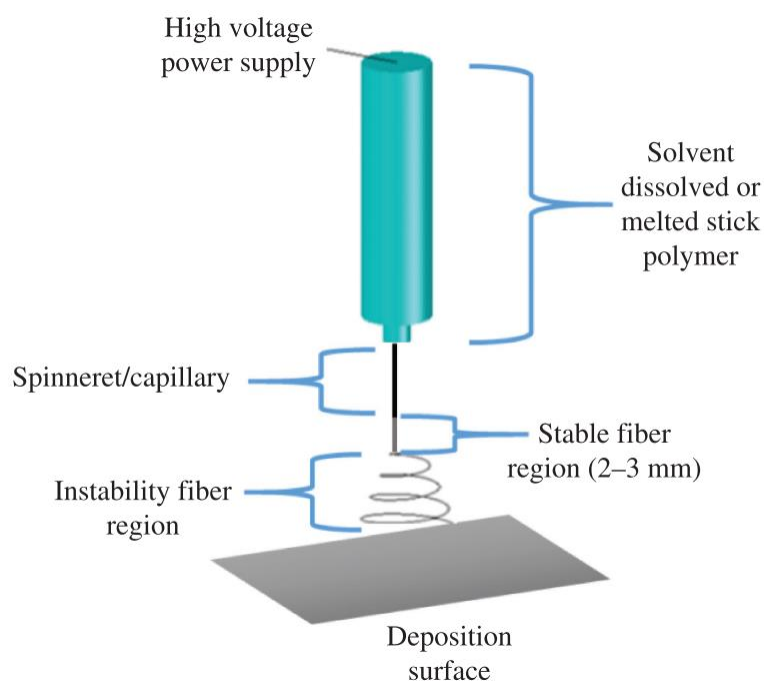


Figure 4: Schematic of a typical vertical electrospinning setup, adapted from Skinner, et al.⁸⁵ The syringe and collector may also be positioned horizontally without any significant modifications to the schematic setup.

The polymer solution or melt is extruded from the spinneret into the electric field, where it forms a droplet at the tip of the spinneret. Electrical charge builds up on the surface of the polymer droplet from the voltage differential between the deposition surface and spinneret. When the charge reaches a sufficient magnitude for the electrostatic forces between the charged droplet and the deposition surface to overcome the surface tension of the droplet, the polymer is elongated into a Taylor cone and further reduced to a micro- or nanoscale jet (Figure 5).

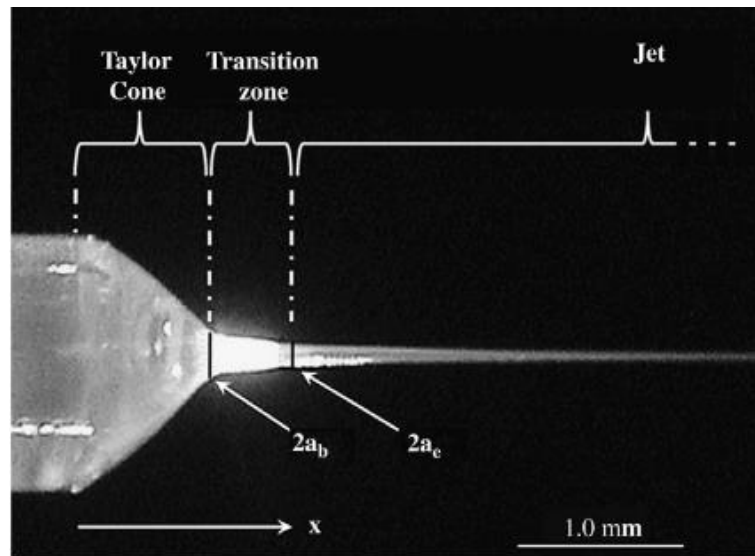


Figure 5: Image showing Taylor cone, transition zone or stable region, and fiber jet. a_b and a_e represent the droplet radii at the respective locations, adapted from Han, Yarin & Reneker.⁸⁶

The fiber jet exists in a stable region for a short distance before entering the whipping region, where solvent evaporation decreases the fiber diameter and radial charge repulsion among the polymer chains becomes dominant.^{85,87} The fibers are whipped chaotically about the jet axis and pulled towards the collector, which is held at the opposite polarity to the spinneret. As the jet travels between the spinneret and collector, the solvent evaporates or the melted polymer cools, and a solid polymer fiber is deposited.

Electrospinning has been effectively applied to an enormous number of natural and synthetic polymers, as well as copolymers and polymer blends. The process is controlled by several parameters, including polymer type and molecular weight, solvent composition and concentration (or temperature for melt electrospinning), separation distance between the spinneret and collector, electric field strength, type or geometry of the collector, and ambient temperature and humidity. Manipulation of the process parameters allows for tunability of fiber composition, size, packing density, alignment, and morphology.

1.2.3.2. Fiber Morphology

Many electrospun fibers exhibit smooth morphologies with circular cross-sections, but electrospinning parameters can be manipulated to produce fibers with wide-ranging morphologies (Figure 6).

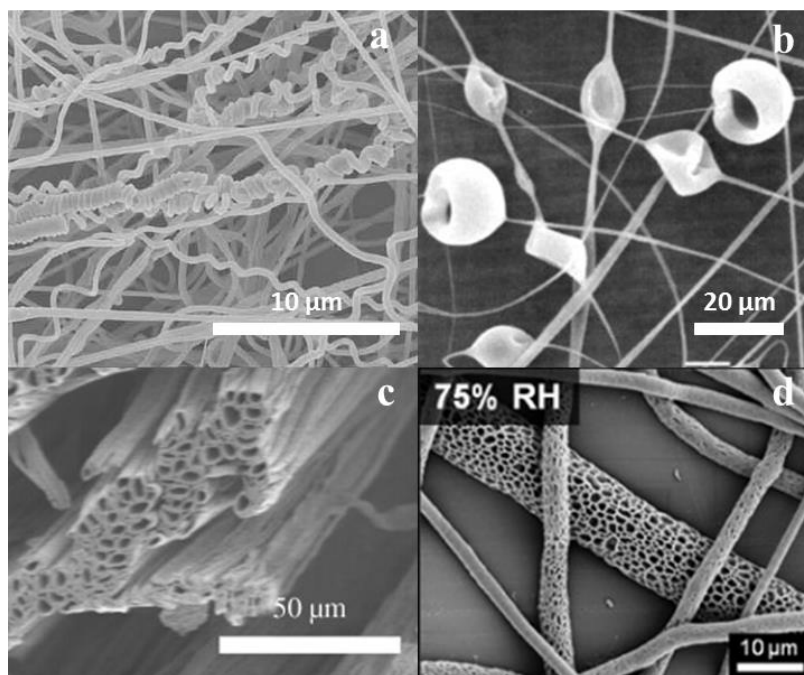


Figure 6: Examples of electrospun fibers with varying morphologies. (a) nanosprings fabricated by coaxial electrospinning of Nomex and thermoplastic polyurethane, adapted from Chen, et al.;⁸⁸ (b) beaded nanofibers produced from polystyrene in tetrahydrofuran, adapted from Lee, et al.;⁸⁹ (c) hollow polycaprolactone (PCL) nanofibers produced by coaxial electrospinning of PCL and polyethylene oxide, adapted from Dror, et al.;⁹⁰ (d) porous PCL microfibers produced by electrospinning at 75 % relative humidity, adapted from Nezarati, Eifert & Cosgriff-Hernandez.⁹¹

Fiber morphology and size are affected by all electrospinning parameters. Solution composition (especially polymer type, molecular weight, and solution concentration) has strong effects on fiber size and morphology. Beads are common with very low solution viscosities resulting from low molecular weight and/or concentration.⁹²⁻⁹⁴ As solution viscosity increases,

the beads change from spherical in shape to elongated, before disappearing entirely. Fiber diameter increases alongside viscosity, up to the point where viscosity becomes so high that the electrostatic forces induced in the polymer can no longer overcome the surface tension of the droplet and electrospinning becomes impossible. Beading may also occur if there is an imbalance between separation distance and applied voltage, with separation being too small or large for the polymer solution and applied voltage, or voltage too high for the separation distance.^{84,95,96}

Fiber diameter can also be controlled with applied voltage, flow rate, or temperature. Increasing the applied voltage generally decreases fiber diameter by causing greater electrostatic force within the fibers, leading to more fiber stretching.^{97,98} However, for some polymers the effect can be negligible or even opposite.^{99,100} Polymer flow rate controls the material deposition rate, with slower feed rates allowing longer times for solvent evaporation and lower fiber diameters.^{101,102} Increases in ambient temperature cause decreased fiber diameter owing to the inverse relationship between temperature and viscosity, with lower viscosities resulting in smaller fiber diameter.^{103,104}

1.2.3.3. Fiber Alignment

For certain applications such as tissue engineering,¹⁰⁵ composite reinforcement,¹⁰⁶ or device fabrication,¹⁰⁷ uni- or multi-axial fiber alignment can be highly desirable due to unique mechanical, optical, electrical, and biological properties. With a flat plate collector, the fibers whip chaotically about the axis extending from the spinneret tip to the collector plate, resulting in random deposition. However, the deposition pattern can be controlled with modifications to the collector. Two common configurations for fabricating aligned fibers are the rotating drum collector and parallel plate electrodes (Figure 7).

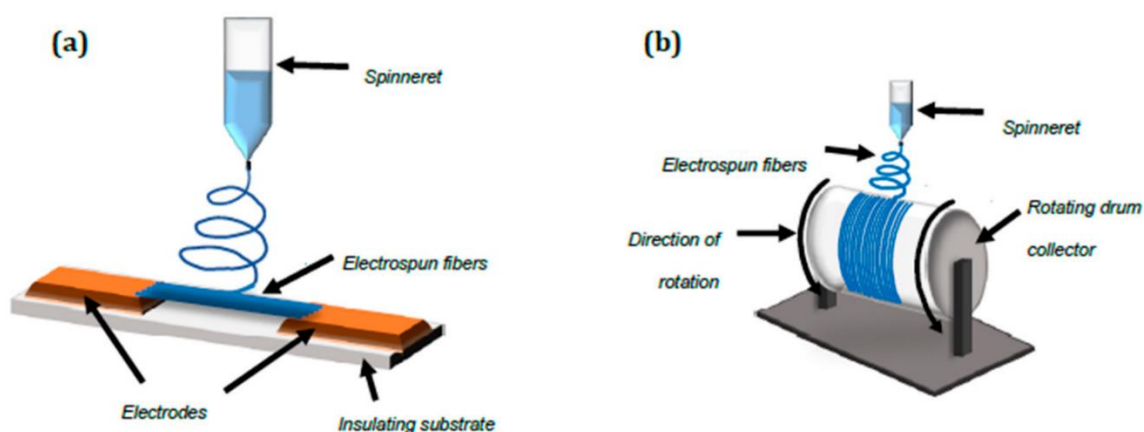


Figure 7: (a) Parallel plate electrodes and (b) rotating drum electrode used for aligned fiber deposition during electrospinning, adapted from Aminu, et al.¹⁰⁸

A rotating drum electrode aligns fibers using mechanical force. When the conductive drum is rotated at a speed such that the linear velocity of the surface is similar to the rate of electrospun fiber deposition, the fibers are stretched circumferentially around the drum, resulting in fiber alignment.¹⁰⁹ However, fast rotation rates can cause breakage of brittle polymers, so the method is not suitable for all materials, and the degree of alignment is generally much lower than that obtained by other methods. The parallel plate collector method can result in higher degrees of alignment and may be suitable for a wider range of polymers. The continuous collection plate is replaced by a collector consisting of two conductive strips separated by a gap ranging from millimeters to centimeters. The insulating gap changes the electric field structure, and deposited fibers are simultaneously attracted to the edges of the two electrodes. Deposition across the gap results in uniaxial fiber alignment, with the degree of alignment affected by gap width and fiber thickness. By introducing more pairs of electrodes around a center area, the number of axes of alignment can also be increased to produce high-quality fiber meshes.¹¹⁰

1.2.3.4. Non-polymeric fibers

Recently, the nonwoven web structure of electrospun materials has been under investigation to produce electrodes from carbon nanofibers,^{111,112} metal oxides,¹¹³ and oxide-carbon composites.¹¹⁴ While electrospinning is a polymer fabrication technique, post-processing can be applied to electrospun fiber mats to convert the structures to non-polymeric compositions. Carbon fibers have been prepared from a number of polymers by subjecting the electrospun fibers to high temperatures under vacuum, inert, or reducing atmospheres.¹¹⁵ The carbonization procedures remove additional elements present in the original polymer, leaving behind pure carbon which can then be used for applications such as catalysis and energy storage.

Metallic and ceramic fibers can be fabricated using a similar procedure with necessary additives to the electrospinning solution. Metal-containing precursors such as salts or organic compounds are added to the polymer solution prior to electrospinning. The fiber mats are heat treated in reactive atmospheres to remove the polymer from the structures as gaseous carbon compounds, and the precursors react with the atmosphere to form oxides, nitrides, silicides, or other ceramics. To produce metallic fibers, subsequent metallization is performed at high temperature in a reducing atmosphere. For both metallic and ceramic fibers, the electrospun system must be carefully engineered so that the metal-based structures solidify prior to polymer burnout in order to retain the fibrous structure without melting.

1.3. Research Goals

In the proposed work, the effects of various processing parameters on the storage capacity and stability of Mn-based electrospun web electrodes will be examined, and a model for describing performance through manipulation of the fabrication parameters will be produced. The materials system examined is a ceramic precursor of manganese acetate

($\text{Mn}(\text{COOH})_2$, $\text{Mn}(\text{Ac})_2$) in a carrier polymer of polyvinylpyrrolidone (PVP). For each parameter evaluated, specific capacitance is the primary metric by which effects will be compared. Electrochemical capacitance is measured in a standard three-electrode or two-electrode cell with cyclic voltammetry (CV). Cyclic voltammograms are collected at different scan rates, and capacitance of the electrode is calculated according to the areas within the traces. The shapes of the scans will also provide qualitative information on the electrochemical behavior of the electrode materials, including redox activity and charging/discharging kinetics. By subjecting the electrodes to many cycles, capacity fading will be measured and used to quantify electrode stability. While the ultimate response variable of interest is electrode capacitance, intermediate variables including fiber diameter and percent areal coverage of the electrode surface will also be measured. The intermediate variables are necessary for calculations and will also provide information on the effects of processing on the system. More complete understanding of electrode structures and morphology will provide insight into the processing-structure-performance relationships of the ceramic system that will be essential for developing a more complete understanding of the component interactions leading to optimization.

Fiber composition, controlled by weight percent of PVP and $\text{Mn}(\text{Ac})_2$ in the electrospinning solution, was varied, and the effects on total electrode capacitance were examined. Exploring the effects of solution composition looked at relative amounts of PVP and $\text{Mn}(\text{Ac})_2$ in the deposited fibers, as well as the sizes and morphologies of the fibers. Electrospinning time affects the ultimate active mass on the electrode by changing the number of fiber layers in the electrospun mat. Longer electrospinning times increases material loading, but with sufficiently long depositions, delamination of the ceramic layer during

calcination becomes an issue as the electrospun ceramic webs lift from the surface of the electrode in sheets. The fibers are prepared as polymer webs and retain their macro-scale dimensions after the polymer is removed and they are converted to ceramics. Upon cooling, the ceramic fibers shrink but are locked in place at junctions with other fibers, where they are fused together. As the fibers shrink, the immobile junctions cause some fibers to break, and as the fiber-fiber links are much stronger than the heterojunction between the fibers and the foil, sufficiently thick fiber mat layers will slough from the surface of the substrate in bulk. Therefore, optimal electrospinning time to prevent sloughing but maximize active mass after calcination is an important parameter for investigation. As an added consideration, electrospinning thicker webs will result in diminishing returns at some thickness as poor electrical conductivity through the oxide fibers limits charge transport to and from the fibers at the surface of the electrode. As the fibers at the very surface of the electrode have the greatest accessibility to the electrolyte, it is imperative to ensure that electrical charge is effectively conducted to the surface of the fiber mat so that electrochemical interaction can occur. The effect of calcination time at constant temperature was investigated, as longer calcination times allow for a greater degree of oxide densification at junctions between fibers and may produce stronger fiber webs. Therefore, fibers calcined for longer times have lower porosity within the fibers and a slightly smaller specific surface area, but stronger junctions between fibers may improve charge transfer from the top layers of fibers down to the substrate and enhance mechanical stability for handling and electrochemical cycling purposes. Calcination temperature was fixed, as the aluminum foil substrates employed have a limited temperature range for stability, and varying calcination temperature influences the phase of manganese oxide produced. The effects of post-electrospinning processing steps, including hot-pressing and vapor-phase partial

melting treatments to enhance adhesion of the fiber mats, were evaluated for their effects on electrode morphology and final energy storage performance.

Experimental results were used to adapt existing models from literature, with the goal of describing the effects of various system parameters on electrospun electrode behavior. Based solely on specific surface area and charge transfer limitations of manganese oxides, a minimized fiber size should result in the greatest capacitive properties. However, the effects of fiber size on electrode porosity and mass loading must also be considered as smaller fiber sizes reduce the active mass of the electrode. Because there is a complex interplay between material properties and electrode geometry to determine electrode performance, a theoretical model that assimilates measured system parameters with theoretical processes is useful for predicting the electrode materials and geometries that will result in the highest-performing electrodes. Using measured values for system parameters such as capacitance and resistance is essential as real systems rarely perform at or even near theoretical values, and the electrospinning process results in geometries that cannot be easily predicted from fabrication parameters. Additionally, the model can be used to predict more complex discharge behavior than simple capacitance, including the effect of varying current densities on discharge behavior and the resulting power densities of the device. By combining experimentally derived system values with theoretical processes and reactions, the unique freestanding web supercapacitor electrodes can be examined as a realistic system. The model was developed from and for Mn_2O_3 webs but may be expanded to other metal oxide systems fabricated with similar methods.

2. Experimental

2.1. Electrospinning

2.1.1. Single-composition

Mn_2O_3 web electrodes were fabricated via electrospinning onto foil charge-collecting substrates and subsequent calcination. The fibers analyzed in Section 3.2.1 were fabricated from manganese acetate tetrahydrate ($\text{Mn}(\text{ac})_2$, $\text{Mn}(\text{CH}_2\text{COO})_2 \cdot 4\text{H}_2\text{O}$, $\geq 99\%$, Sigma-Aldrich) and polyvinylpyrrolidone (PVP, MW=1,300,000) as purchased from Sigma-Aldrich. $\text{Mn}(\text{ac})_2$ and PVP were selected for the electrospinning system because their high solubilities in water: ethanol blends facilitated simple solution preparation, and high molecular weight PVP remains stable past the temperature where $\text{Mn}(\text{ac})_2$ is converted to oxide. Electrospinning solutions consisted of 8 % $\text{Mn}(\text{ac})_2$ / 8 % PVP by weight in a solvent of ethanol ($\geq 99.5\%$, Sigma-Aldrich), deionized water (18 M Ω), and glacial acetic acid ($\geq 99\%$, Sigma-Aldrich) with a volume ratio of 6 : 2.3 : 2.5, which was found to lengthen the shelf life of the prepared electrospinning solution. For a typical solution preparation, 0.798 g PVP was dissolved in 4.5 mL ethanol. 1.131 g $\text{Mn}(\text{ac})_2 \cdot 4\text{H}_2\text{O}$ was dissolved in solvent containing 1.5 mL ethanol, 1 mL deionized H_2O , and 2.5 mL acetic acid at 40 °C. Once both solutions were homogeneous, the $\text{Mn}(\text{ac})_2$ solution was added to the PVP solution and mixed at room temperature until homogeneous. Fibers were electrospun in a vertical electrospinner with the needle at high voltage. Separation distance was fixed at 5 cm, and voltage was maintained at 8.5-8.6 kV. Solution flowrate was adjusted to maintain stable spinning, which occurred around 0.59 mL/hr.

Fiber mats used in Section 3.3 were electrospun from a 14 % / 14 % $\text{Mn}(\text{ac})_2$ by weight in a solvent of 1:1 deionized water : ethanol. Higher PVP and $\text{Mn}(\text{ac})_2$ concentrations were introduced to increase electrospun fiber size, and acetic acid was removed from the solution to

simplify handling and reduce spinneret corrosion. All solutions prepared without acetic acid were used the same day as prepared due to rapid degradation during storage. All reagents were used as-received without further processing. A simplified solution preparation procedure was implemented wherein PVP was added to the ethanol: water solvent and mixed until fully dissolved, 3 – 4 h. The $\text{Mn}(\text{ac})_2 \cdot 4\text{H}_2\text{O}$ was then added and the solution was stirred for approximately 1 h until homogeneous. The solution was electrospun from a 22-gauge needle held at 5.7 kV with the collector plate grounded and a needle-to-collection-plate separation distance of 4.5 cm. Fiber mats were deposited for 10 min each before removal and storage in a desiccator.

2.1.2. Variable Composition

To examine the effects of fabrication parameters on electrospun web electrodes, a design matrix was prepared using a full factorial design of experiments (DOE) with three midpoints to check for curvature in the data (Table II).

Table II: Design matrix for examination of solution composition, electrospinning deposition time, and calcination time on freestanding web electrodes. Nineteen standards were required for a full 2^4 factorial design with three midpoints.

| Standard | PVP Concentration (wt%) | $\text{Mn}(\text{ac})_2$ Concentration (wt%) | Deposition Time (min) | Calcination Time (min) |
|----------|-------------------------|--|-----------------------|------------------------|
| 1 | 8 | 8 | 10 | 120 |
| 2 | 20 | 8 | 10 | 120 |
| 3 | 8 | 20 | 10 | 120 |
| 4 | 20 | 20 | 10 | 120 |
| 5 | 8 | 8 | 30 | 120 |
| 6 | 20 | 8 | 30 | 120 |
| 7 | 8 | 20 | 30 | 120 |
| 8 | 20 | 20 | 30 | 120 |
| 9 | 8 | 8 | 10 | 240 |
| 10 | 20 | 8 | 10 | 240 |
| 11 | 8 | 20 | 10 | 240 |
| 12 | 20 | 20 | 10 | 240 |
| 13 | 8 | 8 | 30 | 240 |

| | | | | |
|----|----|----|----|-----|
| 14 | 20 | 8 | 30 | 240 |
| 15 | 8 | 20 | 30 | 240 |
| 16 | 20 | 20 | 30 | 240 |
| 17 | 14 | 14 | 20 | 180 |
| 18 | 14 | 14 | 20 | 180 |
| 19 | 14 | 14 | 20 | 180 |

The low and high conditions for PVP and $\text{Mn}(\text{ac})_2$ were set at 8 wt% and 20 wt%, electrospinning deposition time was varied between 10 and 30 min, and calcination time was tested at a low value of 120 min and a high value of 240 min. Low and high values for solution composition were determined from the functional range for electrospinning. At PVP concentrations below 8 wt% or above 20 wt% solution viscosity does not allow for fiber formation during electrospinning, while low $\text{Mn}(\text{ac})_2$ concentrations prevent oxide fiber formation during calcination and higher concentrations do not dissolve fully into solution. Deposition times were also selected for functional purposes; less than 10 min deposition results in a sparse fiber mat and weak electrochemical response, and greater than 30 min results in a thick fiber mat that disrupts the electric field within the electrospinner and prevents further electrospinning. Calcination times were selected to provide sufficient time for polymer burnout. The sixteen standards evaluating low and high conditions were fabricated and tested in a random order to eliminate temporal effects, while the three midpoints (std 17, 18, and 19) were evaluated as the first, tenth, and nineteenth samples.

Electrospinning solutions were prepared from PVP and $\text{Mn}(\text{ac})_2$ in a 1:1 volume ratio of deionized water: ethanol solvent as described in Section 2.1.1. Fibers were electrospun in a Spraybase vertical electrospinner equipped with a 22-gauge needle at high voltage and a grounded collection plate. Solution flow rate was fixed at 0.20 mL/h and voltage was maintained at 6.5 kV with a separation distance of 4.5 cm between the needle and collector. Fibers were

electrospun onto 9-cm-diameter circular aluminum foil substrates. Manganese oxide films were also spin cast for comparison to the electrospun structures. To achieve areal masses similar to the electrospun electrodes, the solutions were dynamic deposited onto 9-cm aluminum foil substrates at 10,000 rpm and spun for 60 s. Deposition volumes were the same as electrospun deposition volumes based on electrospinning time and solution flow rate: 100 μL for 30 min deposition times, and 33 μL for 10 min deposition times.

2.2. Thermal Treatment

Electrospun fiber mats and spin cast films were calcined in a 2-inch-diameter tube furnace (MTI Corp, CA, USA) in air to remove the polymer from the structures and convert $\text{Mn}(\text{ac})_2$ to manganese oxide. The furnace was ramped to 600 $^{\circ}\text{C}$ at a rate of 10 $^{\circ}\text{C}/\text{min}$ and maintained at temperature for times ranging from 120 to 720 min before cooling to room temperature. The ramp rate was selected to minimize the time spent between the glass transition and vaporization temperatures of the polymer so that the fiber structure would be preserved.

For calcination in an oxidizing atmosphere, electrospun fiber mats were sealed into a 2-inch-diameter tube furnace. Oxygen gas (>99.5 %, General Distributing Co., MT, USA) was flowed through the tube at 0.3 LPM with 0 atm total relative pressure in the tube. The tube was flushed with oxygen for 20 min prior to starting the heating procedure. The furnace was ramped at 10 $^{\circ}\text{C}/\text{min}$ to 600 $^{\circ}\text{C}$ for polymer burnout, then reduced to 450 $^{\circ}\text{C}$ for the remainder of the calcination. Samples were allowed to cool overnight prior to removal from the furnace.

2.3. Variable Pressure Calcination

Samples prepared for bulk fiber treatment in Section 3.2.1 were collected by electrospinning for ~ 1 h at a time onto foil and then scraping the collected fibers into crucibles for thermal

treatment. Calcining independently from the deposition surface was necessary as the calcined structures cannot be removed from the foil. Bulk treatment also reduced total experiment time by increasing the mass of fibers that could be calcined during a single furnace run. Electrospun composite $\text{Mn}(\text{ac})_2/\text{PVP}$ fibers were ramped at $10\text{ }^\circ\text{C}/\text{min}$ to $600\text{ }^\circ\text{C}$ and held for 0.5 h, 2 h, or 4 h before cooling to room temperature. All experiments were conducted in air, at 0.81 atm (atmospheric pressure), 0.26 atm, or 0.12 atm. Pressure was controlled by adjusting the seal at the front of the tube furnace while simultaneously pulling vacuum from the rear to create flow through the tube at the specified pressure. Fibers were then processed into composite electrodes as described in Section 2.8.1.

2.4. Post-Processing

After electrospinning, the composite fibers from Section 2.1.1 were subjected to post-processing procedures to improve their mechanical stability. The samples were hot pressed, vapor melted, or both. Fiber mats were hot pressed at $120\text{ }^\circ\text{C}$ for 10 min in a manual hot press and allowed to cool in air. Vapor melting was conducted in a humidity-monitored box, where 20 mL of deionized water was deposited onto an absorbent substrate. The box was allowed to rise to 76 % relative humidity, and the fiber mats were sealed into the box for 180 s before removal to ambient air. Samples that experienced both treatments in either sequence (hot pressing then vapor melting, or vice versa) were subjected to the same conditions for each treatment as those that only underwent one post-processing step.

To measure wettability of the prepared electrodes, a $10\text{ }\mu\text{L}$ droplet of deionized water was dispensed onto the surface of each electrode. Side-on images were taken for three samples from each condition, and the contact angle of the water droplet was measured in ImageJ.¹¹⁶ The average of the three measurements was reported as the contact angle for given treatment.

2.5. Imaging

2.5.1.1. Transmission Electron Microscopy (TEM)

Electrospun fibers for TEM examination were prepared directly on 3.0 mm PELCO Stainless Steel TEM grids (Ted Pella Inc., CA, USA). The grids were placed onto the aluminum foil collector during electrospinning and calcined according to the procedures described in Section 2.2. The fiber mats were imaged at 200 kV with a Philips CM-200 FEG-TEM equipped with a cryogenic cooling arm.

2.5.1.2. Scanning Electron Microscopy (SEM)

Scanning electron micrographs were collected with a Tescan Mira3 FE-SEM operated at 15.00 kV and a Hitachi S4500 SEM at 20.00 kV. Samples were cut from the as-spun and calcined fiber mats, mounted onto aluminum stubs, and lightly gold coated prior to imaging. SEM was used to measure fiber mat thickness, porosity, and average fiber diameter. From each fiber mat, planar and cross-sectional images were collected at multiple locations. Image analysis to determine fiber thickness, mat thickness, and porosity was performed in ImageJ. For fiber thickness, the average of 30 diameter measurements from five locations was taken as average diameter. Fiber mat thickness was taken as the average of 20 measurements from cross-sectional images. Fiber thickness was quite variable, with typical ranges of approximately 100 nm; fiber mat cross-sectional thickness had similar ranges of around 100 – 150 nm.

Porosity was measured from SEM micrographs by thresholding the image so that all fibers were displayed as white pixels, and voids were black (Figure 8).

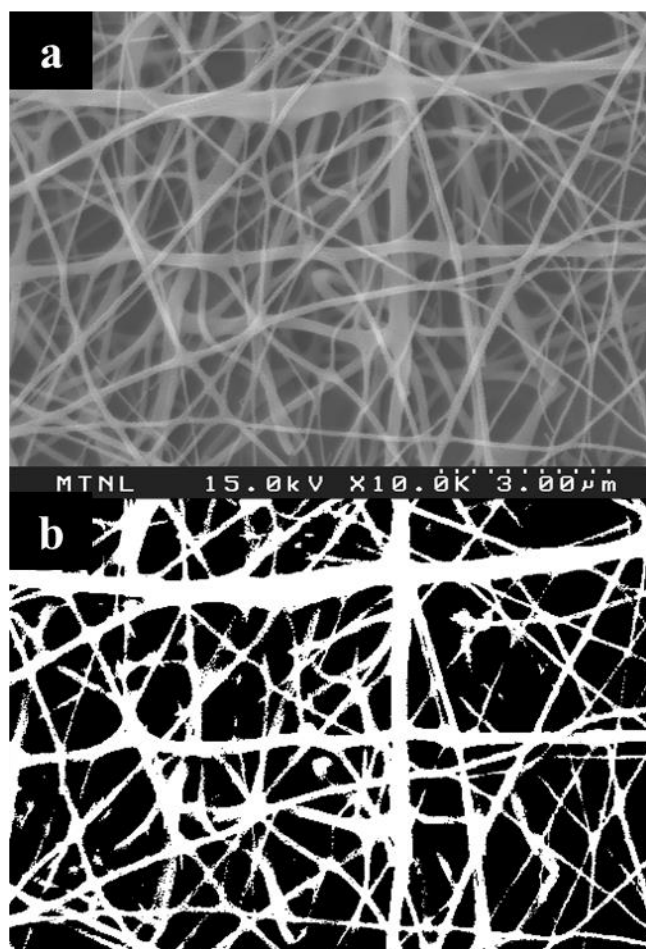


Figure 8: Scanning electron micrograph (SEM) of electrospun fiber mat electrode before (a) and after (b) thresholding used to measure porosity by calculating ratio of black pixels to total pixels on the thresholded image.

The ratio of black pixels to total pixels in the image was taken to represent fiber mat porosity.

Porosity was measured from 10 locations and averaged to yield the fiber mat porosity used in the model.

2.6. X-ray Diffraction (XRD)

The aluminum foil substrates used to support the electrospun structures exhibit strong diffraction peaks overlapping those of Mn_2O_3 , preventing direct XRD interrogation of the electrospun oxide structures. Once fabricated, the electrospun fiber mats cannot be removed from

the charge collecting substrate. Thus, a powder approximation was necessary to isolate the oxide X-ray signal from that of the aluminum substrate. To prepare samples for powder XRD, PVP and $\text{Mn}(\text{ac})_2 \cdot 4\text{H}_2\text{O}$ were mixed in a crucible in 1:1, 1:2.5, or 2.5:1 weight ratios to replicate the weight ratios present in the electrospun structures. The powders were calcined under the same conditions as the corresponding electrospun fibers and crushed to remove agglomerations. Diffractograms were collected with a Rigaku Ultima IV X-ray diffractometer from 20-80 deg. at a scan rate of 2 deg./min. A Cu-K α source was used with a Ni filter at 40 kV and 40 mA.

2.7. Thermogravimetric Analysis

As-received PVP and $\text{Mn}(\text{ac})_2 \cdot 4\text{H}_2\text{O}$ and as-electrospun fibers were analyzed with a TA Instruments SDT-650 STA to determine critical temperatures for the electrospun composite system. Samples were heated in an alumina crucible from room temperature to 600 °C at a rate of 10 °C/min under flowing air to detect material changes.

2.8. Electrochemistry

2.8.1. Composite Electrodes

Fibers were processed into stable electrodes prior to electrochemical characterization for Section 3.2.1. Calcined samples were mixed with acetylene black and polyvinylidene difluoride (PVDF) binder (MTI Corp., CA, USA) in a 70:15:15 weight ratio to improve sample conductivity and mechanical stability, and N-methyl pyrrolidinone (≥ 99 , Sigma-Aldrich) was added to form a thick slurry. The slurry was doctor bladed onto Ni mesh substrates (MTI Corp., CA, USA) and the electrodes were dried at 100 °C for 24 h before examination.

Electrochemical characterization was performed in 0.5 M Na₂SO₄ ($\geq 99.0\%$, Sigma-Aldrich) with a Pt wire counter electrode and Ag/AgCl reference electrode. A Keithley 2450 SourceMeter was used as the electrochemical test station. The working electrode was tested using an electrode holder with defined area of 0.421 cm² and a standard three-electrode configuration. Cyclic voltammetry (CV) was performed between -0.4 and 1.3 V vs Ag/AgCl at rates between 25 and 200 mV·s⁻¹. The voltage range was selected to capture the redox activity observed above 1 V.

2.8.2. Freestanding Electrodes

2.8.2.1. Three Electrode Cell

Calcined samples for Sections 3.1, 3.2.1, and 3.3 were tested in a standard configuration three-electrode electrochemical cell with Ag/AgCl reference electrode and Pt wire counter electrode, and 1.0 M Na₂SO₄ electrolyte. A Keithley 2450 SourceMeter was used as the potentiostat. Circular samples were cut from the calcined fiber mats and placed into a circular foil holder with a defined area of 0.421 cm². Cyclic voltammograms were recorded between -0.3 and $+0.3$ V at scan rates of 25, 50, 100, and 200 mV/s. Three samples were tested for each standard, and the average of the calculated capacitances were taken as the areal capacitance of the standard. Typical ranges for the three samples were between 10 % - 40 % of the calculated average.

2.8.2.2. Two-Electrode Symmetrical Cell

Electrodes for Sections 3.2.2, 3.4, and 3.5.1 were tested as symmetrical cells in a two-electrode split cell (MTI Corp., USA) with 15 mm electrodes cut from the calcined fiber mats, a glass microfiber filter separator (Whatman, Grade GF/F), and 1.0 M Na₂SO₄ electrolyte. A two-electrode configuration was used to characterize the cells with cyclic voltammetry (CV),

linear sweep voltammetry (LSV), electrochemical impedance spectroscopy (EIS), and galvanostatic charge-discharge (GCD), with a Gamry 1010E electrochemical test station used to conduct all tests. Each test was performed on three cells and the calculated values were taken as the average of the measurements.

For LSV, linear sweeps were taken from -0.1 V to 0.1 V at 0.5 mV/s, and the results were plotted as $\log(\text{current})$ vs potential to produce a Tafel plot from which transfer coefficients and exchange current density were extracted. Cyclic voltammograms were collected from 0 to 1 V at scan rates of 10, 5, 50, 100, and 200 mV/s and were used to calculate areal capacitance of the cells. EIS was conducted on the cells from 1 MHz to 0.1 Hz, with 0 V DC and 5 mV AC applied. Bode and Nyquist plots generated from EIS were fit with equivalent circuit models to describe the observed behavior and isolate double layer capacitance from pseudocapacitive energy storage modes. The same equivalent circuit model was used to describe all samples. GCD was used to examine cycling stability of the freestanding electrospun electrodes. Current densities of 1, 5, and 10 A/g were applied to the cells to charge to 1 V before discharging to 0 V. The 0 – 1 V charge and discharge cycle at constant current density was continued for 100 cycles and the capacitance was calculated from each GCD cycle by the Gamry Echem Analyst software.

2.9. Model Implementation

The theoretical model was implemented in R,¹¹⁷ with the package deSolve¹¹⁸ used to solve the system of ordinary differential equations. For each iteration, the spatial domain was divided into 50 boxes, and the time domain was given a step size of 0.1 s. For generating Ragone plots at current densities above 100 A/g, the time domain was given a step size of 0.01 s to improve prediction accuracy between 1 and 0 V. For Section 3.5.5, the time domain was adjusted with the total discharge time to give at least 100 steps.

3. Results and Discussion

3.1. Effects of Fabrication Parameters on Electrospun Electrodes

Prior to further characterization, the thermal behavior of the PVP/Mn(ac)₂ system was examined to ensure that the acetate-to-oxide conversion occurred at a lower temperature than polymer burnout to prevent fiber melting. Components of the electrospun fibers were examined with thermogravimetry both in as-received form and in the as-electrospun fiber (Figure 9).

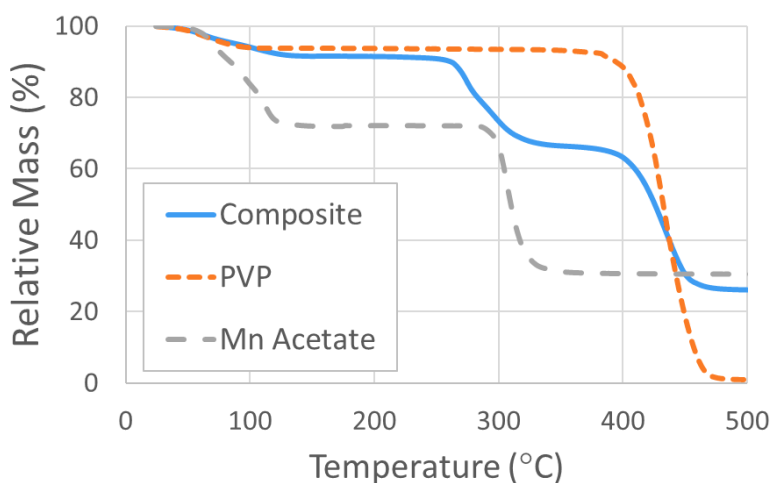


Figure 9: Thermogravimetric analysis plot of as-received Mn(ac)₂, as-received PVP, and as-electrospun composite fibers.

By examining sample mass loss as temperature increases, the critical temperatures at which chemical reactions and vaporization occur can be determined. Additionally, by testing both fiber components individually as well as in the composite form, changes to the thermal behavior due to reactions between the PVP and acetate can be identified. In both the composite fiber and as a pure sample, Mn(ac)₂·4H₂O loses mass due to dehydration between 60-110 °C, and then again at 290 °C as it is converted to the lower molecular weight M₂O₃. The PVP carrier polymer exhibits a slight mass loss due to dehydration around 100 °C and then complete removal from 440-460 °C. In the electrospun fibers, onset of Mn(ac)₂ oxidation begins slightly earlier than in the

pure material, around 260 °C, due to improved heat transfer properties of the high surface-area-to-volume ratio of the electrospun fibers as compared to as-received acetate crystals. Polymer burnout occurs in the same temperature range for the electrospun fibers as for the pure material, as the ultra-high molecular weight of the polymer results in a high degree of chain entanglement, limiting significant depression of the oxidation temperature in the nanostructures. Based on thermogravimetry, chemical interactions between the acetate precursor and polymer matrix are not significant to the thermal behavior of either component, as decomposition temperatures in the composite correspond directly to those of the individual components. $\text{Mn}(\text{ac})_2$ conversion to Mn_2O_3 occurs prior to polymer removal, allowing for the electrospun fiber morphology to be maintained throughout thermal treatment.

To determine the effects of fabrication parameters on the structure and performance of freestanding electrospun electrodes, a 2^4 factorial design was used with StatEase statistical modeling software. Because solution composition was varied between conditions, it was necessary to first confirm that no phase changes occurred in the ceramic as a result of the changing ratios of polymer and precursor. After electrospinning and calcination in air to convert the polymer fibers to ceramic structures, powder XRD was used to confirm phase of the electrospun oxide structures (Figure 10).

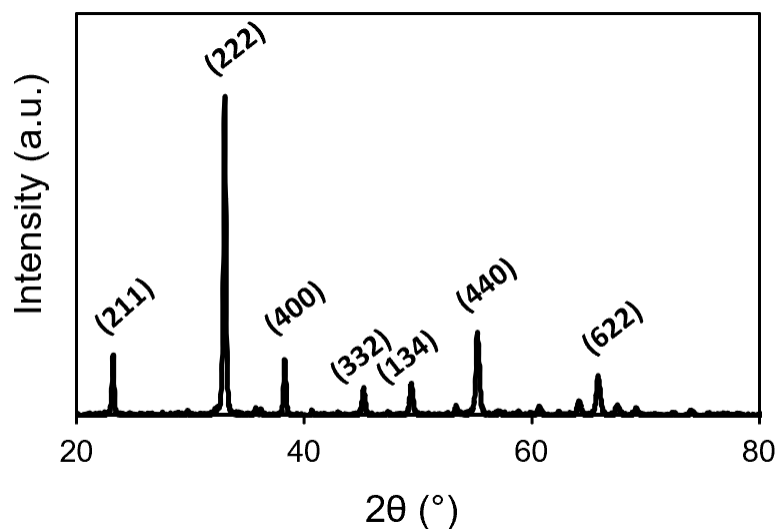


Figure 10: X-ray diffractogram of powder-processed 1:1 PVP: $\text{Mn}(\text{ac})_2$ to determine phase of oxide produced during calcination of electrospun composite fibers. Planes associated with each major diffraction peak are labeled. The diffractograms for the 1:2.5 and 2.5:1 compositions are not presented due to lack of variation between conditions. The observed X-ray diffractogram is characteristic of Mn_2O_3 .

Individual powder samples reflecting the weight ratios of polymer and acetate resulting from each of the electrospinning solutions were produced and analyzed. Powders with 1:1 weight ratios of PVP and $\text{Mn}(\text{ac})_2$ represented the 8 % / 8 % and 20 % / 20 % electrospinning solutions, while 1:2.5 PVP: $\text{Mn}(\text{ac})_2$ (or vice versa) weight ratios represented 8 % / 20 % solutions. For all weight ratios, all XRD peaks were indexed to Mn_2O_3 . Lack of variation between conditions indicates that the relative amounts of PVP and $\text{Mn}(\text{ac})_2$ in the fibers do not affect the oxidation state of manganese in the final structure; and therefore, variations in the areal capacitance of the web electrodes are likely not due to chemical differences.

Cyclic voltammetry was used to measure the areal capacitance of the freestanding Mn_2O_3 web electrodes. Voltammograms were collected for each fabrication condition at scan rates between 25 and 200 mV/s (Figure 11).

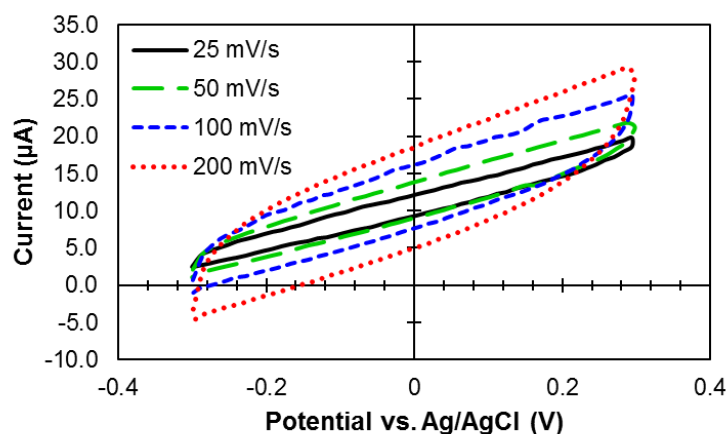


Figure 11: A typical cyclic voltammogram under the examined conditions. Scan displayed is of electrode prepared from 8 % PVP/ 8 % Mn(ac)₂, deposited for 30 min and calcined for 120 min. The inclined shape and lack of redox peaks are typical for all samples.

The web electrodes exhibit electrochemical traces about an inclined axis. The incline of the voltammograms results from the conductive behavior of the aluminum foil charge-collecting substrate: aqueous electrolyte wets the electrodes and substrate thoroughly, so direct contact between the electrolyte and charge collector results in the addition of a conductive I-V curve to the capacitive component of measured current. Relatively low mass loading onto the substrates decreases the scale of the capacitive voltammogram and gives the current collector a significant impact on the shape of the scan, which is characteristic of resistive capacitors. No redox peaks are evident in the forward or reverse scans, and voltammetric curves broadened with increasing scan rate.

Areal capacitance of the electrospun web electrodes was calculated according to the equation

$$C_a = \frac{\int (iv) dv}{\mu A \Delta V} \quad (1)$$

Where C_a is areal capacitance (F/cm^2); i and v are current (A) and voltage (V), respectively, as recorded by the potentiostat; μ is the scan rate (V/s); A is the exposed area (cm^2) of the electrode, defined by the electrode holder; and ΔV is the voltage window (V) of the scan. Tabulation of the calculated areal capacitance for each sample at all scan rates is presented in Appendix A.

Design Expert 12 was used to fit a statistical model to the data and determine the significance and relative impact of PVP and $\text{Mn}(\text{ac})_2$ concentrations, deposition time, and calcination time on areal capacitance. To visually demonstrate the effect of each parameter on capacitance, data sets were collapsed to the parameter of interest by taking the average of all measurements encompassing the data point (*e.g.*, for the effect of calcination time, the data point for each scan rate in the 120 min data set represents the average of all standards calcined for 120 min; standards 1-8). The midpoint conditions were not tested in combination with the high and low limits from the DOE, so the results for those three standards could not be treated with the same methodology and are therefore not included in the graphical representation. However, the statistical models indicate that curvature is not significant within the range studied, so their exclusion does not affect the trends described by the model.

3.1.1. Solution Composition

Fibers were electrospun directly onto aluminum foil charge-collecting substrates from four solution compositions of 8 % / 8 %, 8 % / 20 %, 20 % / 8 %, and 20 % / 20 % PVP/ $\text{Mn}(\text{ac})_2$ for 10 and 30 min. As-spun fibers morphologies were examined prior to calcination (Figure 12).

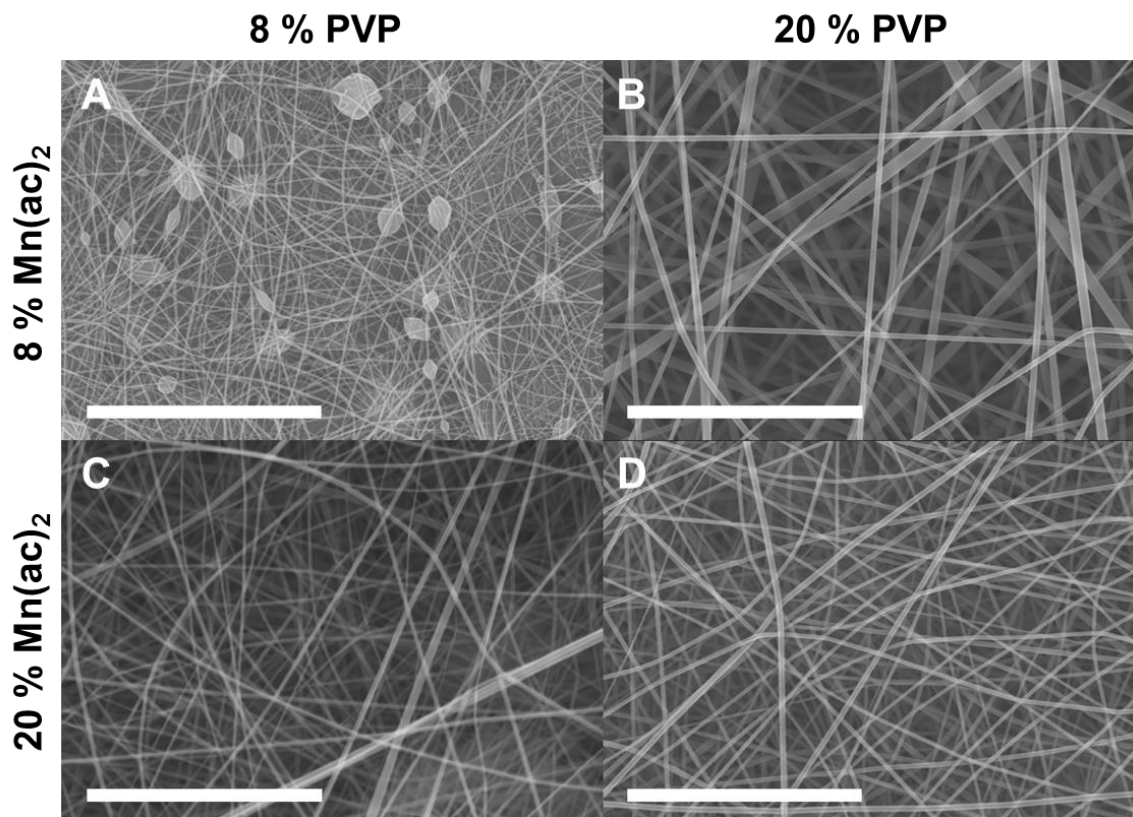


Figure 12: Scanning electron micrographs of as-electrospun PVP/ $\text{Mn}(\text{ac})_2$ composite fibers deposited for 30 min from solution composed of (A) 8 % PVP / 8 % $\text{Mn}(\text{ac})_2$, 69 nm average diameter; (B) 20 % PVP / 8 % $\text{Mn}(\text{ac})_2$, 340 nm average diameter; (C) 8 % PVP / 20 % $\text{Mn}(\text{ac})_2$, 162 nm average diameter; and (D) 20 % PVP / 20 % $\text{Mn}(\text{ac})_2$, 154 nm average diameter. All scale bars are 10 μm . As-spun fiber morphologies were not affected by deposition time, so the 10 min condition is not presented.

All electrospinning conditions result in discrete fibers, without evidence of electrospaying or excessive fiber melting upon or after deposition. Fibers prepared from 8 % PVP / 8 % $\text{Mn}(\text{ac})_2$ exhibit beading, which is not observed with other solution compositions. While the 8 % / 8 % fibers have a smaller average diameter than those from other solution compositions, a significant difference in fiber diameter was not observed between fibers prepared with 8% PVP / 20 % $\text{Mn}(\text{ac})_2$ and 20 % PVP / 20 % $\text{Mn}(\text{ac})_2$, suggesting that the concentration of oxide precursor in the fibers has a strong effect on the electrospinning process.

With a 20 % PVP / 8 % $\text{Mn}(\text{ac})_2$ electrospinning solution, the resultant fibers have diameters approximately twice that of those prepared from the other solutions. Solution conductivity is primarily related to $\text{Mn}(\text{ac})_2$ content, so increasing concentration of the precursor elevates the conductivity of the electrospinning solution. With 20 % PVP, the solution is highly viscous, and with low $\text{Mn}(\text{ac})_2$ concentration, the applied electric field has a weaker stretching effect on the fibers, resulting in higher average diameter.

Each solution from the experimental design was electrospun for both 10 and 30 min deposition times, and samples from each of those conditions were calcined for 120 and 240 min prior to testing. Of the parameters examined, electrospinning solution composition had the largest visible effect on final electrode morphologies (Figure 13).

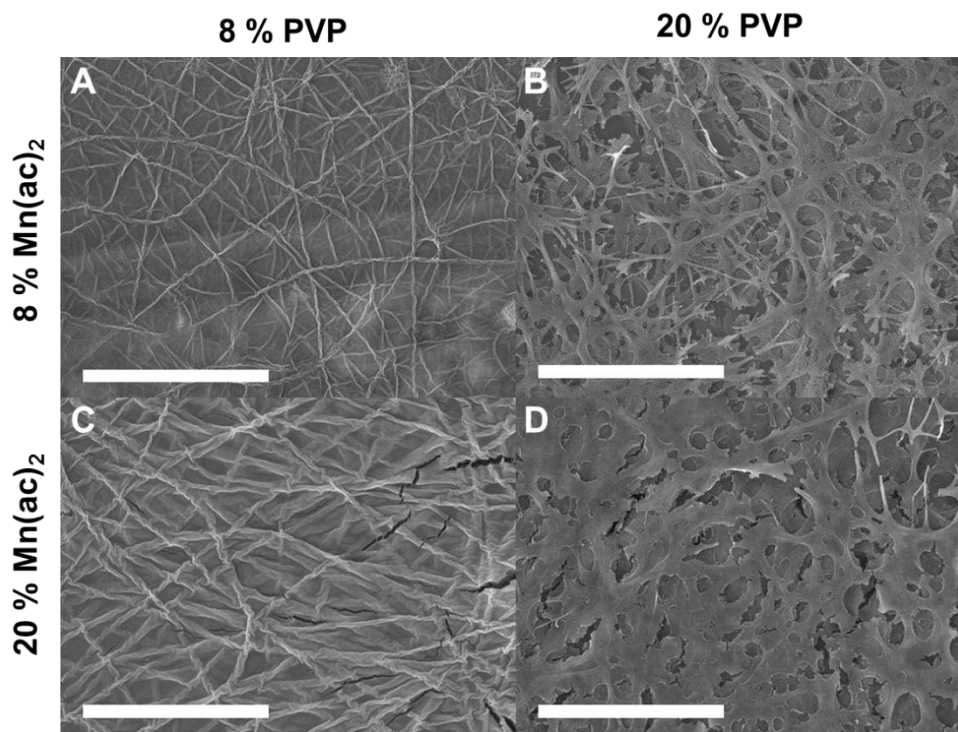


Figure 13: Scanning electron micrographs of samples prepared with (A) 8 % PVP / 8 % $\text{Mn}(\text{ac})_2$; (B) 20 % PVP / 8 % $\text{Mn}(\text{ac})_2$; (C) 8 % PVP / 20 % $\text{Mn}(\text{ac})_2$; and (D) 20 % PVP / 20 % $\text{Mn}(\text{ac})_2$, deposited for 30 min

and calcined for 240 min. All scale bars are 10 μm . Trends exhibited by solution composition modification were consistent for the 10 min deposition and 120 min calcination conditions and are therefore not shown.

Polymer concentration in the electrospinning solution had the most consistent and visible effect on fiber morphology, with low-PVP solutions exhibiting a nanowrinkle morphology and high-PVP solutions maintaining a fused-fiber structure. The nanowrinkle structures observed in 8 % PVP fibers likely result from the small initial fiber diameter previously discussed. Previous work has shown that during heating, $\text{Mn}(\text{ac})_2$ is converted to Mn_2O_3 before PVP removal,¹¹⁹ so the oxide structure is already formed upon polymer burnout. Small-diameter electrospun fibers from the 8 % PVP solution contain relatively smaller amounts of $\text{Mn}(\text{ac})_2$, inhibiting stable oxide network formation as the polymer softens, melts, and eventually burns off. The mechanical weakness of the fine oxide network formed causes the fibers to collapse and melt together into a film-like structure with fibrous wrinkles at the surface. Conversely, the thicker fibers deposited from 20 % PVP solutions form more mechanically-stable oxide networks that are capable of supporting themselves once the polymer structures are removed.

The concentration of $\text{Mn}(\text{ac})_2$ in the electrospinning solution did not have a visible effect on the nanowrinkle structures but affected the porosity of the fiber-based structures (Figure 14).

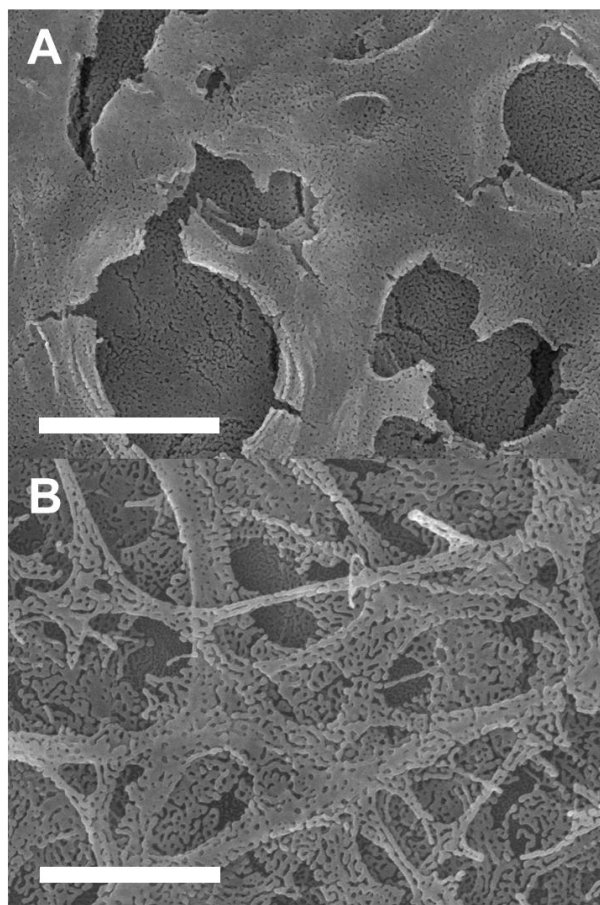


Figure 14: Detail of electrodes (A) prepared with 20% PVP and 20 % Mn(ac)₂, showing the slight porosity evident in nearly all the examined conditions; (B) prepared with 20 % PVP and 8 % Mn(ac)₂, with high porosity unique to the fibrous structures fabricated from low-Mn(ac)₂ electrospinning solutions. Scale bars are 2 μm .

All samples exhibited some porosity, but the number of large pores was greatly increased for fiber-based structures prepared with 8 % Mn(ac)₂. High porosity results from greater dispersion of Mn(ac)₂ within the electrospun composite fibers. With high Mn(ac)₂ concentration, the oxide particles that form during the initial stages of calcination are in sufficiently close proximity that densification at higher temperatures nearly eliminates major porosity in the structure. However, with low Mn(ac)₂ concentration, oxide-rich regions in the fibers are initially spaced distantly enough that densification cannot effectively eliminate pores over the same

heating duration. While low $\text{Mn}(\text{ac})_2$ content results in higher porosity, accompanied by higher specific surface area, the total mass of oxide deposited is lower, so improvements in capacitance from the higher specific surface area will be mitigated by a decrease in active mass.

Increasing PVP concentration in the electrospinning solution slightly increases areal capacitance (Figure 15). Areal capacitance is calculated from nominal electrode area, as defined by electrode diameter.

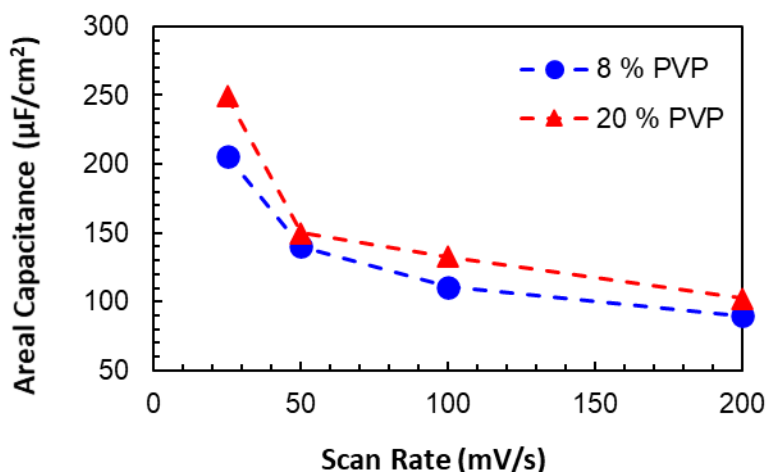


Figure 15: Graphical representation of the effect of PVP concentration on areal capacitance of electrospun Mn_2O_3 electrodes across multiple scan rates. Each data point is the average of eight conditions, with three measurements for each standard.

A slight increase in areal capacitance is evident with increased PVP concentration in the electrospinning solution. Polymer concentration controls the morphology of calcined structures, with fibers resulting from a high polymer concentration and nanowrinkles from low concentration. The relatively greater specific surface area of fiber-based morphologies, compared to nanowrinkle structures, increases storage capacity directly due to a greater number of storage sites available. However, the nanowrinkle morphologies still have rough surfaces with high

surface areas, so the capacitance increase is minor compared to the magnitude of measured capacitance.

Increasing concentration of $\text{Mn}(\text{ac})_2$ in the electrospinning solution decreases areal capacitance of the web electrodes, as shown in Figure 16.

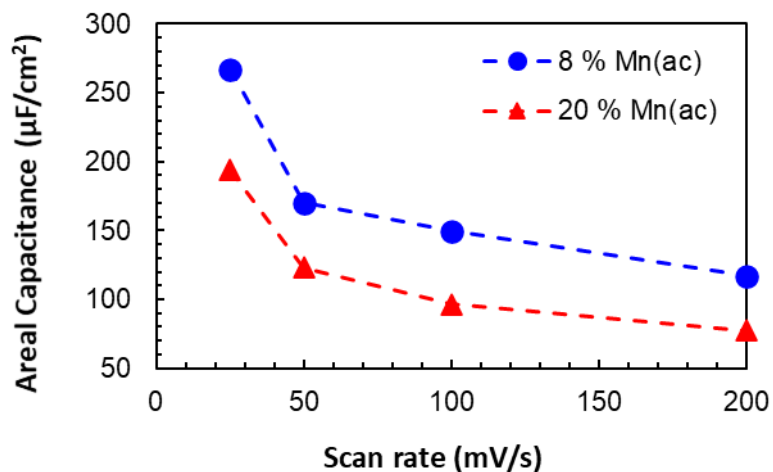


Figure 16: Graphical representation of the effect of $\text{Mn}(\text{ac})_2$ concentration on areal capacitance of electrospun Mn_2O_3 electrodes across multiple scan rates. Each data point is the average of eight conditions, with three measurements for each standard.

With increased acetate content in the electrospinning solution, a relatively large decrease in areal capacitance is observed. Despite the reduced active mass in electrodes prepared from solutions with low $\text{Mn}(\text{ac})_2$ concentration, the high porosity observed in the structures has a greater effect on available surface area than total oxide mass. The lower porosity and specific surface area resulting from increased precursor concentration causes decreased overall performance due to fewer active sites for electrolyte interaction. At all scan rates, $\text{Mn}(\text{ac})_2$ concentration has a significant effect on performance, with an average 30 % and maximum 76 % capacitance increase between the high and low $\text{Mn}(\text{ac})_2$ concentration. The difference in performance across all scan speeds suggests that the pores in the fabricated electrodes are highly

accessible to electrolyte ions and greatly increase accessible surface area, regardless of whether the calcined structures retain their discrete fiber morphologies. For structures fabricated with 8 % PVP, the electrodes lose their freestanding morphology and become film-based rather than fiber-based. The film-based structures do not exhibit the high porosities observed with 20 % PVP electrodes, but the improved performance remains. With low $\text{Mn}(\text{ac})_2$ concentration, a thinner oxide layer results due to the smaller mass of precursor deposited over the same area. The thinner layer results in higher capacitance than the thicker oxide from 20 % $\text{Mn}(\text{ac})_2$ due to increased out-of-plane structure conductivity from shortened charge transfer pathways. By decreasing the distance that electrons must travel to reach the electrode surface, the number of scattering events is decreased and the high resistivity of Mn_2O_3 is combated. By causing greater porosity in the structures, performance of electrospun electrodes can be increased by using low precursor concentration in the electrospinning solution.

3.1.2. Electrospinning Deposition Time

Deposition time does not have a visible effect on the morphologies of the calcined electrodes. However, increasing deposition time improves electrochemical performance, as the amount of oxide present for energy storage increases with longer deposition times (Figure 17).

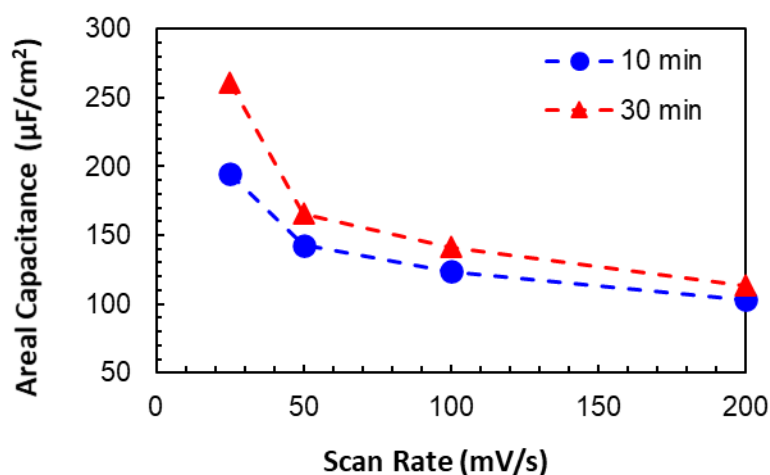


Figure 17: Graphical representation of the effect of electrospinning deposition time on areal capacitance of electrospun Mn_2O_3 electrodes across multiple scan rates. Each data point is the average of eight conditions, with three measurements for each standard.

At slow scan rates, a longer deposition time significantly increases capacitance, but the effect fades with increasing scan rate. With a greater active mass, especially for fibrous structures, more sites are available for energy storage. Although the total mass of Mn_2O_3 deposited is approximately three times greater in samples deposited for 30 min than those deposited for only 10 min, the observed increase in capacitance is only 34 % at 25 mV/s and decreases at faster scan rates. With longer deposition times, fiber intermelting and loss of discrete fiber structure prevents the theoretical threefold increase in available surface area that could be expected with a threefold increase in fiber mass. Fiber layers beneath the surface of the electrode may not be as easily accessible, so the increase in mass would not correlate directly to increased surface area. Additionally, increasing the thickness of the electrode negatively affects electronic conductivity through the structure, so the oxide layers furthest from the charge collector cannot store charge as effectively as those closest to the substrate. As a result, areal capacitance does not increase proportionally to increasing active mass via longer deposition

time. However, increased deposition times do improve performance by increasing the active mass of the electrodes.

3.1.3. Calcination Time

Calcination time has only a small effect on the visible external structure of calcined fiber mats. For the 20 % PVP / 20 % Mn(ac)₂ electrospinning solution, fiber definition within the structure decreases slightly with increasing calcination times (Figure 18), but the trend is not visible in the 20 % PVP / 8 % Mn(ac)₂ condition, which also exhibits a fused-fiber structure.

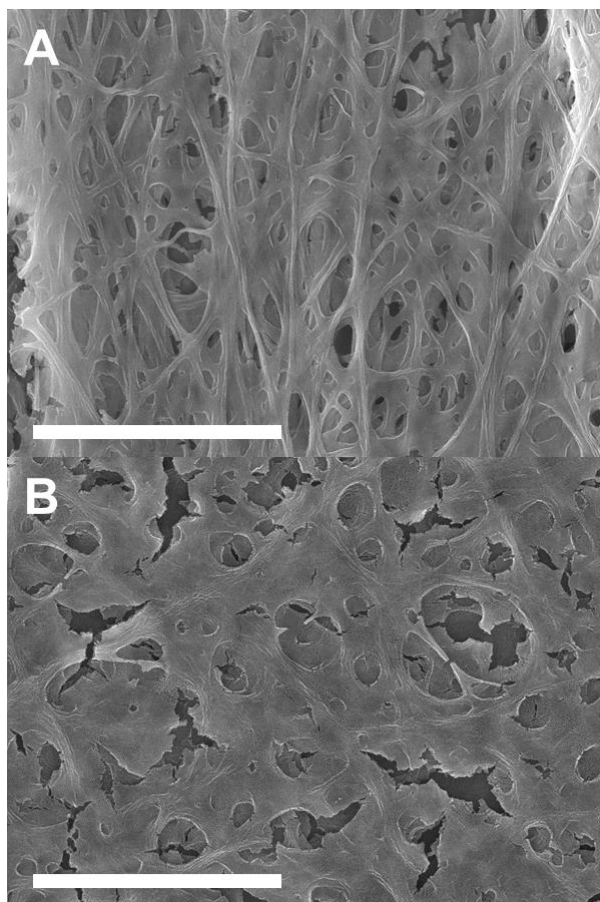


Figure 18: Morphologies of samples prepared with 20 % PVP / 20 % Mn(ac)₂ electrospinning solutions, deposited for 10 min and calcined for (A) 120 min, and (B) 240 min. Samples electrospun from the same

solution composition and deposited for 30 min display morphologies nearly identical to that observed in (B) and are therefore not presented. Scale bars are 10 μm .

Somewhat less distinct fiber definition is evident in samples that were calcined for 240 min than those treated for shorter time periods. During calcination, the fiber structures always exhibit some degree of intermelting, resulting from sintering at the fiber junctions and subsequent self-diffusion of the oxide toward the lowest surface energy structure of a smooth surface. With increased calcination time, more diffusion and bulk structure densification causes further intermelting and loss of discrete fiber structures. With the 8 % $\text{Mn}(\text{ac})_2$ electrospinning solution, the trend is not observable as the initial fiber structure is already less defined than that exhibited with the 20 % $\text{Mn}(\text{ac})_2$ solution. Loss of definition may in fact be present but is too subtle to detect by visual inspection.

Lengthening calcination duration also elevates areal capacitance of the electrospun web electrodes (Figure 19).

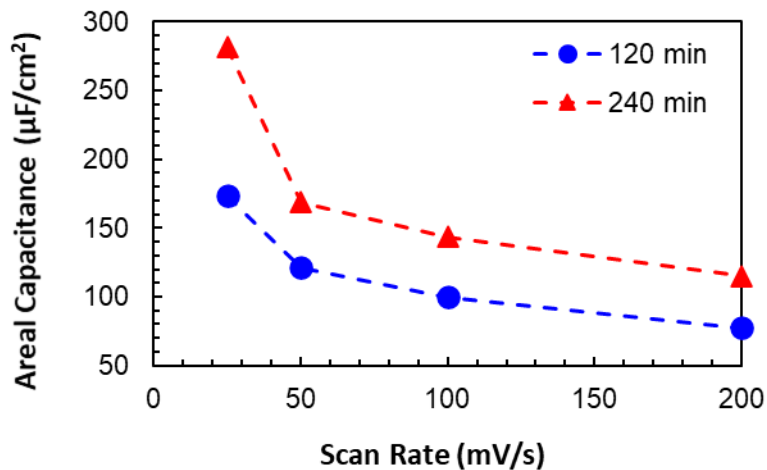


Figure 19: Graphical representation of the effect of fiber calcination time on areal capacitance of electrospun Mn_2O_3 electrodes across multiple scan rates. Each data point is the average of eight conditions, with three measurements for each standard.

At all scan rates, area capacitance is significantly increased by lengthened calcination times. With extended time at high temperature, densification of the ceramic structures may proceed more completely, and interior porosity is minimized. The densified ceramic webs provide more direct conductive pathways than structures with significant interior porosity acting as insulating regions. Shorter charge transfer pathways allow for more effective electronic conduction between the charge collector and electrolyte/electrode heterojunction at the surface of the oxide webs. Without the ability to effectively charge the oxide surfaces, the electrodes cannot attract and repel electrolyte ions, so optimized electrical conductivity through the structure is essential to electrochemical performance. In addition to decreasing interior porosity, longer calcination times encourage grain growth in the ceramic, thereby increasing conductivity in the structures via reduction in grain boundary scattering.^{120,121} At 25 mV/s, calcination time has the strongest effect on capacitance of the parameters tested, with an average 62 % and maximum 140 % capacitance increase observed between the 120 min and 240 min conditions. At faster scan rates, the effects of deposition time and calcination duration have similar magnitudes, which are stronger than the effect of PVP concentration but weaker than the effect of $\text{Mn}(\text{ac})_2$ concentration.

Because increasing calcination time from 120 to 240 min improved performance, the effects of calcination time past 240 min was also investigated (Figure 20).

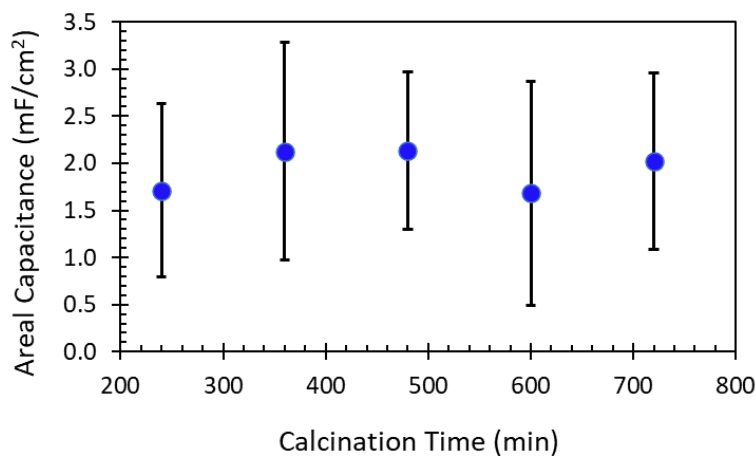


Figure 20: Effect of calcination time on areal capacitance of electrospun freestanding Mn_2O_3 electrodes fabricated from 20 % PVP/ 8 % $\text{Mn}(\text{ac})_2$ solutions. Areal capacitances were measured from cyclic voltammograms collected at 10 mV/s; error bars indicate 95 % confidence intervals.

Past 240 minutes, increasing calcination time does not have a statistically significant effect on electrode performance, with the average capacitances for all conditions clustered around 1.5 – 2.5 mF/cm^2 nominal electrode area at 10 mV/s and no visible trends relating the calcination time and specific capacitances. The lack of trends in specific capacitance for calcination times longer than 240 minutes was observed at all scan rates from 10 to 200 mV/s.

Increasing calcination time from 120 to 240 min had a visible effect on fiber porosity (Figure 21), but past 240 min there were no visible changes in fiber structure.

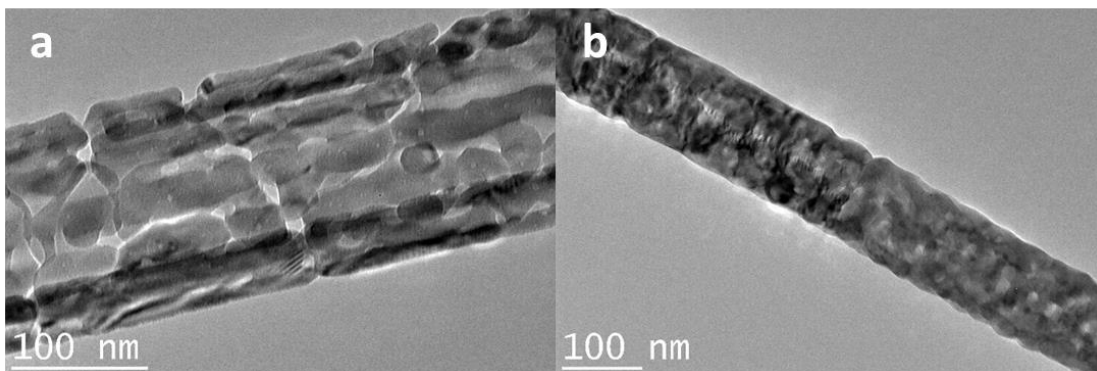


Figure 21: TEM micrographs of electrospun fibers calcined at 600 °C for (a) 120 min and (b) 240 min.

Calcination times longer than 240 min did not present visible distinction from (b).

Between 120 and 240 min, the interior porosity of the fibers (visible in Figure 21 as light regions) decreased significantly. The fibers calcined for 120 min (Figure 21a) have a nearly hollow structure, indicated by dark exterior walls and a lighter fiber interior. After 240 min (Figure 21b), the fibers no longer exhibit shade differentiation between the walls and interior, and instead show a consistent mottled appearance through the thickness, which indicates uniform porosity throughout the fiber. While decreasing porosity, as observed between 120 and 240 min calcination, has a negative effect on surface area, the decrease in surface area is countered by improved matrix conductivity, as the more continuous fiber structure in Figure 21b presents shorter charge transfer pathways for charging and discharging. Calcination times between 240 and 720 min exhibited similar structures to the 240-min calcination, which is consistent with the electrochemical results showing no significant difference in energy storage performance past 240 min calcination times.

3.1.4. Multivariable Interactions

Two-factor interactions were also considered based on their statistical significance as determined by the Design Expert model. Interactions between electrospinning duration and other

parameters were found to be significant in that short deposition times depress the effects of the other variables examined. For the samples prepared with 10 min electrospinning stages, little to no difference was observed in capacitance resulting from changes to calcination time or $\text{Mn}(\text{ac})_2$ concentration.

For short electrospinning times, a thin fiber mat is deposited, with a shorter distance for charge transfer to occur between the charge collector and top surface of the electrode. Because the charge transfer pathways are inherently shorter for the thin fiber mats, the effects of calcination time on structure conductivity become less significant and more difficult to detect. Similarly, the smaller mass of oxide in electrodes produced with short electrospinning times leads to a less noticeable increase in measurable surface area with high-porosity electrodes produced from 8 % $\text{Mn}(\text{ac})_2$. Because the surface area increase from the porous structure is necessarily proportionate to the initial mass of fibers deposited, a larger improvement in capacitance is observed from a larger starting mass of fibers. Longer deposition times result in a greater mass of fibers and therefore more detectable changes relating to the other experimental variables.

Additionally, the interaction between deposition time and $\text{Mn}(\text{ac})_2$ concentration in the electrospinning solution suggests that the major limiting factor in performance increase of the high-porosity structures fabricated from 8 % $\text{Mn}(\text{ac})_2$ solutions is primarily limited conductivity through the structure, rather than poor accessibility of the electrode surfaces with increasing thickness. If fiber layers were inaccessible to the electrolyte due to increased electrode thickness from longer deposition time, the effect of $\text{Mn}(\text{ac})_2$ concentration on areal capacitance would become less significant with longer deposition, as the proportionate surface area increase from high porosity would only be observable for the small fraction of active material on the top layers

of the electrodes. Because the opposite is observed ($\text{Mn}(\text{ac})_2$ concentration has a larger effect with longer deposition), it is inferred that the thicker electrodes from long electrospinning stages retain excellent electrotype permeability but possess poor electrical conductivities.

3.1.5. Comparison to Planar Structures

Comparison to planar Mn_2O_3 electrodes was performed in order to confirm that electrospun structures have higher capacitances than planar structures that have otherwise been treated identically. Electrospun structures were determined to exhibit universally higher areal capacitance compared to spin cast films prepared from the same solutions due to the increased surface area and decreased dead volume of the freestanding fiber structures. While the maximum performance of $560 \mu\text{F}/\text{cm}^2$ was observed with an 8 % $\text{Mn}(\text{ac})_2$ / 20 % PVP solution, the film electrode fabricated from the same solution had an average areal capacitance of only $49 \mu\text{F}/\text{cm}^2$. The film electrode made from 8 % $\text{Mn}(\text{ac})_2$ / 8 % PVP fared only slightly better, with a capacitance of $82 \mu\text{F}/\text{cm}^2$, as compared to $389 \mu\text{F}/\text{cm}^2$ for its analogous web electrode. The improved performance of the low-PVP film is due to more uniform film quality during spin casting and calcination, owing to the relatively lower viscosity of the solution allowing for a more uniform dispersion on the substrate. Although the effects of solution composition are not consistent with those observed in the electrospun structures, when method of deposition is the only variable changed, electrospinning results in a remarkable capacitance increase over spin-cast films.

Average areal capacitance values for the nineteen standards tested range from 55 to $560 \mu\text{F}/\text{cm}^2$, which is several orders of magnitude lower than literature values reported for Mn_2O_3 thin film and nanofiber-based electrodes.^{122,123} The performance is attributed to relatively poor

charge transfer through the charge collecting substrate to the electrode surfaces, as well as low active mass. Mass loading in the freestanding electrodes is much lower than that observed with traditionally-processed nanofiber and nanoparticle-based electrodes, leading to decreased capacitance from fewer active sites. Thin film electrodes have low active mass but superior electrical properties; as increasing active mass via deposition time was not observed to have a strong effect on areal capacitance, improving electrical properties of the electrospun web electrodes may provide a more effective route to optimization.

Maximum performance of the web electrodes fabricated within the scope of the study on fabrication parameters was from 20 % PVP/ 8 % Mn(ac)₂, 30 min deposition, and 240 min calcination (standard 14). The average capacitance for the set of conditions measured 560 $\mu\text{F}/\text{cm}^2$ at 25 mV/s, which was 44 % greater than the next-highest value of 389 $\mu\text{F}/\text{cm}^2$, documented for 8 % PVP / 8 % Mn(ac)₂, 30 min deposition, and 240 min calcination (standard 13). The conditions used to produce the highest-performing electrodes are consistent with the statistical evidence that polymer concentration has the weakest effect on performance, as all resulting morphologies demonstrated high surface roughness, while calcination time has the strongest effect. Because electronic properties are one of the most significant limiting effects for manganese oxide electrodes, the improved crystalline and physical structure resulting from longer calcination translates to significantly better performance. Therefore, to produce high-performance electrospun electrodes, fabrication parameters should include low oxide precursor concentrations, high polymer concentrations, long electrospinning times, and calcination times of at least 4 h. Further testing is necessary to determine the optimal calcination time, past which detrimental effects from surface area loss via smoothing and intermelting negate the positive electronic effects.

3.2. Calcination Environment

3.2.1. Environment Pressure

By manipulating the pressure under which the ceramic structures are fabricated, the oxygen partial pressure and therefore oxidation state of the metals within the ceramics can be altered. Examination of fibers produced in air under different calcination pressures by XRD reveals a shift in composition from Mn_2O_3 to Mn_3O_4 with decreasing pressure (Figure 22).

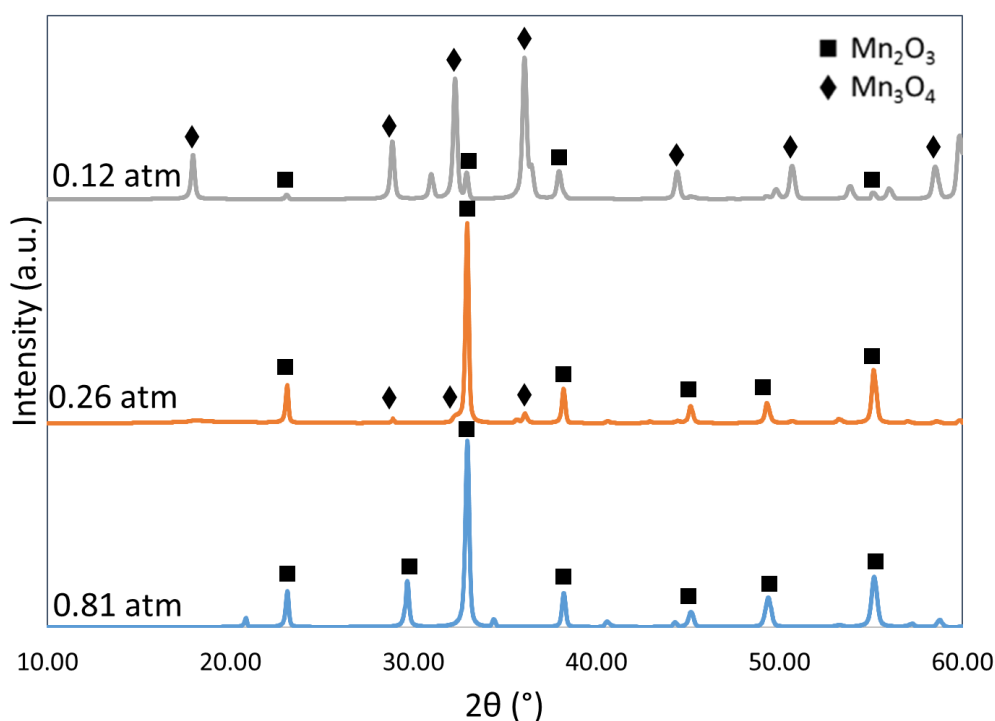


Figure 22: XRD diffractogram for MnO_x prepared under different calcination pressures for 4 h calcination times, showing the effect of calcination pressure on composition.

At 0.81 atm, the fibers exist as single-phase Mn_2O_3 , while the 0.12 atm condition results in nearly-pure Mn_3O_4 with 3.5 % Mn_2O_3 remaining. Fibers calcined at an intermediate pressure, 0.26 atm, consisted of 70 % Mn_2O_3 and 30 % Mn_3O_4 and display the major diffraction peaks of both phases. Because the changes in reaction kinetics at different atmospheric pressures were uncertain, multiple calcination times between 0.5 and 4 h were tested to ensure that the effects of

varied atmospheric pressure were thoroughly observed. Calculated fiber compositions did not change between the 0.5 h and 4 h calcination times, but crystallite sizes as calculated by the Williamson-Hall method increased from approximately 80 Å to 280 Å, respectively.

Examination of fiber morphology at different calcination times and pressures reveals trends towards decreasing surface area with increased time and pressure. For all pressure conditions, surface roughness at the nanoscale decreases with longer times at temperature (Figure 23).

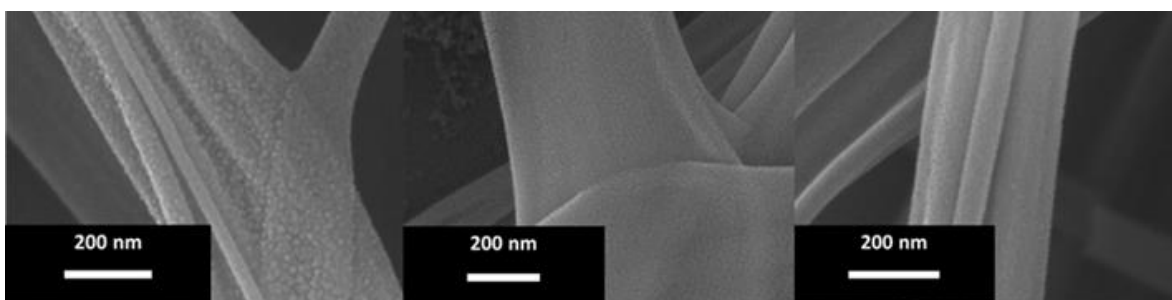


Figure 23: Surface detail of electrospun MnOx fibers calcined at 0.12 atm for (left) 0.5 h, (center) 2 h, and (right) 4 h, showing decrease in surface roughness after 0.5 h.

The oxide structure forms prior to polymer burnout, with densification necessarily occurring primarily after the polymer has been removed. While the oxide structure is limited during formation by existing locations of acetate molecules within the electrospun fibers, extended time at high temperature provides thermal energy for mass transport, driving the structures toward the lowest interfacial energy configuration of a smooth surface. The greatest difference in qualitatively observed surface roughness occurs between 0.5 h and 2 h, with only a minor decrease in roughness between 2 h and 4 h. High surface roughness observed at the shortest calcination time will result in increased electrochemical capacitance owing to the greater accessible surface area per volume of active material.

While pressure during thermal treatment does not have a significant effect on nanoscale surface features or roughness, micro-scale and cross-sectional morphology of the calcined fibers changes dramatically between the 0.81-atm and 0.26-atm conditions, where it remains consistent for the 0.12-atm condition (Figure 24).

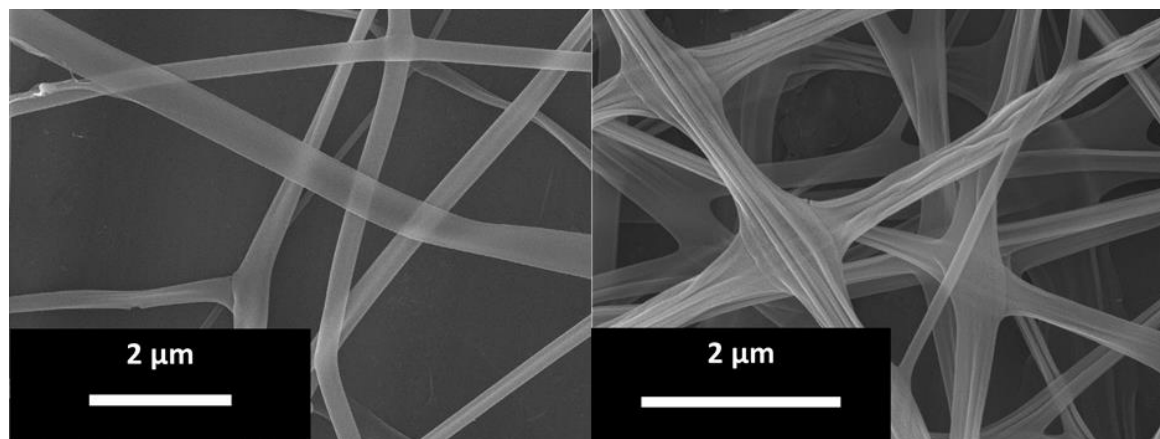


Figure 24: Electrospun MnOx fibers calcined for 0.5 h at (left) 0.81 atm and (right) 0.12 atm. Calcination at atmospheric pressure results in a smooth fiber and round cross-section, while sub-atmospheric pressures result in wrinkled fiber surfaces and flattened cross-sections.

Calcination at sub-atmospheric pressures results in a “collapsed” cross-section, as the reduced pressure in the calcination chamber causes faster evaporation of residual solvent and allows a skin to form on the outer sheath of the fibers. Further oxidation completely removes the carrier polymer, significantly decreasing the overall volume and drawing the partially solidified layer inwards. The ribbed morphologies of the fibers prepared at low pressures have major lateral dimensions slightly greater than the diameters of fibers prepared at atmospheric pressure (322 nm as compared to 296 nm) as the result of the flattened at fiber junctions, where the fibers are fixed into place prior to collapsing. Samples were imaged on a flat plane, so average fiber diameter increases slightly for the irregular cross-sectional morphologies. The collapsed fibers display greater surface-area-to-volume ratio, as a circular cross-section represents the lowest

geometrically-possible surface area for a fiber. Alongside changes in cross-sectional morphology, modifications to calcination pressure result in shifting oxidation state within the MnO_x ceramic fiber. At 0.81 atm calcination pressures, XRD shows only the presence of Mn_2O_3 . With decreasing oxygen partial pressure during ceramic processing, Mn^{2+} in the acetate precursor is barred from complete conversion to the higher oxidation state Mn^{3+} , and fiber composition shifts to include Mn_3O_4 , which has a higher conductivity and lower capacitance than Mn_2O_3 .¹²⁴

CV profiles for all tested calcination conditions were collected from composite electrodes at different scan rates and used to compare the relative performances of MnO_x composite electrodes with defined areas of 0.420 cm^2 . CVs collected for 0.5 h calcination conditions did not exhibit defined redox peaks at any pressure. For samples calcined for 2 h and 4 h at 0.81 atm, slight oxidation peaks were evident around 1 V, with poorly resolved reduction peaks appearing at slow scan rates (25 and $50 \text{ mV}\cdot\text{s}^{-1}$) around 0.76 V. Fibers prepared at 0.12 atm displayed redox peaks at slightly higher voltages, around 1.1 V and 0.8 V. Fibers calcined at 0.26 atm (Figure 25) displayed behavior like those prepared at 0.81 atm, consistent with their high Mn_2O_3 content as determined by XRD.

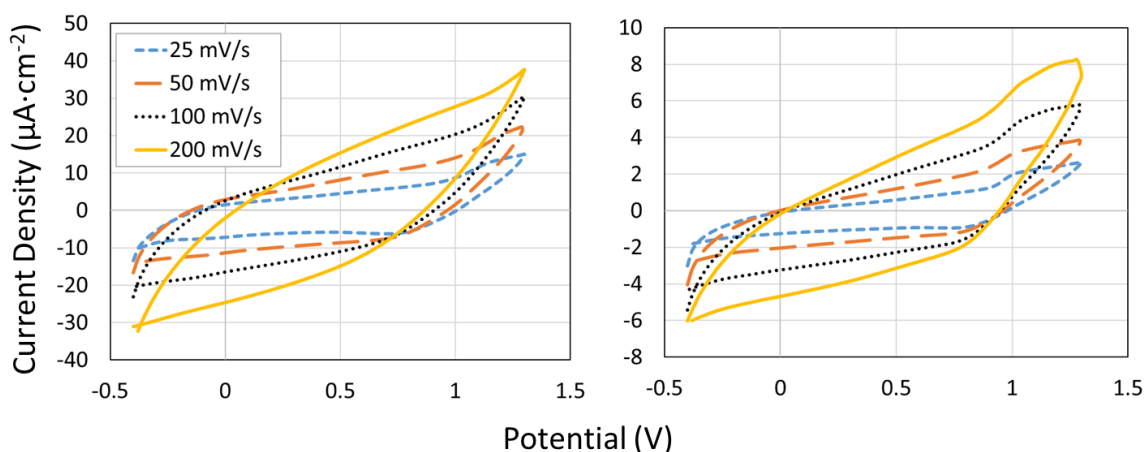


Figure 25: Cyclic voltammograms of fibers calcined for 0.5 h (left) and 4 h (right) at 0.26 atm, showing typical shape profiles observed. Electrode potential is vs Ag/AgCl.

Minor redox peaks are present in the around 1 V during charging of the 4 h samples, which were not observable over the limited voltage range tested in previous sections. The appearance of redox peaks at longer treatment times may be attributed to a more highly-ordered crystalline structure from the longer annealing time, facilitating charge transfer within the structure.¹²⁵ Average specific capacitance for each sample (C_s , F/g) was calculated from 100 $\text{mV}\cdot\text{s}^{-1}$ CV scans according to

$$C_s = \frac{\int(iv)dv}{\mu m \Delta V} \quad (2)$$

where i and v are current (A) and voltage (V), respectively, as recorded during the test, μ is the scan rate ($\text{V}\cdot\text{s}^{-1}$), m is the mass (g) of MnO_x in the electrode, and ΔV is the voltage window (V) during the scan. Because of the asymmetrical shapes of the voltammograms, the integral was taken over both the forward and reverse scans (Figure 26).¹²⁶

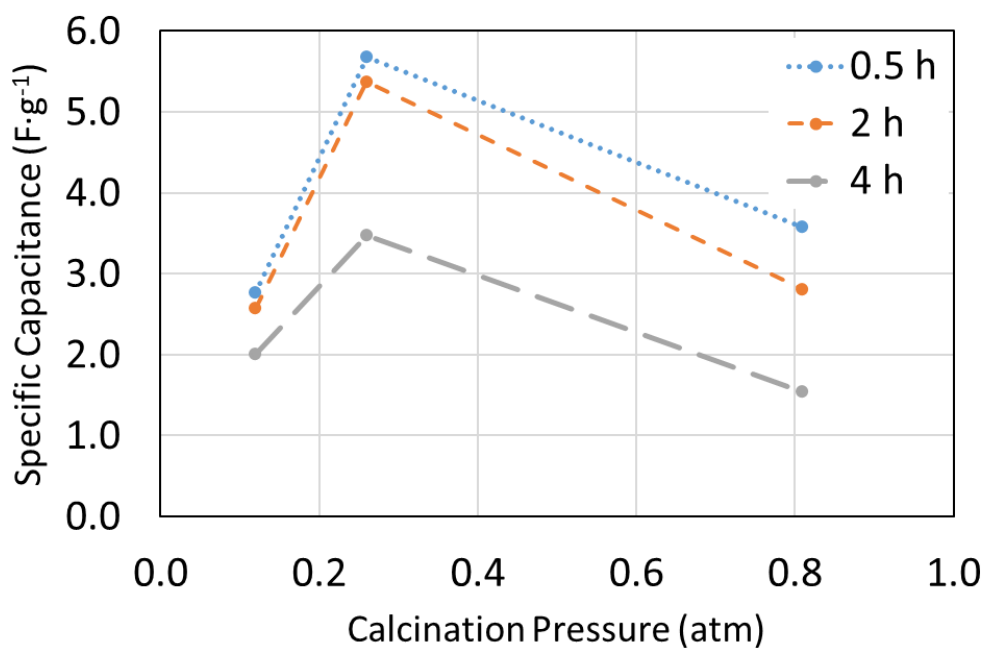


Figure 26: Specific capacitance values of composite MnO_x electrodes prepared under varying conditions. Capacitance decreases with increasing calcination time and shows increased performance at a moderate calcination pressure.

At all pressures, the highest specific capacitance occurred at the 0.5 h calcination condition, presumably due to the increased surface area as observed with SEM. Although the most significant smoothing was observed between 0.5 h and 2 h, the 2 h electrodes exhibited only slightly decreased performance as compared to the 0.5 h electrodes. Because the fiber structures were tested as composite electrodes, any conductivity improvements resulting from longer calcination time were rendered negligible by the high-conductivity matrix of the electrode. The surface smoothing and corresponding decrease in surface area therefore became more significant, resulting in a calcination time / capacitance trend opposite that observed in Section 3.1.3. The highest specific capacitance for each calcination time was observed for the mixed-phase oxides produced at 0.26 atm, an effect that has been previously observed for mixed-

phase MnO_x .¹²⁷ While Mn_3O_4 has a higher conductivity and Mn_2O_3 exhibits greater specific capacitance, the presence of both in a single structure results in a lowered charge transfer resistance and balances the properties of the two to result in a material that has superior electrochemical performance than either of the individuals. The specific capacitance of the fibers composed primarily of Mn_2O_3 (0.81 atm) and Mn_3O_4 (0.12 atm) is not wholly consistent with the expected relatively higher capacitance of Mn_2O_3 , and in fact the primarily Mn_2O_3 electrode prepared at 4 h calcination time exhibits a lower specific capacitance than the primarily Mn_3O_4 electrode calcined for the same length of time. The lack of strong trends in the highest and lowest-pressure calcination conditions may be due to the changes in gross fiber morphology previously discussed. At sub-atmospheric calcination pressures, an increase in specific surface area from fiber collapse was observed; as the effect may not be controlled discretely from fiber composition, the relative effects of material and fiber cross-sectional morphology can not be simply separated.

The highest observed specific capacitance of $5.68 \text{ F}\cdot\text{g}^{-1}$ is low compared to literature values for manganese oxides.¹²⁴ The thickness of the composite layer on the Ni mesh substrates was necessarily much greater than the actual depth of interaction volume between the electrode and electrolyte; however, the total mass of MnO_x in the exposed area of the electrode was used for calculation. The overestimation of mass was used for more accurate comparison among the tested conditions but does not allow for representative comparison to literature values. Additionally, pinholes in the prepared composite electrodes allowed for short-circuit conductivity pathways and decreased the measured capacitive values. Although the electrospun fibers exhibit relatively low performance, atmospheric pressure testing should be conducted on

freestanding web structures to determine whether the mixed-phase oxide continues to elevate performance.

3.2.2. Environment Composition

Manipulation of the oxygen partial pressure during calcination was used to increase the oxidation state of the manganese oxide electrodes. Where calcination at low pressure provided a low pO_2 to decrease oxidation state in the ceramic, calcination under flowing O_2 gas provided a constant high pO_2 to the system and resulted in formation of Mn^{4+} , or MnO_2 (Figure 27).

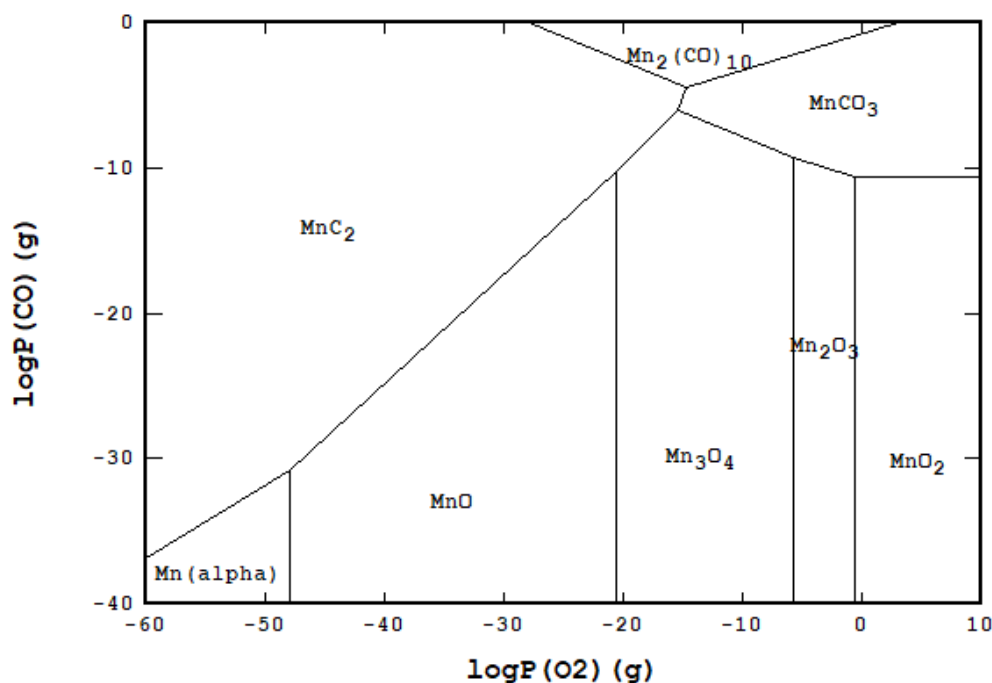


Figure 27: Phase stability diagram for Mn-C-O at 450 °C. Diagram produced with StabCal thermodynamic equilibrium software.

According to phase stability diagrams for the Mn-C-O system, MnO_2 is the thermodynamically stable phase at 450 °C when the oxygen partial pressure is 1, which is attained by calcining the electrodes under pure flowing oxygen. However, the electrodes must be heated to over 500 °C to remove all the carrier polymer from the system, so Mn_2O_3 is formed

initially and then converted to MnO_2 by a longer calcination at $450\text{ }^\circ\text{C}$. As temperature is decreased for the system, MnO_2 becomes stable at lower oxygen partial pressures and becomes a more dominant system component compared to Mn_2O_3 , but the conversion reaction kinetics are slowed.

First, the electrospun fibers were calcined under flowing O_2 for 30 min at $600\text{ }^\circ\text{C}$ prior to a 5 h calcination at $450\text{ }^\circ\text{C}$. The resulting morphology was examined to determine whether the environment composition affected physical structure (Figure 28).

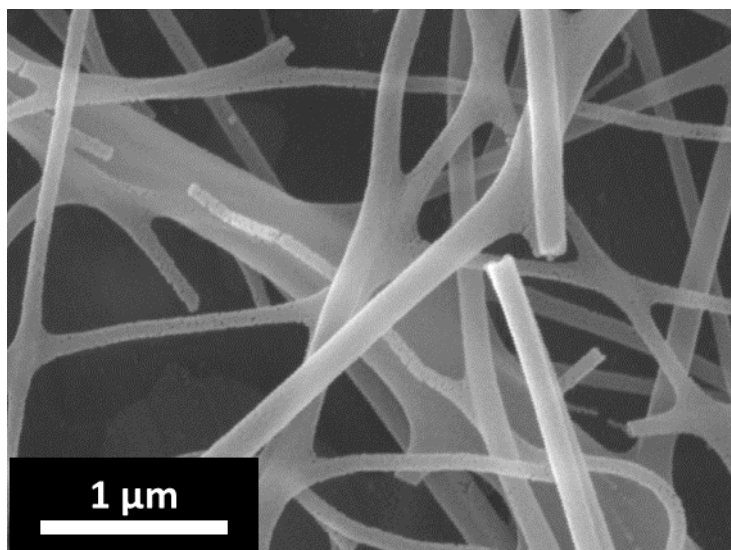


Figure 28: SEM showing electrospun fibers calcined in pure oxygen for 30 min at $600\text{ }^\circ\text{C}$ and then 5 h at $450\text{ }^\circ\text{C}$. Fibers exhibit smooth morphologies and minimal porosity.

The fibers had mostly smooth morphologies, with some porosity visible in the smallest fibers. Although low-diameter fibers had the roughened, porous and segmented morphologies anticipated for oxide fibers, the smooth morphology observed in the larger fibers is characteristic of polymer fibers and suggests that 30 min at $600\text{ }^\circ\text{C}$ was not sufficient to fully remove the polymer. Additionally, XRD on the powder-processed materials treated under the same conditions showed only Mn_2O_3 , so the 5 h low-temperature treatment was not sufficient to

convert a detectable amount of the Mn_2O_3 produced during the polymer removal step to MnO_2 . To solve the issues, time was increased for both the initial polymer removal step and the second, lower temperature phase conversion step. A calcination program with 2 h at 600 °C and then 8 h at 450 °C was tested for its effect on morphology (Figure 29) and composition (Figure 31).

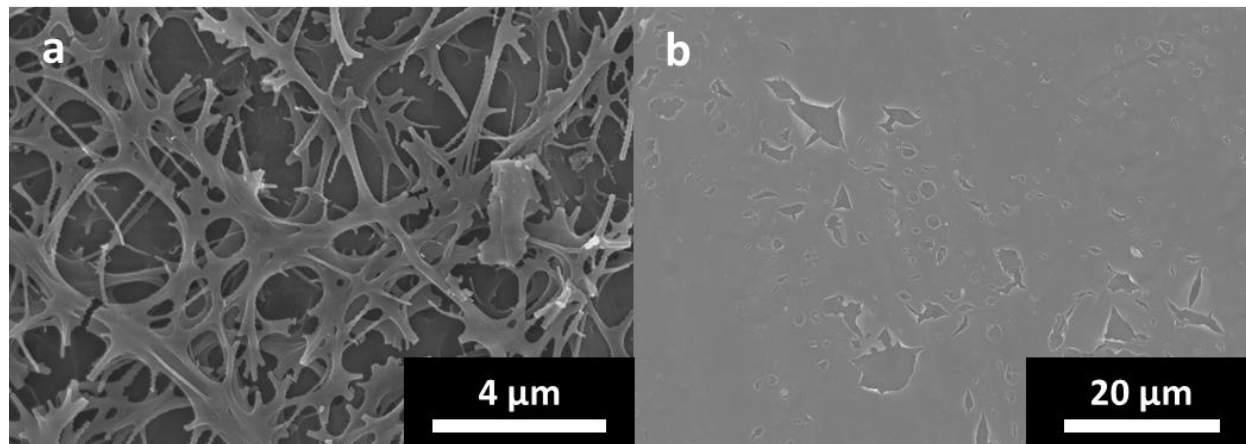


Figure 29: SEMs showing manganese oxide electrodes after an 8 h calcination in O_2 at 450 °C. (a) Semi-melted fibers observed throughout fiber mat. (b) Fully melted film-like morphology observed at center of fiber mat. Similar morphologies were observed for fiber mats calcined with the same heating program in air.

After 2 h, the fibers exhibited morphological features characteristic of oxide fibers such as roughening, fractures, and porosity, indicating that the 2 h calcination at 600 °C is sufficient to remove the polymer from the fiber structures. However, the 8 h calcination at 450 °C caused the fibers to melt and lose their fibrous structure either partially or completely. Towards the centers of the fiber mats, where fiber density is greatest, complete intermelting occurred, with a filmlike morphology observed. Further towards the edges of the electrospun fiber mats, some fibrous structure was maintained, but a large amount of fiber intermelting resulted in an electrode structure that was primarily film-like (Figure 30).

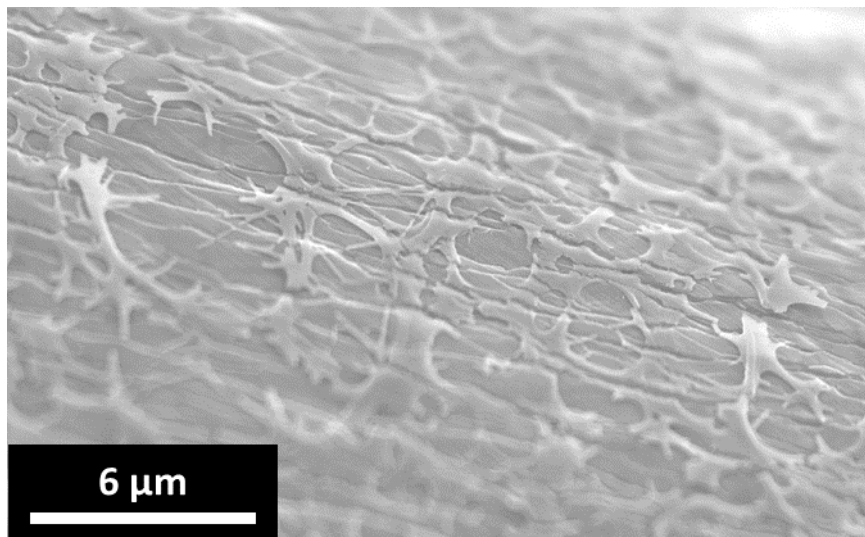


Figure 30: SEM showing oblique view of mixed fiber-film morphology observed after long calcination in oxygen.

The melted fibers are overlaid onto a melted film of manganese oxide and do not form any sort of continuous or freestanding structure; thus, the surface is anticipated to have the energy storage qualities of a roughened film rather than the ultrahigh surface area and permeability of a fiber web. The long calcination step is therefore undesirable from a structure standpoint. However, the longer time at low temperature allows enough time for some conversion to MnO_2 . The oxide phase was confirmed with XRD performed on powder-processed oxide formed by calcining well-mixed PVP and $\text{Mn}(\text{ac})_2 \cdot 4\text{H}_2\text{O}$ in the proportions used for electrospinning (Figure 31).

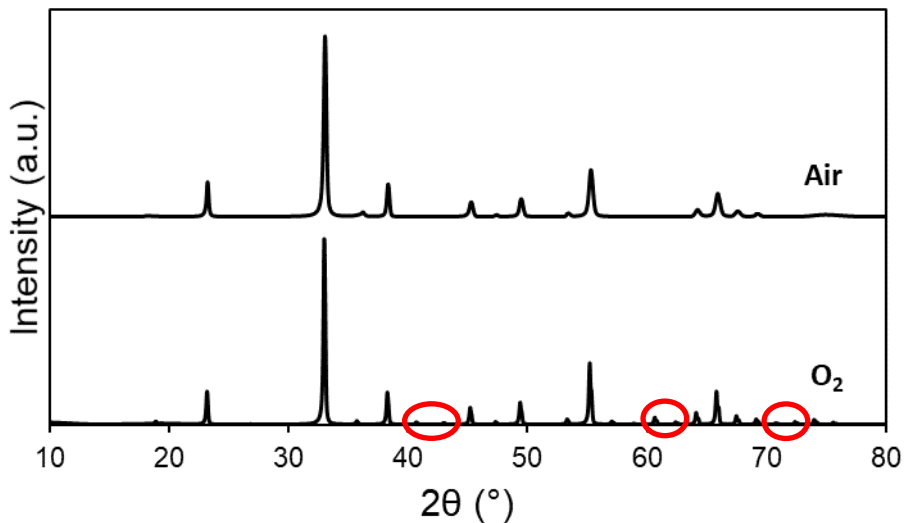


Figure 31: X-ray diffractograms of active material calcined in air and in a pure O₂ environment showing additional MnO₂ peaks (red circles).

While the diffractograms are highly similar, the powder treated in a high-oxygen environment has additional peaks between 40 – 45 ° and 60 – 75 ° which are indexed to MnO₂. Quantitative analysis indicated approximately 5 % MnO₂ with balance Mn₂O₃, but the fiber mats likely contain a higher proportion of MnO₂ due to the smaller particle size allowing for a greater oxidation depth. Approximately 80 % of the existing MnO₂ in the structure is manganite, MnOOH, with the remainder of the MnO₂ existing as β-MnO₂, the lowest-performing MnO₂ structure.¹²⁸ Manganite and β-MnO₂ have identical structures, with the exception of the H in the manganite,¹²⁹ and because the electrodes are used in an aqueous environment where the hydrogen bonds present during dry testing will be overcome, the two structures are assumed to have essentially similar capacitances. In order to produce a higher-performance phase of MnO₂ such as α- or δ-MnO₂, which have lattice configurations better able to accommodate ion intercalation for faradaic energy storage, more intensive processing than simple thermal treatment in an oxidizing environment may be necessary.

Because initial oxidation above 500 °C is necessary to remove the polymer from the structures, initial formation of Mn_2O_3 is unavoidable, but a longer subsequent calcination at 450 °C oxidizes the structure surfaces to MnO_2 . Because both Mn_2O_3 and MnO_2 are semiconductors with similar low electrical conductivities, it was anticipated that the surface oxidation of fibers would result in improved energy storage owing to the superior pseudocapacitive properties of MnO_2 , without a significant effect on the overall electrode resistance. However, electrochemical characterization showed that areal capacitance of the electrospun fiber electrodes was not affected by the oxygen treatment (Figure 32).

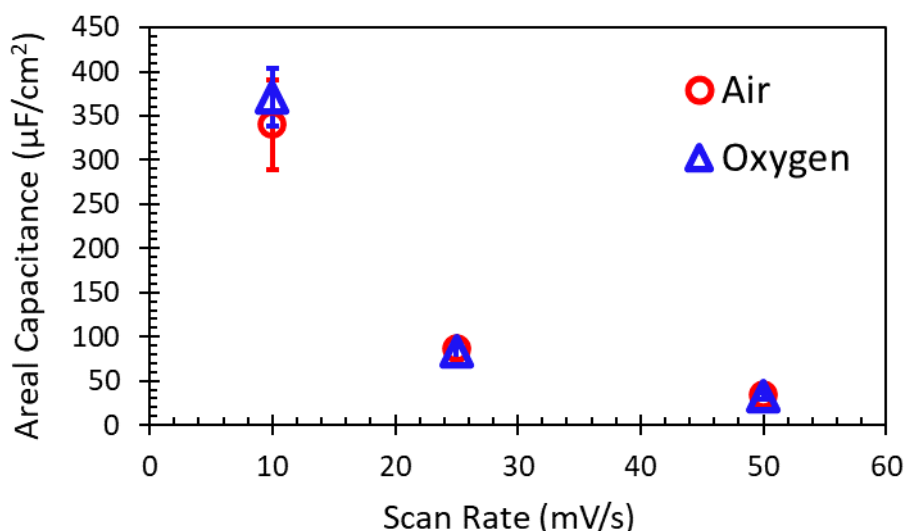


Figure 32: Areal capacitance of electrospun electrodes calcined in air and oxygen for 8 h at 450 °C, as calculated from cyclic voltammograms. Error bars show 95 % confidence intervals.

Although the oxygen-calcined fiber mats have very slightly higher capacitance at the lowest scan rate of 10 mV/s, the difference is not statistically significant as the average values for each data set are within the confidence intervals of the others. The air-calcined fiber mats have slightly higher capacitances at all other scan rates (including 100 and 200 mV/s, which are not displayed) but the differences between the conditions are similarly insignificant. At scan

rates of 25 mV/s and above, the standard deviations and resulting confidence intervals are so small as to not be visible past the markers in Figure 32, which indicates strongly that there is no difference in the performance of electrodes with surface oxidation to MnO₂.

Even with conversion to β -MnO₂ instead of a higher-performance phase, a difference in performance between Mn₂O₃ and MnO₂ electrodes should be evident. The nearly identical performances of the two conditions indicate that the bulk matrix properties, rather than the surfaces, act as the primary limiting factors controlling electrode energy storage performance. Controlled calcination in oxidizing environments to convert the fiber surfaces to higher-performing phases is unlikely to improve performance of the web electrodes, even with improvements to the procedure.

3.3. Post-Processing of Electrospun Electrodes

After electrospinning but prior to calcination, post-processing steps were implemented to improve fiber interconnectivity and adhesion. The goal of post-processing is to improve interfiber bonding to minimize sloughing during calcination and improve the electrical conductivity of the structures. Fiber mats were examined with scanning electron microscopy for the effects of hot pressing and vapor melting on as-spun post-calcination morphologies. All fiber mats were electrospun under identical conditions and exhibited smooth and uniform as-spun fiber morphologies with an average diameter of 264 nm (Figure 33). Electrospun fibers were subjected to vapor melting, hot pressing, or both, and the effect on as-spun morphology was examined.

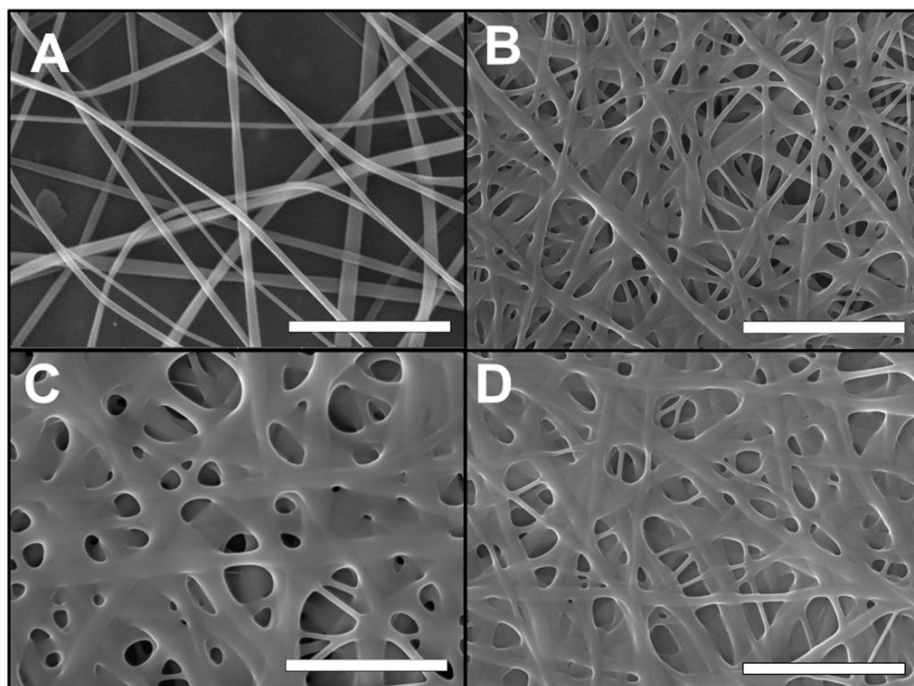


Figure 33: SEMs of electrospun PVP/ $\text{Mn}(\text{ac})_2$ fibers. Scale bars 10 μm . (A) as-spun, without further processing. (B) After hot-pressing treatment, showing fiber melting at junctions. (C) After vapor melting, with similar fiber melting. (D) After vapor melting and hot pressing, showing more complete melting of lower fiber layers from two melting steps.

Both stabilizing treatments caused a small degree of fiber melting at junctions without gross changes to fiber morphology; however, hot pressing caused delamination of fiber layers within the mats, leaving a reduced fiber mat thickness and fiber density. Fiber mats were then calcined at 600 °C for 120 min to remove the carrier polymer and convert the precursor, $\text{Mn}(\text{ac})_2$, to crystalline oxide. The effects of the various pre-calcination treatments on final ceramic fiber morphologies were observed with SEM (Figure 34).

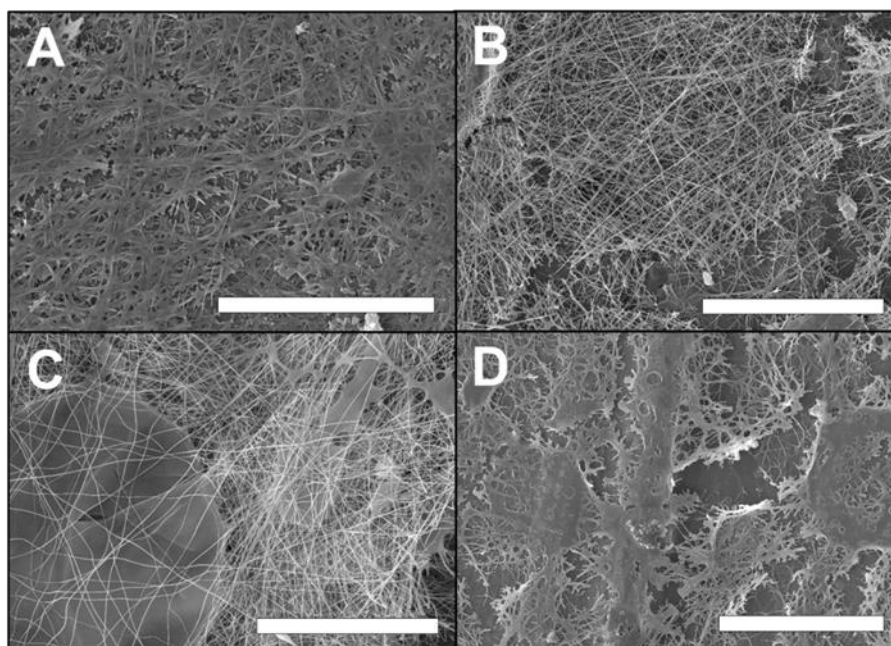


Figure 34: Micrographs of calcined fiber mats after various post-electrospinning treatments. Scale bars 20 μm . (A) no post-spinning treatment; (B) hot pressed; (C) vapor-melted; (D) vapor-melted and hot-pressed.

Hot pressing resulted in oxide fibers that were physically bonded at junctions but retained their individual structures. The large-scale damage to the mats remained after calcination, and lower fiber density was evident compared to the untreated and vapor-melted mats. Fiber structure in the vapor melted samples was similar to the hot-pressed samples, with melted junctions but largely discrete fibers. On the larger scale, however, the vapor melted fiber mats had circular, smooth regions of oxide present over the surfaces, which are formed during vapor melting as condensation begins to nucleate on the surfaces of the samples.^{130,131} Upon calcination, the regions melted together completely to form effectively planar, round oxide areas. Although the smooth regions present lower specific surface area than fiber-based structures and are therefore less desirable for energy storage applications, the majority of the electrospun fibers retained their structures throughout the vapor melting and calcination treatments. The resulting fiber mat, composed of circular melted regions interspersed with densely packed fibers, therefore possesses

specific surface area comparable to that of the untreated fiber mats. Mats that were subjected to both hot pressing and vapor melting, in either order, had relatively smaller amounts of oxide present on the surface due to fiber removal during hot pressing. The fibers that were present had a largely interconnected structure, with some discrete fibers and some regions of nearly planar oxide. Samples that were initially vapor melted and subsequently hot pressed had a visibly greater mass of oxide present than those that were treated in the reverse order, but the two conditions exhibited similar morphologies.

Fiber mats that were calcined without further processing experienced a seemingly greater degree of melting and loss of discrete fiber morphology during the calcination process than those that were vapor melted or heat treated. It is hypothesized that while hot pressing and vapor melting caused slight intermelting of the polymer regions of the electrospun composites as observed in Figure 1, acetate-rich regions of the fibers remained relatively unaffected. Previous thermogravimetric analysis of the PVP - $\text{Mn}(\text{ac})_2$ system has shown that the acetate precursor is not converted to the oxide form until approximately 290 °C (Figure 9), so hot pressing at 120 °C affects only the polymer phases of the fibers. As such, the post-spinning treatments improved stability of the fiber mats through modification of polymer-rich regions only, with negligible migration of the ceramic precursor from the initial, discrete fiber structure. Upon calcination, the ceramic precursors sintered into a fiber network, which maintained the overall structure defined by the initially deposited fibers.¹³²

3.3.1. Electrochemical Performance

Electrospun and calcined manganese oxide fiber mats were tested as working electrodes in a standard three-electrode cell using cyclic voltammetry to measure electrochemical capacitance (Figure 35). Values were compared as areal capacitance (F/cm^2), as the overall

performance of the fabricated electrodes is of greater interest than that of the electrospun Mn_2O_3 material, which has previously been reported as a supercapacitor electrode material.^{122,127,133}

Fiber mats were tested as freestanding electrodes without further post-calcination processing.

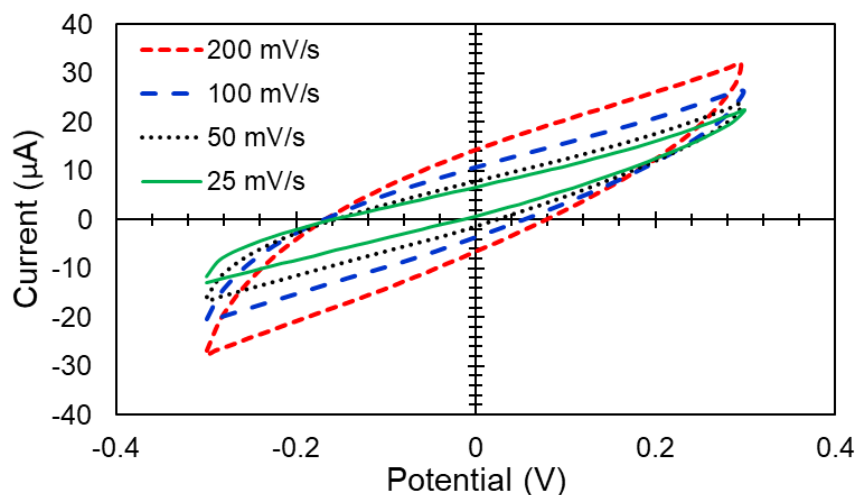


Figure 35: Cyclic voltammogram of a vapor melted Mn_2O_3 fiber mat at varying scan rates. Trace shape is typical of that exhibited for all samples examined from all conditions. Potential is measured vs. Ag/AgCl reference electrode.

Cyclic voltammograms collected at all scan rates had smooth shapes, without redox peaks evident in the potential range measured. The lack of pseudocapacitive activity observed with the Mn_2O_3 electrodes is attributed to the use of acidic electrolyte, as pseudocapacitance in Mn_2O_3 is generally observed in an alkaline environment. Calculated areal capacitance for fiber mats that were calcined as-spun without further processing had an average value of $288 \mu\text{F}/\text{cm}^2$ at $25 \text{ mV}/\text{s}$. With increasing scan rates, the areal capacitance decreased to a minimum measured average of $149 \mu\text{F}/\text{cm}^2$. Vapor melting in a humidity-controlled environment resulted in enhanced performance, with an average capacitance of $45 \mu\text{F}/\text{cm}^2$ at $25 \text{ mV}/\text{s}$, a 57.5 % capacitance increase over the untreated fiber mats. The improved performance is maintained at increasing scan rates. Elevated performance after vapor melting results from an increased

number of charge transfer pathways within the electrode. Because of the low conductivity of bulk manganese oxides, enhanced out-of-plane conductivity of the electrospun structures elevate performance by improving electrical contact to the charge collecting substrate. The fully melted regions provide through-mat stabilization and connection for the fiber mats; by melting fibers from multiple layers together, the physical sloughing of fiber layers upon introduction to the aqueous system or during handling may be reduced. Enhanced stability and interconnectedness through the layers of the fiber mats, with improved out-of-plane conductivity, results in elevated electrochemical performance.

Hot pressing had a deleterious effect on electrochemical performance, with a 14.8 % decrease in measured capacitance at 25 mV/s to 245 $\mu\text{F}/\text{cm}^2$, and similar decreases in performance evident at all scan rates. The poor performance is easily attributed to the loss of bulk fibers during the hot-pressing phase. Fiber mats subjected to both processing steps also exhibited diminished capacity, with a 35.1 % decrease in capacitance to 187 $\mu\text{F}/\text{cm}^2$ observed in the sequential vapor melted-hot pressed sample and a remarkable 49.8 % decrease to 145 $\mu\text{F}/\text{cm}^2$ in the hot pressed-vapor melted fiber mat. An initial vapor melting treatment slightly reduced fiber loss during hot-pressing; as a result, performance is slightly improved over fiber mats that were hot pressed without a vapor phase treatment. The plummeting performance of electrospun mats that were hot pressed prior to vapor melting is attributed to a compounding areal loss. Surface area was reduced by fiber sloughing during hot pressing, and subsequent vapor melting caused destruction of the fiber morphology and reversion to a largely planar film, with additionally decreased surface area. Changes in areal capacitance result from morphological changes, rather than chemical changes to the oxide composition; varying hydration states induced by vapor melting are negated by drying prior to and during initial heating of calcination,

while hot pressing was carried out well beneath the critical temperatures of the oxide precursor. Measured capacitance for the electrospun free-standing electrodes is one to two orders of magnitude lower than literature values that have been reported for Mn_2O_3 thin film and nanofiber-based structures, owing to poor charge transfer through the fiber layers and between the oxide fibers and charge collecting substrate.^{122,123} The limited number of charge transfer pathways and the indirect paths through the electrode thickness prevent efficient charging of the top electrode layers and increase effective conductivity of the structures. By focusing on increasing the packing density of fibers in future work, shorter out-of-plane conductivity pathways will be formed, structure conductivity will increase, and measured capacitance of the structures will improve.

3.3.2. Electrode Wettability

Ensuring a high degree of electrode wettability is critical to maximizing capacitive energy storage. Poor wetting decreases the effective area of the electrode/electrolyte heterojunction, resulting in diminished performance.^{134,135} Wettability of the fabricated electrodes was measured via the contact angle of deionized water on the electrode surface (Figure 36).

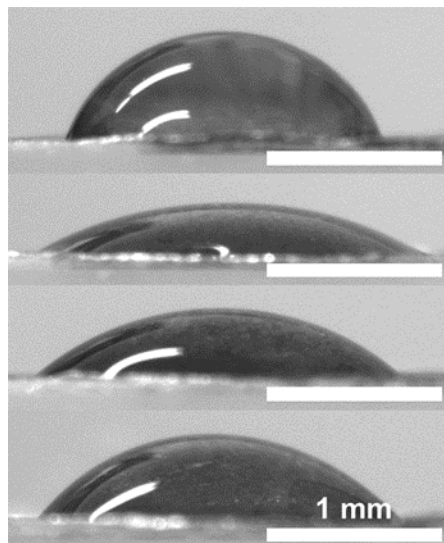


Figure 36: Goniometer images of water droplets on the calcined fiber mats. From top to bottom: untreated mat, 75.3 ° contact angle; vapor melted mat, 26.5 ° contact angle; hot pressed mat, 37.9 ° contact angle, vapor melted and hot-pressed mat, 47.1 ° contact angle.

All post-spinning treatments improved the hydrophilicity of the fiber mats (indicated by a decrease in contact angle), with the greatest improvement observed after vapor melting. Untreated electrodes exhibited an average contact angle of 75.3 °, which decreased to 26.5 ° for electrodes treated with vapor melting prior to calcination. Hot pressing resulted in a 37.9 ° contact angle, while processing with both treatments resulted in an average contact angle of 47.1 °. The improved wettability observed with all post-processing treatments is attributed to larger-scale disruptions in the electrospun mats. While the untreated Mn₂O₃ fiber mats exhibited lower nanoscale surface roughness due to greater fiber melting, hot pressing and vapor melting resulted in decreased effective roughness of the electrodes and thereby increased surface hydrophilicity. Hot pressing removed swaths of fibers and provided routes for water to wick into the electrode surfaces, which improved surface utilization but was unable to counteract the loss of active mass. Although surface utilization was improved, the reduction in total surface area

ultimately resulted in decreased electrochemical performance. Vapor melting resulted in planar regions with low roughness on the scale of dozens of microns, which improved overall electrode wettability and allowed for more effective utilization of the active material surface. The microscale planar regions of the vapor melted mats provide sufficiently smooth surfaces to counteract the high roughness of the interspersing fibers, resulting in an effectively smoother surface and higher wettability. Combined with enhanced out-of-plane conductivity and stability, electrochemical performance is increased over untreated fiber mats, which had the poorest wetting properties and therefore lowest surface utilization. With less contact area between the electrolyte and electrode, the number of storage sites and overall energy storage capacity remained low, but a combination of optimized fabrication as discussed in Section 3.1 with pre-calcination vapor treatment presents a potential route towards improving freestanding web electrode performance.

3.4. Cycling Stability of Freestanding Electrospun Electrodes

Although supercapacitors are known for their exceedingly long cycling lives, pseudocapacitive activity involving oxidation and reduction of the component oxides decreases the long-term stability of the electrode structures. Additionally, high-performance nanostructures are more prone to capacity fading as the ultrahigh surface area of the structures increases side reactions and dissolution rates. Capacity fading is a common problem with manganese oxide-based electrodes due to Mn^{3+} dissolution and lattice deformation with charging and discharging.¹³⁶ Capacity retention for Mn_2O_3 nanostructures after many cycles ranges from over 90 % to less than 20 %, with the number of cycles used to examine stability ranging widely from 15 to 3000.^{133,137–139} For preliminary stability testing, the electrospun Mn_2O_3 electrodes were tested for their stability over 100 cycles at 10 A/g (Figure 37).

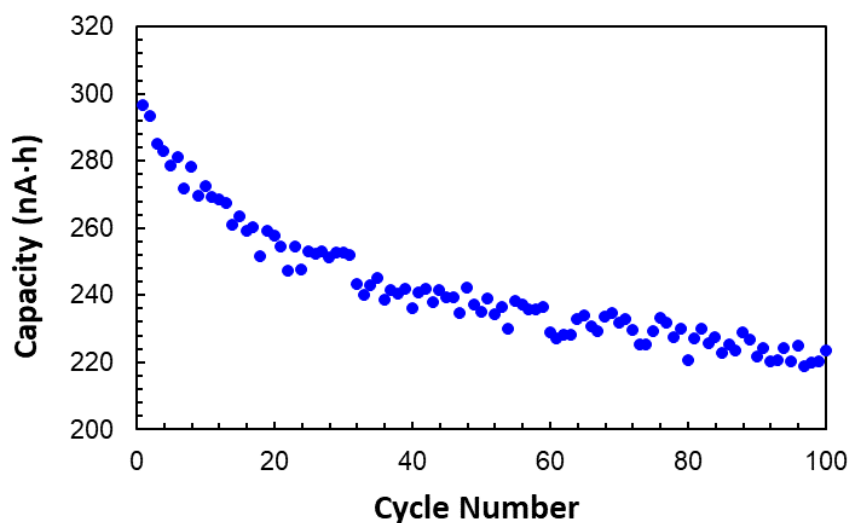


Figure 37: Capacity of an electrospun Mn_2O_3 electrode over 100 cycles at 10 A/g, showing approximately 30 % capacity fading.

After 100 cycles at 10 A/g, the freestanding electrospun electrode demonstrates around 70 % capacity retention, which is comparable to fiber-based nanostructured electrodes in literature. After a sharp initial drop over the first 15 – 20 cycles, the capacity fading slows for the remainder of the tests. Because the surfaces of the electrospun fibers are fully exposed to electrolyte, capacity fading likely results primarily from dissolution and physical breakdown of the unsupported fiber networks. With a greater fiber density or larger fiber diameter, cycling stability may be improved by increasing the mechanical stability and physical support for the nanofibers. Another potential route for improving cycling stability is via processing to improve adhesion between the electrospun fiber network and the charge collecting substrate to reduce physical breakdown of the electrodes.

3.5. Modeling

Lin's model of a porous metal oxide-based supercapacitor was used as the foundation for the model presented herein.⁵⁹ In Lin's model, two $\text{RuO}_2 \cdot x\text{H}_2\text{O}$ nanoparticle-based electrodes are

separated by an ionically conducting separator and H_2SO_4 electrolyte. To adapt the model to the Mn_2O_3 fibrous web-based system described by our work, new equations were derived to describe the faradaic reactions occurring in the electrodes and the geometric relationships between fiber size, porosity, and specific surface area. Temperature, electrolyte concentration, and DL capacitance are assumed to be invariant with potential, and side reactions, leakage, and self-discharge are ignored.

3.5.1. System Parameter Measurement

Physical parameters describing the electrospun electrodes were extracted from EIS scans by fitting models to describe the data (Figure 38).

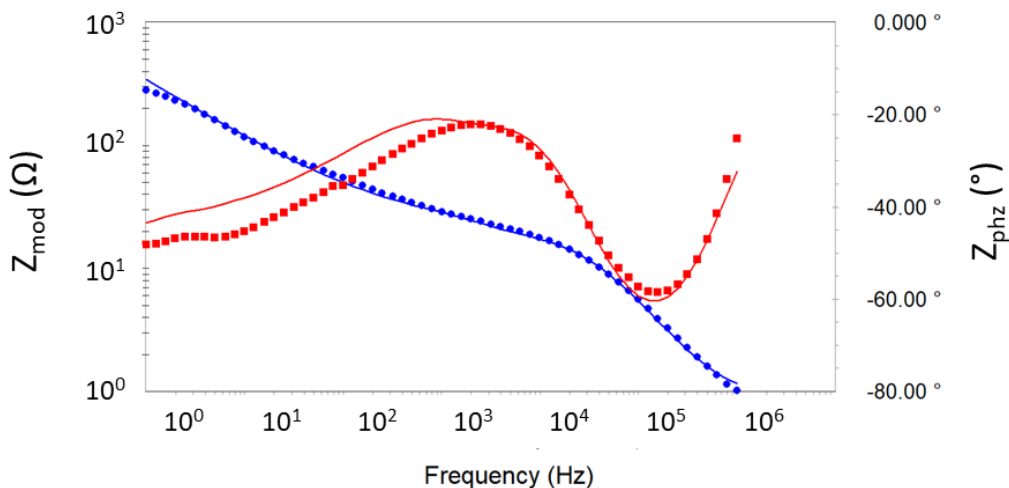


Figure 38: Example of Bode plots describing an electrospun Mn_2O_3 electrode (points) and the models fit to describe them (lines). Blue data corresponds to the primary Y axis, Z_{mod} , and red data corresponds to the secondary axis, Z_{phz} .

In EIS, the complex impedance of the electrode is measured over a range of frequencies, and the changes in impedance are plotted as a function of those frequencies to yield a Bode plot. The primary Y axis, Z_{mod} , describes the change in resistance, while the secondary axis, Z_{phz} , describes the phase shift observed in the complex impedance. The scans are also presented as a

Nyquist plot (Figure 39), where the magnitudes of the real and imaginary parts of the complex impedance are compared.

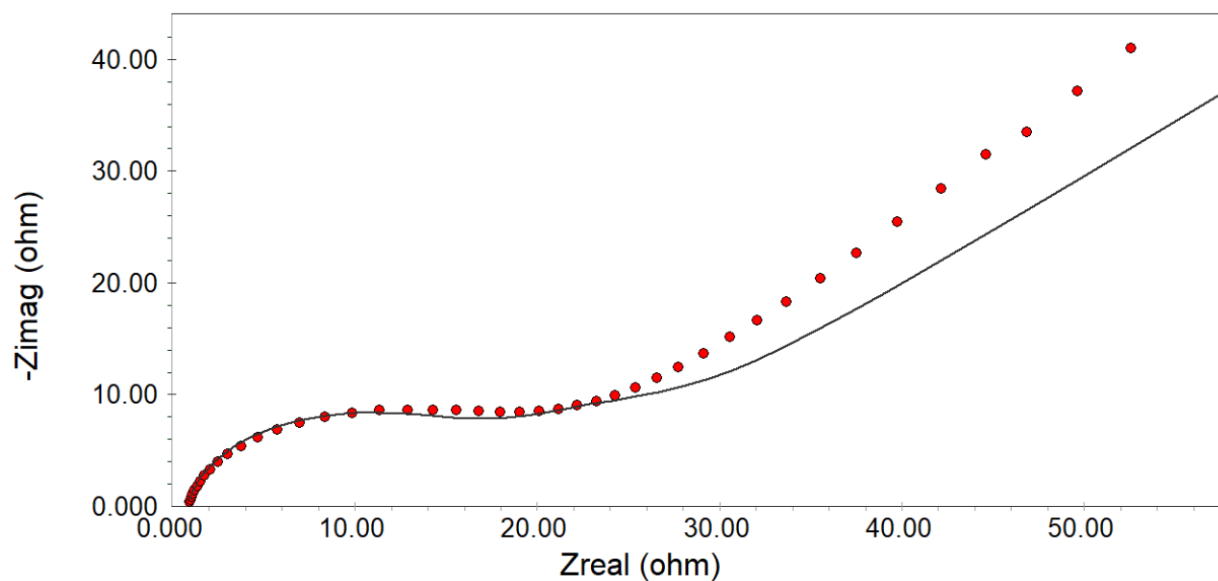


Figure 39: Nyquist plot describing an electrospun Mn_2O_3 electrode (points) with model overlaid (line).

Frequency decreases from left to right on the Nyquist plot, although no explicit frequency data is given. For both the Nyquist and Bode plots, the model fits well in the high-frequency range and departs from the data in the low-frequency range, where kinetically slow effects such as diffusion and chemical reactions become more dominant and are not well-described by the equivalent circuit model (Figure 40).

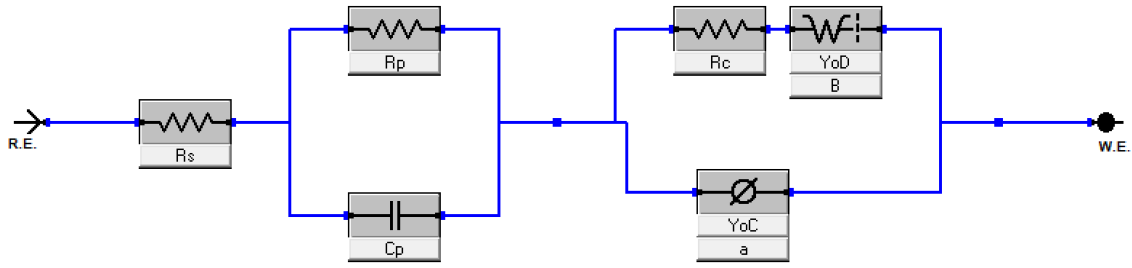


Figure 40: Equivalent circuit model used to describe electrospun electrodes for extracting variables from Bode and Nyquist plots.

In the model, R_s is the solution resistance in the cell, R_p and C_p are an RC component representing double layer capacitance via polarization, and the $R_c / Y_{oD} / Y_{oC}$ component represents the faradaic processes in the system.¹⁴⁰ The Warburg component, with parameter labels Y_{oD} and B , describes diffusion effects in an electrochemical system; a porous bounded Warburg component was used as it describes diffusion within a non-infinite closed electrochemical system with non-planar electrodes at the boundaries. At high frequencies, the Warburg component has little effect, but at low frequencies the Warburg diffusion behavior becomes large. The two parameters, Y_{oD} and B relate to impedance as

$$Z = \left[\frac{(1/Y_{oD})}{\sqrt{(j\omega)}} \right] \tanh[B\sqrt{(j\omega)}] \quad (3)$$

$$Y_{oD} = \frac{1}{\sigma\sqrt{2}} \quad (4)$$

$$B = \frac{\lambda}{\sqrt{D_0}} \quad (5)$$

where Z is impedance, j is $\sqrt{-1}$; ω is radial frequency (s^{-1}); σ is the Warburg coefficient, which is dependent on concentrations and diffusion coefficients of the oxidizing and reacting species,

as well as electrode surface area, temperature, and number of electrons transferred; λ is the Nernst diffusion layer thickness (cm), and D_0 is the average diffusion coefficient of the diffusing species.¹⁴¹

To describe a non-ideal capacitor, a constant phase element (CPE) with parameters Y_0C and a is used in place of a capacitor, with an impedance described by

$$Z = \frac{1/Y_0}{(j\omega)^a} \quad (6)$$

where a is an empirical fitting constant without a well-accepted physical basis.¹⁴² The double-layer capacitance of real cells frequently behaves as a CPE rather than an ideal capacitor by describing inhomogeneity in the surface, but double layer capacitance cannot easily be extracted from a CPE since extensive experimentation is needed to fit a series of curves.¹⁴⁰ To estimate capacitance for the electrospun electrode systems, a second equivalent circuit model was constructed where the CPE is replaced with a simple capacitor. The values for the other model components (R_s , R_p , C_p , R_c , Y_0D , and B) were each locked to the values calculated by the equivalent circuit model presented in Figure 40. The CPE with parameters Y_0C and a was replaced with a simple single-parameter capacitor, and the new component was fit to the data. That value was then taken as the double layer capacitance of the electrode.

Exchange current density for the faradaic reaction and transfer coefficients for the anode and cathode were measured from Tafel plots (Figure 41).

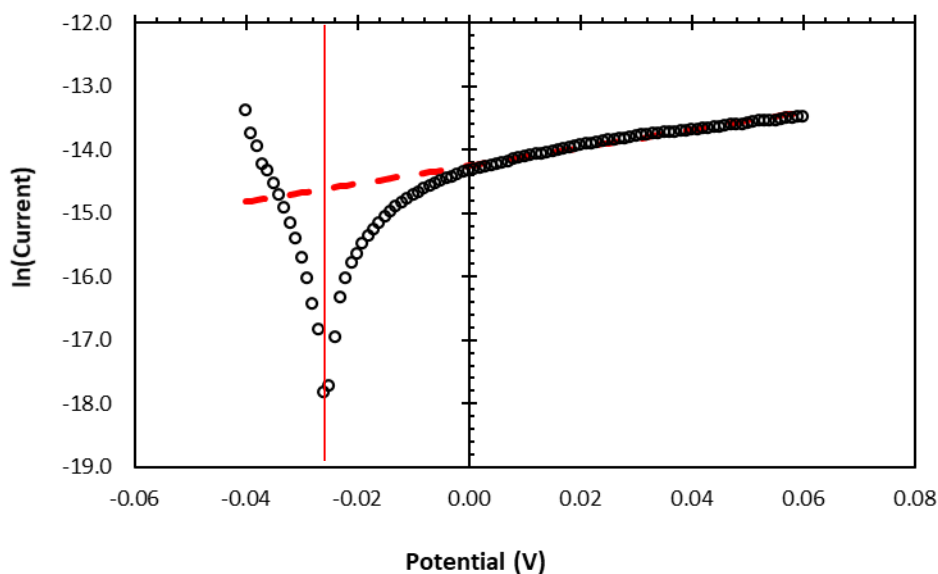


Figure 41: Example of a Tafel plot constructed for a freestanding Mn_2O_3 electrospun electrode. Line of best fit for linear region is shown as a dotted line, and the vertical line indicates the intercept at which exchange current density is measured.

The slope discrepancy between the anodic (left of asymptote) and cathodic (right of asymptote) regions of the Tafel plot is common in functional applications and indicates a difference in polarization resistance between the anodic and cathodic reactions.¹⁴¹ A corrosion voltage of around 30 - 50 mV occurs due to natural variations in mass loading between the two electrodes due to the random nature of deposition in electrospinning. Slight metal ion dissolution at the electrode surfaces forms a concentration cell and causes a corrosion voltage between the electrodes. Exchange current density, i_0 , is taken as the current value where the line of best fit for the linear region intercepts the vertical asymptote of the Tafel plot and was taken as the average of measurements from three cells.

The slopes of the linear regions have an average of 14.165 V/decade, which can then be used to calculate the transfer coefficients for the system according to

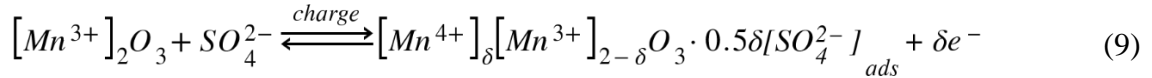
$$\alpha_c = \frac{RT}{nF} \frac{\partial \ln i_c}{\partial E} \quad (7)$$

$$\alpha_a + \alpha_c = 1 \quad (8)$$

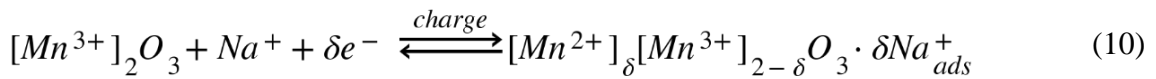
where α_c and α_a are the cathodic and anodic transfer coefficients, respectively; R is the ideal gas constant, T is temperature, n is the number of electrons transferred during polarization, F is Faraday's constant, i_c is the cathodic current, and E is the potential.¹⁴³ The same equation can be applied to calculating the anodic transfer coefficient by taking the Tafel slope of the anodic reaction (left of the asymptote in Figure 41). However, α_c and α_a conveniently sum to 1, necessitating independent calculation of only one of the two.

3.5.2. Model Derivation

The faradaic reactions occurring between the Mn_2O_3 electrodes and the Na_2SO_4 electrolyte during charge and discharge are expressed as



for the positive electrode, and



for the negative electrode, where δ is the state of charge of the electrode. During charging, the reduction of Mn^{3+} to Mn^{2+} in the negative electrode is compensated by sodium ion adsorption from the electrolyte, and oxidation to Mn^{4+} is countered by sulfate ion adsorption.¹⁴⁴ The faradaic transfer current in the system, j_f , is described by the Butler-Volmer equation

$$j_f = i_0 \{ \exp[\alpha_a f (E - U_a)] - \exp[\alpha_c f (E - U_c)] \} \quad (11)$$

where i_0 is the exchange current density of the faradaic reaction; f is equal to $F/(RT)$, with F being Faraday's constant, R the ideal gas constant, and T absolute temperature; α_a and α_c are the

anodic and cathodic transfer coefficients for the reactions, E is the local electrode potential, and U_a and U_c are the equilibrium potentials at the anode and cathode, respectively.⁵⁹ U is a function of the state of charge, which is represented by θ as the fraction of oxidized species in the electrode. To obtain the relationship between state of charge and equilibrium potentials, the charge and discharge curves obtained from LSV are integrated to yield total electrode charge, Q . State of charge (SOC) is then calculated according to

$$\delta = \frac{Q}{2mF} \quad (12)$$

where m is moles of Mn_2O_3 present in the electrode, based on mass.¹⁴⁵ SOC is then plotted against potential between 1 V and 0 V (Figure 42).

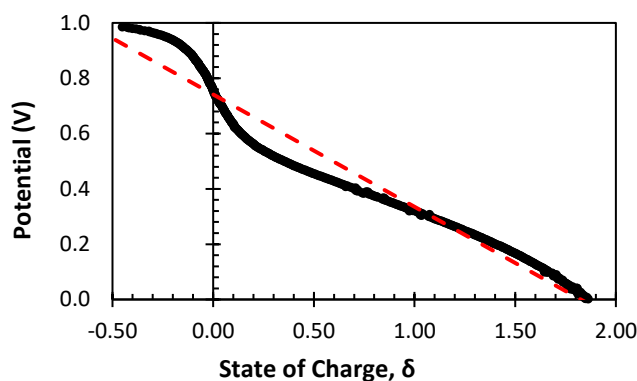


Figure 42: Voltage of Mn_2O_3 electrospun electrodes as a function of state of charge, obtained by integrating the LSV curve, with the linear approximation displayed as a dashed line. State of charge, δ represents the content of oxidized or reduced Mn, as described in Equations 9 and 10.

The curve displayed in Figure 42 shows the change in Mn oxidation state in the positive electrode as it is discharged, where δ is a real number as described in Equations 9 and 10. To approximate the relationship between state of charge and potential, a linear approximation was fit to the curve over the entire range. The inflection point around $\delta = 0$ is due to redox activity in the Mn_2O_3 electrodes, while the approximately linear region at a higher state of charge is

attributed to a constant redox-based capacitance.¹⁴⁵ The negative SOC region indicates that faradaic processes alone are not sufficient to charge the electrodes to 1 V and must be supplemented with double layer capacitance. The linear approximation has an R^2 value of 0.952, which was considered adequate for the purpose of estimating state of charge over the voltage range; however, the inaccuracies in shape around the inflection point at $\delta = 0$ are likely related to the inaccurate shape of the predicted discharge curve.

U_a and U_c are related to fraction of oxidized species by

$$U_a = 0.371\theta \quad (13)$$

$$U_c = 0.371(\theta - 0.406) \quad (14)$$

which is estimated from the relationship between potential and state of charge for an Mn_2O_3 electrode (Figure 42), according to the equation for the linear approximation.^{59,145} Faradaic charge of the electrode relates θ and j_f by

$$\theta = \frac{Q_f - Q_{f,red}}{Q_{f,ox} - Q_{f,red}} \quad (15)$$

$$\frac{\partial Q_f}{\partial t} = s_v j_f \quad (16)$$

where Q_f is the faradaic charge of the electrode, $Q_{f,red}$ is charge of a fully reduced electrode, $Q_{f,ox}$ is charge of a fully oxidized electrode, and s_v is the active surface area per unit volume of the electrode.⁵⁹ The charges of fully reduced and oxidized equations are assumed constant and are calculated according to

$$Q_{f,ox} = \frac{s_v \delta F}{h^2 L_A} \quad (17)$$

$$Q_{f,red} = 0 \quad (18)$$

where h is the lattice length on the surface of the electrode and L_A is Avogadro's number.⁵⁹ State of charge, δ for a fully charged electrode is taken as 2 according to Eq. (9) and (10). Equations (11), (15), and (16) are combined into one of the main governing equations of the model as

$$\frac{\partial \theta}{\partial t} = \frac{s_v i_0}{Q_{f,ox} - Q_{f,red}} \exp\{\alpha_a f(E - U_a)\} - \exp[-\alpha_c f(E - U_c)] \quad (19)$$

which describes rate of change of fraction of oxidized species, or rate of oxidation or reduction.

The second governing equation describes changes in electrode potential through the thickness of the electrode by

$$\frac{\partial^2 E}{\partial \xi^2} = \tau \frac{\partial E}{\partial t} + \frac{\tau}{C_d} j_f \quad (20)$$

where ξ is the dimensionless distance describing spatial location within the electrode; C_d is the double layer capacitance per unit surface area of the electrode, obtained by dividing DL capacitance obtained from EIS curve fitting by the total surface area contained within the electrode; and τ is the double layer time constant of the system. The time constant is further defined by

$$\tau = s_v C_d L^2 \left(\frac{1}{\sigma} + \frac{1}{\kappa_p} \right) \quad (21)$$

where L is the total thickness of one electrode, σ is the bulk conductivity of the electrode matrix, and κ_p is the conductivity of the electrolyte within the pores of the electrode, expressed as

$$\kappa_p = \kappa_0 \epsilon^{1.5} \quad (22)$$

where κ_0 is bulk conductivity of the electrolyte and ϵ is the electrode porosity.⁵⁹ The thickness of the electrode was allowed to vary with changing fiber diameter as

$$L = \frac{L_{obs} D}{D_{obs}} \quad (23)$$

where L_{obs} and D_{obs} are the observed electrode thickness and average fiber diameter, as measured from SEM micrographs. The thickness variation operates under the assumption that a constant number of fiber layers are deposited with changing diameter. The relationship between electrode surface area and porosity is described by

$$s_v = \frac{4(1 - \epsilon)}{D} \quad (24)$$

$$\epsilon = 1 - \left(\frac{\pi D^2 l}{4}\right) \quad (25)$$

where D is fiber diameter and l is the length of fiber deposited in the unit cell during electrospinning. Because the freestanding electrospun morphology prevents any packing of the structures as would be expected with free-flowing nanoparticles, it was necessary to expand the porosity observed in the fabricated electrospun webs to similarly fabricated structures composed of fibers with different diameters. To do so, a constant length of deposited fiber within the unit cell was assumed, which fixes the fibers in space and allows diameters to increase or decrease without affecting the center-to-center fiber spacing. A length value is obtained by solving Eq. (25) for l using the observed porosity and average fiber diameter, which can then be carried forward to calculate ϵ and s_v for any fiber size. Additionally, the diameter that results in zero porosity is calculated and used as the upper limit of D in the model. The unique effect of the fixed-fiber model is that as D increases, specific surface area for a unit cell of the electrode also increases. Without packing, increasing fiber diameter consumes void space in the electrode and

allows for more effective space utilization; however, it is important to note that surface area per fiber volume still decreases with increasing diameter, as is expected from scaling effects.

The boundary and initial conditions were set according to the assumption that at the interface between electrode and current collector ($\xi = 0$), all current arises from the current collector, and at the electrode surface farthest from the current collector ($\xi = 1$), current arises exclusively from the electrolyte phase.⁵⁹ At the $\xi = 0$ interface,

$$\frac{\partial E}{\partial \xi} = -\frac{i_{cell} L}{\sigma} \quad (26)$$

where i_{cell} is the applied or requested cell current density. At the $\xi = 1$ interface, the potential flux boundary is

$$\frac{\partial E}{\partial \xi} = -\frac{i_{cell} L}{\kappa_p} \quad (27)$$

Additionally, it is assumed that the fraction of oxidized species within the electrode, θ , will be constant across the thickness of the electrode, giving the boundary condition

$$\frac{\partial \theta}{\partial \xi} = 0. \quad (28)$$

The initial conditions are set for discharge such that at time $t = 0$, $E = 1$ V and $\theta = 1$.⁵⁹ A complete list of model parameters and their values is presented in Table III.

Table III: List of model parameters used to describe discharge of freestanding electrospun electrodes.

| Parameter | Value | Source |
|-------------|--|---------------------------|
| i_0 | 1.29e-05 A | Measured (LSV) |
| α_a | 0.664 | Measured (LSV) |
| α_c | 0.336 | Measured (LSV) |
| U_a | 0.3710 V | Eq. (6) |
| U_c | 0.371($\theta - 0.406$) V | Eq. (7) |
| $Q_{f,ox}$ | 0.391 C at D = 112 nm | Eq. (10) |
| $Q_{f,red}$ | 0 C | Lin, et al. ⁵⁹ |
| s_v | 2.22e05 cm ² /cm ³ at D = 112 nm | Eq. (17) |
| h | 9.41e-08 cm | Geller ¹⁴⁶ |
| τ | 1.05e-03 s at D = 112 nm | Eq. (14) |

| | | |
|------------|-----------------------------|----------------------------|
| C_d | 1.07e-02 F/cm ² | Measured (EIS) |
| L | 4.08e-05 cm at $D = 112$ nm | Measured (SEM) |
| σ | 1e-05 S/cm | Hong, et al. ⁵⁵ |
| κ_0 | 0.0667 S/cm | Measured (EIS) |
| κ_p | 0.051 S/cm at $D = 112$ nm | Eq. (15) |
| D | Between 100 and 250 nm | Assumed |
| ϵ | 0.8371 at $D = 112$ nm | Measured (SEM) |

With D and i_{cell} as the manipulated variables, and all other model parameters measured or assumed, Eq. (19) and (20) are a system with two equations and two unknowns, E and θ .

Diameters were set between 100 nm and 250 nm to stay below the upper fiber diameter limit of 276 nm, where the structure achieves zero porosity. Current densities between 1 and 5000 A/g were used to examine the effects of increasing power density on energy density of the structures. Local electrode potential and fraction of oxidized species were solved for over defined time ranges at locations throughout the depth of the electrode.

3.5.3. Effect of Fiber Diameter

The electrospun electrodes were imaged with SEM and TEM to examine the structure and morphology of the oxide fibers (Figure 43).

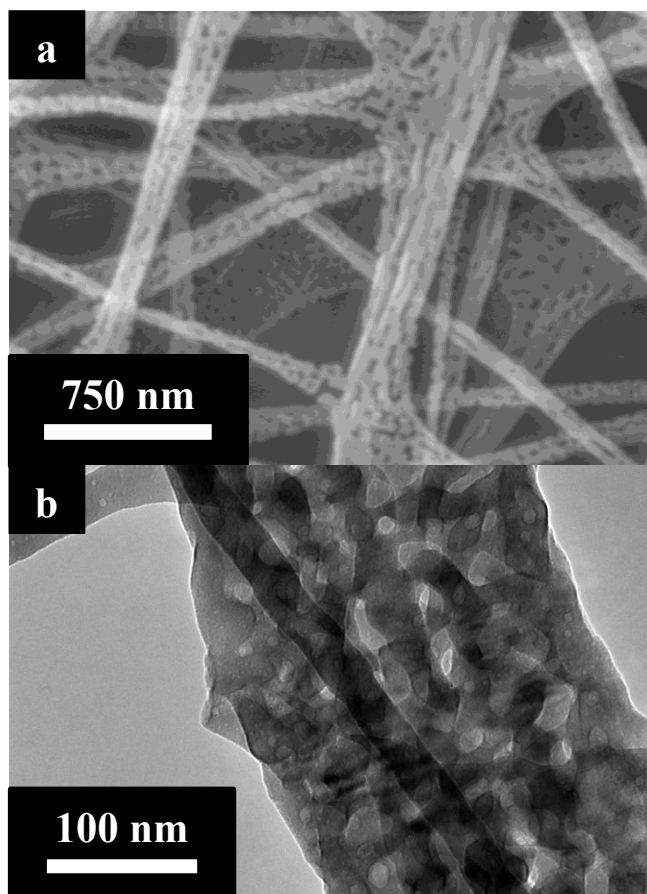


Figure 43: Micrograph images of electrospun Mn_2O_3 fibers. (a) SEM showing fiber porosity and layered structure. (b) TEM showing interior porosity of electrospun oxide fibers.

After calcination, the electrospun fibers demonstrate a highly porous structure. The porosity results from the mechanism of fiber formation during heat treatment. Manganese acetate in the composite electrospun fibers converts to oxide between 260 and 310 °C. During the conversion, regions of $\text{Mn}(\text{ac})_2$ in the fibers form an interconnected manganese oxide network that preserves the fiber morphology upon polymer burnout, which occurs between 400 and 450 °C.¹¹⁹ Further calcination at 600 °C allows full conversion to Mn_2O_3 and densification of the structures. Both SEM and TEM examination reveal a high degree of porosity in the fibers, which is highly desirable for supercapacitor applications due to the additional surface area that the porosity provides. The primary variable manipulated for the mathematical and experimental

model was fiber diameter, D . Discharge curves were simulated between 1 V and 0 V for electrospun fiber mats with changing fiber diameter (Figure 44). Charging curves were assumed to simply be the reflection of the discharge curves.⁵⁹

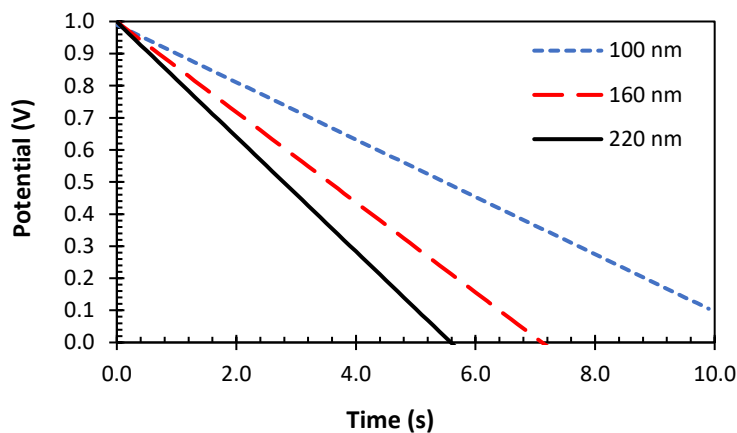


Figure 44: Discharge curves generated from the mathematical model for freestanding web electrodes with fiber diameters of 100, 160, and 220 nm at a current density of 1 A/g. Color available online.

The electrodes exhibit linear discharge to 0 V, with discharge time increasing for decreasing fiber diameter. The linear nature of the discharge curves results from the model combining capacitive and faradaic response from $t = 0$, assuming no change in capacitance or reactivity over time or kinetic delay of the initial faradaic response. As fiber diameter increases, discharge time shortens due to decreased specific surface area relative to active volume. Although fixing the fibers in space causes increased specific surface area of the electrode with increasing fiber diameter, the effect results from consumption of void space between the fibers. The mass-based scaling effect of surface area to volume ratios decreasing with increasing linear dimensions still describes the active volume of the fibers themselves, so as current density is scaled to mass, it is controlled by fiber volume minus void space, rather than the total electrode volume. Because a constant current density was used to simulate real application conditions, the

total cell current applied to the electrodes scales with $1/D^2$ (for cylindrical fibers), while the active surface area scales with $1/D$. Applied current therefore increases more rapidly than energy storage sites and total capacity, so the discharge time must decrease with increasing fiber diameter.

However, the effect of fiber size on discharge time is not solely determined by scaling effects, with a slowed response observed for electrodes with fiber diameters above 230 nm (Figure 45).

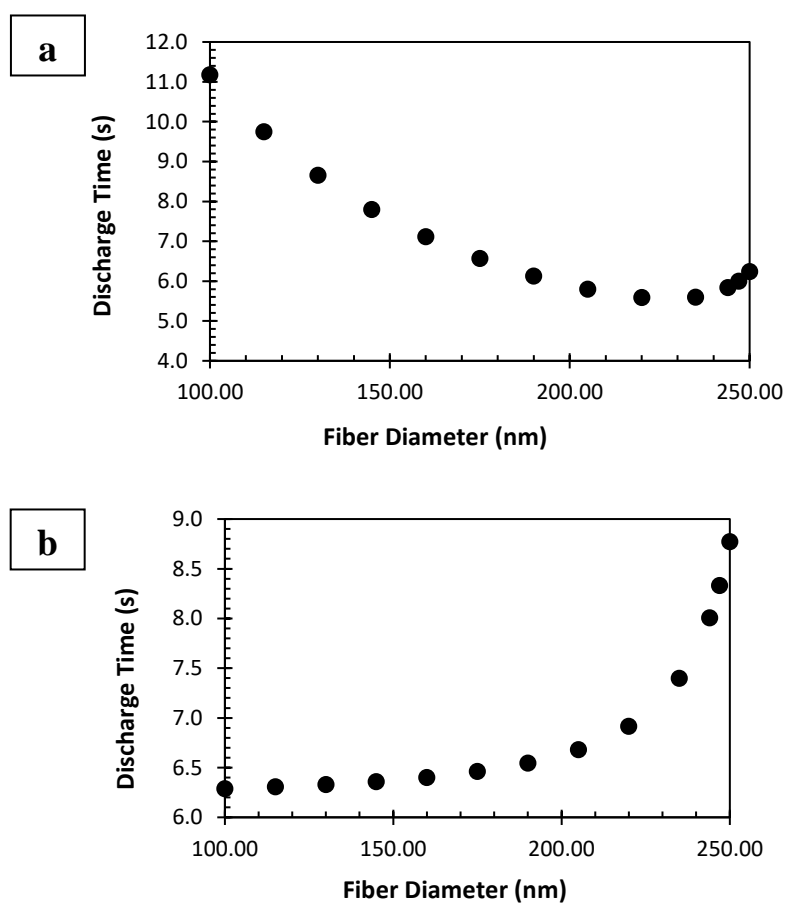


Figure 45: (a) Time to fully discharge for electrodes with varying diameter, discharged from 1 V at a constant current density of 1 A/g; (b) discharge time for electrodes with varying fiber diameter, discharged from 1 V at a constant areal current of $20 \mu\text{A}/\text{cm}^2$ of active surface area.

Discharge time exhibits a $1/D$ relationship with fiber diameter (Figure 45a) up to around 230 nm, after which discharge time again begins to increase. The change from decreasing t_d to increasing t_d results from a shift between the scaling effect-controlled regime below 230 nm to a porosity-controlled regime above 230 nm. Scaling the required current to active surface area, as calculated by s_v , multiplied by the area and thickness, L , of the 15 mm electrodes, removes the $1/D$ dependence in the low-diameter region and reveals the second dominant trend controlling discharge time (Fig. 4b). When areal current is used, the curve is proportional to the inverse of porosity, and as porosity approaches zero, a sharp increase in discharge time is observed. Electrode porosity controls solution conductivity within the electrode pores as described by Eq. (16), which becomes the dominant component of the system time constant, τ , at low porosity (Eq. 15). At high porosity, the $1/\sigma$ matrix conductivity term controls the time constant, but as porosity approaches zero the $1/\kappa_p$ porosity-controlled term inflates the time constant, leading to a longer discharge time. Physically, the effect is caused by decreasing electrolyte conductivity, which results in lower ion transport rates, slower charge transfer, and ultimately a slower electrode response.^{71,147} The lower power density caused by long discharge times is not generally desirable, although the increased surface area associated with minimal porosity works to increase energy density. However, surface area can also be increased in the system by maintaining a small fiber diameter and decreasing the center-to-center fiber spacing. By increasing the number of fibers in a unit cell of the electrode, surface area for energy storage can be maximized while maintaining high porosity to prevent restricting the electrolyte conductivity.

Power and energy densities were calculated according to

$$\text{Energy density} = \frac{I_{cell} \phi_{avg} t_d}{V_{cell}} \quad (29)$$

$$\text{Power density} = \frac{I_{cell} \phi_{avg}}{V_{cell}} \quad (30)$$

where I_{cell} is the total cell current applied, calculated as the product of current density, cell volume, and active volume ($1 - \epsilon$); t_d is discharge time; V_{cell} is the volume of the full cell, including electrolyte, separator, and both electrodes; and ϕ_{avg} is the average cell potential over the entire discharge period as defined by

$$\phi_{avg} = \frac{1}{t_d} \int_0^{t_d} \phi_{cell} dt \quad (31)$$

where ϕ_{cell} is the cell potential measured between the two electrodes. Ragone plots were generated to examine the effect of the unique electrode morphology on power and energy densities (Figure 46).

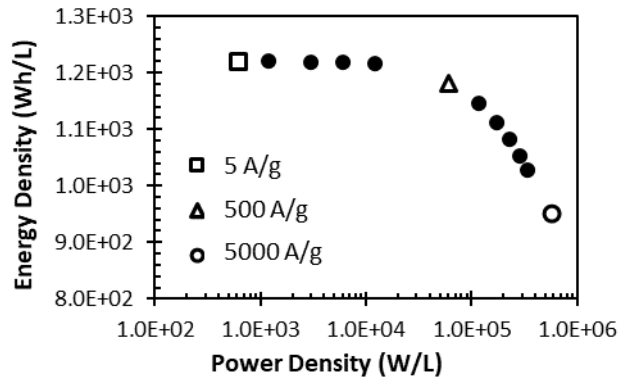


Figure 46: Ragone plot for electrospun electrode with fiber diameter $D = 115$ nm. Current densities used to generate plot range from 5 A/g to 5000 A/g.

Ragone plots constructed for the modeled electrospun electrodes exhibit theoretical power and energy densities equal or superior to nanoparticle-based $\text{RuO}_2 \cdot x\text{H}_2\text{O}$ electrodes previously modeled.^{59,148,149} While theoretical models are not readily available for electrospun

carbon or oxide/carbon composite electrodes, comparisons to real electrospun structures also demonstrates superior performance.^{112,114} In the real system, a high-performance electrospun ZnO-carbon nanofiber electrode possesses an energy density of around 20 Wh/kg at power densities between 400 and 4000 W/kg. For Mn₂O₃ electrospun electrodes with average fiber diameter of 115 nm, the theoretical power density is approximately 270 Wh/kg at an energy density of 400 W/kg. Because carbon-based structures have lower theoretical capacitance than manganese oxides and real systems rarely perform near ideal, the difference between the performance of a real oxide-carbon composite electrode and an idealized, pure oxide electrode is easily explained.

In addition to high performance, the electrodes exhibit remarkably stable energy densities over a wide range of power densities. Between 5 A/g and 500 A/g current densities, nearly no change in energy density is observed, dropping from 1219 Wh/L at 5 A/g to 1217 Wh/L at 500 A/g. Above 500 A/g the change in energy density becomes more apparent, but is still quite minor; at 5000 A/g the theoretical energy density of the electrospun electrodes remains at 952 Wh/L—only a 22 % decrease from maximum energy density with over a 93,000 % increase in power density. By comparison, similar changes in power density for nanoparticle-based RuO₂ structures are predicted to exhibit energy density drops of over two orders of magnitude. By altering current density, power density achieved by the cell can be increased by several orders of magnitude while maintaining energy densities within a single order of magnitude. The potential to improve the range of power densities available to power-dependent applications without a significant negative effect on the energy densities has exciting prospects for implementing the structures in a wider range of applications with flexible power and energy requirements.

To examine model fidelity, predicted discharge curves were compared to actual curves collected with GCD from Mn_2O_3 electrospun electrodes (Figure 47).

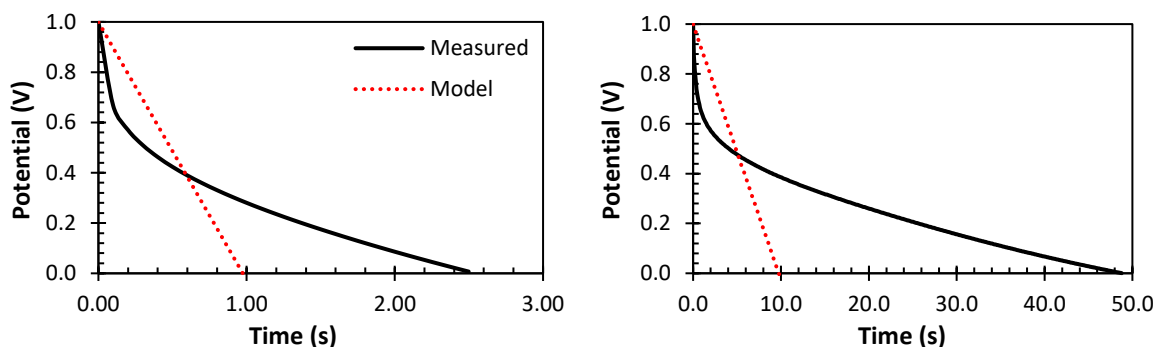


Figure 47: Discharge curve for modeled electrode with fiber diameter $D = 115$ nm vs. measured discharge curve from real electrode with average fiber diameter of 112 nm. Electrodes were discharge from 1 V at a current density of 10 A/g (left) and 1 A/g (right).

As predicted by the model, there is a rapid initial discharge before the faradaic response takes over and slows the discharge. The behavior is less apparent at higher current densities, where the capacitive response has a more dominant effect over the entire discharge owing to kinetic limitations on the faradaic reaction. While the modeled discharge curve shows good correlation with other theoretical models,¹⁴⁸ it departs from actual discharge curves produced by performing GCD on the electrospun electrodes. The sharp initial drop observed in real electrodes is a true capacitive response to the current draw, where the faradaic reactions are too slow to provide the required current; the slope change that occurs after 1-2 s shows the region where pseudocapacitance and faradaic exchange become dominant in the system. The low slope of the discharge curve suggests that the faradaic response in the actual system is more dominant than predicted by the model. True capacitive response therefore accounts for a smaller amount of energy storage than anticipated, further supporting the state of charge results presented in Figure 42, where it was determined that faradaic energy storage was essential to the system.

The discrepancy between the model and experimental results is explained by the characterization techniques used to measure faradaic and capacitive parameters; high-frequency EIS was used to measure DL capacitance of the system, while slow LSV was used to find exchange current density. Using two individual methods at different rates does not account for temporal effects in the system that may affect the balance between faradaic and capacitive response in the electrospun electrodes. The model does not account for the lag in faradaic response, nor the actual dominance of the faradaic response in the electrospun system. It is well-known that measured parameters such as DL capacitance can vary wildly with characterization technique (e.g. CV and GCD can give largely different capacitance values on the same sample), so the wide variety of techniques used to measure characteristic parameters of the electrospun system also worked to reduce model fidelity. However, further characterization of the Mn_2O_3 systems and electrodes composed of other oxides will serve to improve model accuracy by providing a more accurate estimate of system parameters.

3.5.4. Modeling System Parameters

The effect of system parameters on discharge curves was examined to locate essential areas of optimization for the freestanding electrospun electrodes (Figure 48 through Figure 52).

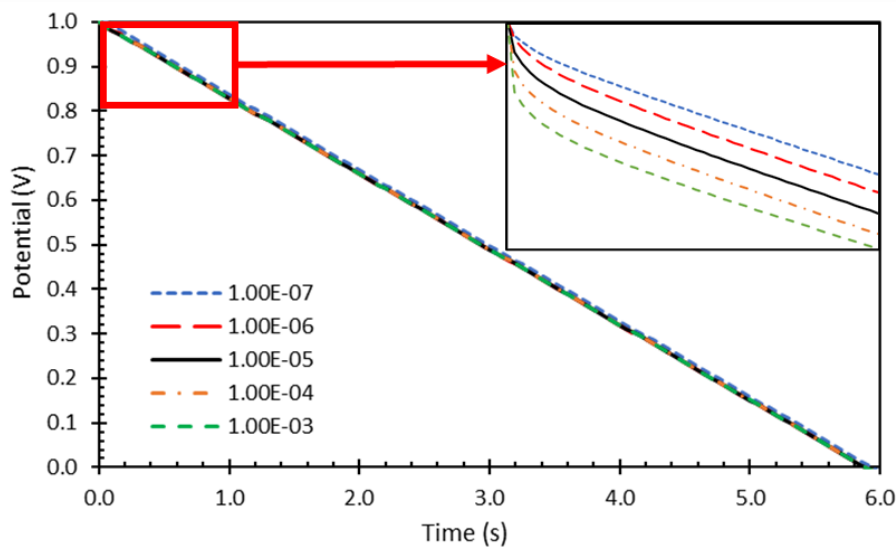


Figure 48: Effect of exchange current density, i_0 (A/cm^2), on modelled discharge behavior. Plots generated at $D = 120 \text{ nm}$ and 1 A/g current density.

Exchange current density has only a minor effect on the high-porosity electrodes, with changes over four orders of magnitude having an almost negligible effect on the discharge curves of electrodes with otherwise identical structures and parameters. There is an effect in the initial moments of discharge, where the region of slope change shifts according to i_0 . At smaller exchange current densities, where electrons are produced more slowly, the region of slope change occurs earlier as the balance between electrons produced and those consumed reaches steady-state more rapidly. At higher exchange current densities, electrons are provided more rapidly, so it takes slightly longer to consume excess electrons and reach steady state in the discharge curve. The result of the shift in slope change region is a very slight change in discharge time, with smaller exchange current densities resulting in slightly longer discharge times as the system is kinetically limited by the rate at which electrons are provided by the faradaic reaction. It is known that at different discharge currents, the point of slope change in the discharge curve shifts, with a maximum capacitance occurring at a value of i_0 where the rate of electron

consumption from discharge is similar to that of electron production from the faradaic reaction.¹⁴⁹ As i_0 increases, discharge time can be expected to increase up to the i_0 that corresponds to maximum capacitance, then decrease thereafter. The value of i_0 for which a maximum occurs at 1 A/g is below the range examined, but its effect on discharge performance is minimal.

The effect of matrix conductivity on electrode performance was next investigated. Conductivities between 0.01 S/cm and 0.1 mS/cm were used to produce modeled discharges (Figure 49).

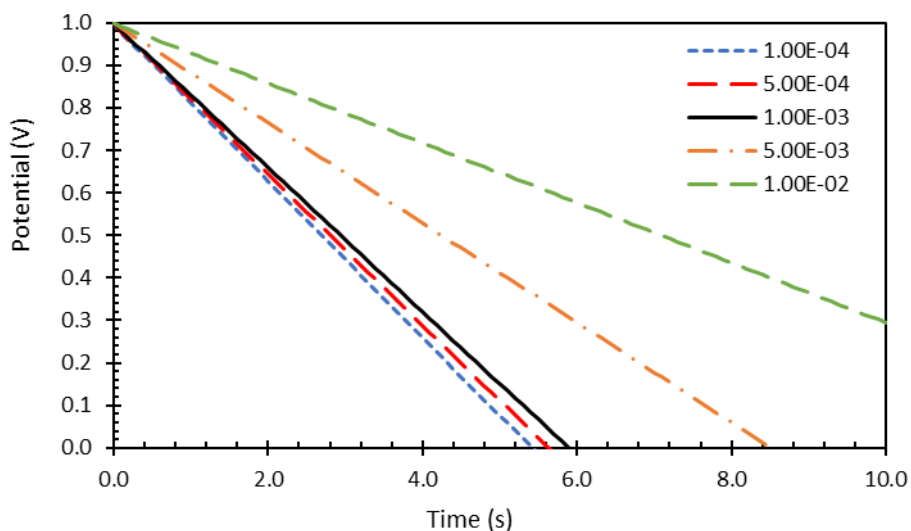


Figure 49: Effect of matrix conductivity, σ (S/cm), on modelled discharge curve. Plots generated at $D = 120$ nm and 1 A/g current density.

Discharge time increases with increasing matrix conductivity as higher conductivity results in a smaller initial voltage drop. In keeping with Ohm's law, to produce a constant current, smaller voltage drops are necessary with lower-resistance electrodes. Energy density is directly related to total capacitance of the electrode, which can be calculated from linear discharge curves by

$$C = \frac{I_{cell} t_d}{\Delta V} \quad (32)$$

where all the symbols have their previous definitions. Longer discharge times at constant currents therefore directly correlate to increased energy density. At low matrix conductivity ($<10^{-3}$ S/cm), discharge times change much more slowly, suggesting that at 1 A/g, there is some threshold conductivity below which other aspects of the system prevent further decrease in discharge times. The enormous effect of improving electrode conductivity on total energy storage capacity is consistent with literature and exhibits the importance of improving electrode conductivity to increasing the energy densities of supercapacitors.¹⁵⁰

Because the experimental setup used a low-conductivity electrolyte to avoid handling and storing highly corrosive solutions, the effect of increasing electrolyte conductivity up to 5 S/cm was examined (Figure 50).

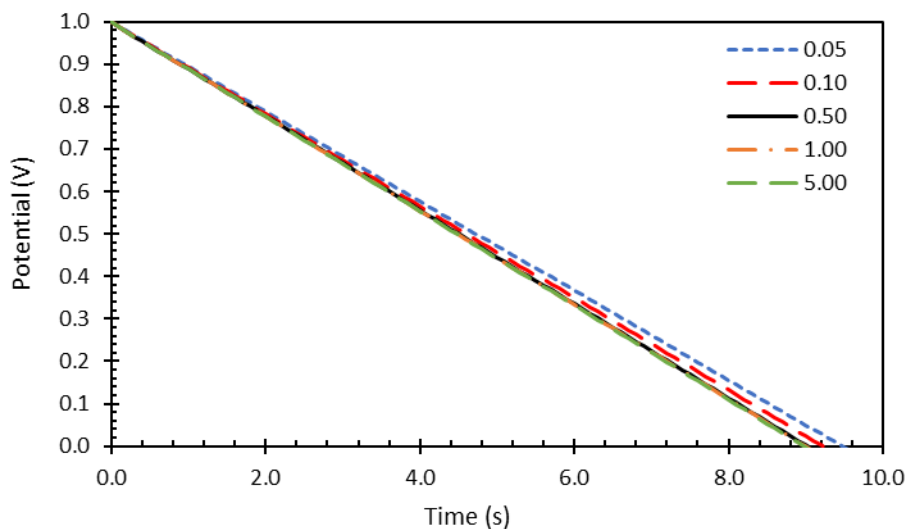


Figure 50: Effect of electrolyte conductivity, κ_0 (S/cm), on discharge behavior. Model generated with $D = 120$ nm at 1 A/g current density.

Bulk electrolyte conductivity has little effect on performance of the electrospun electrodes. Over a range of two orders of magnitude, which fully encompasses and extends beyond the conductivity values for typical aqueous electrolytes at both low and high concentrations, very little change in the discharge rate is observed at otherwise constant conditions. The result is interesting because Lin's examination of an RuO₂ nanoparticle-based electrode concluded that electrolyte resistance was the limiting resistance of the system owing to their assumption that the RuO₂ matrix had a conductivity of 10⁵ S/cm, a value higher than many metals and one that was admitted to be potentially several orders of magnitude higher than actual conductivity values.⁵⁹ In their model, the actual conductivity of the electrode matrix was assumed to be nearly irrelevant because of the limiting influence of the electrolyte, but in a system with a low matrix conductivity, such as manganese oxide, the effect of electrolyte conductivity becomes minor. With high matrix resistance, the importance of electrolyte conductivity is minimized, allowing the use of safe, low-concentration, and less corrosive electrolytes for experimental purposes.

Areal capacitance of a material is a function of its surface configuration, including lattice spacing and atomic arrangement. The effect of DL capacitance per unit area on energy storage was examined over a range of values that encompass the capacitances of common electrode materials^{30,151} and is presented in Figure 51.

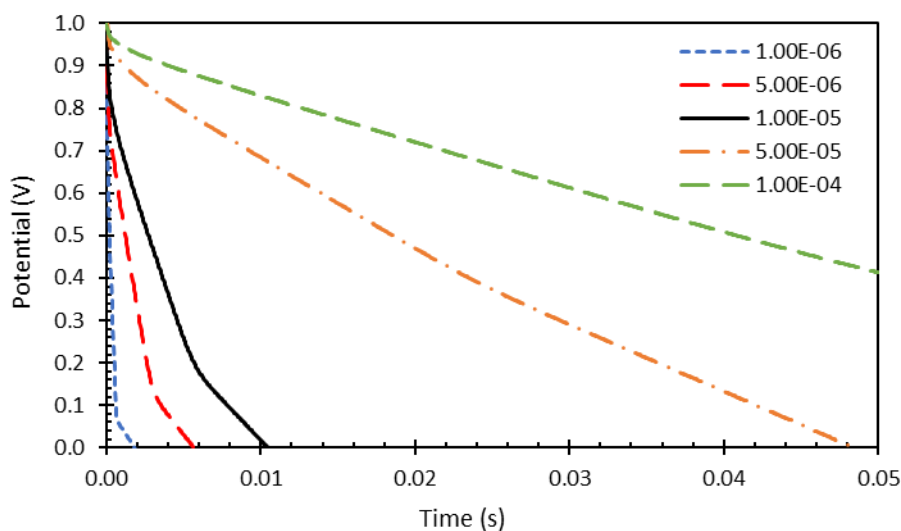


Figure 51: Effect of DL capacitance per unit surface area, C_d (F/cm^2), on discharge curve. Model generated with $D = 120$ nm at 1 A/g current density.

Because areal capacitance of a material directly influences energy storage capacity in much the same way as surface area, it is unsurprising that DL capacitance of a material has an enormous effect on the specific energy of a device. However, it is a parameter associated with material selection for the electrode and is tied to other intrinsic properties such as matrix conductivity. However, for manganese oxides, fabrication conditions influence the phase of the material, so for a given material stoichiometry (e.g. MnO_2), atomic structure and crystallinity can change the specific capacitance of the oxide by an order of magnitude or more.¹²⁸ Additionally, low areal capacitance can be countered by increasing mass loading and active surface area of the electrode.

While the effect of porosity on discharge behavior is examined via fiber diameter in Figure 45b, a separate examination at constant fiber diameter was also performed (Figure 52).

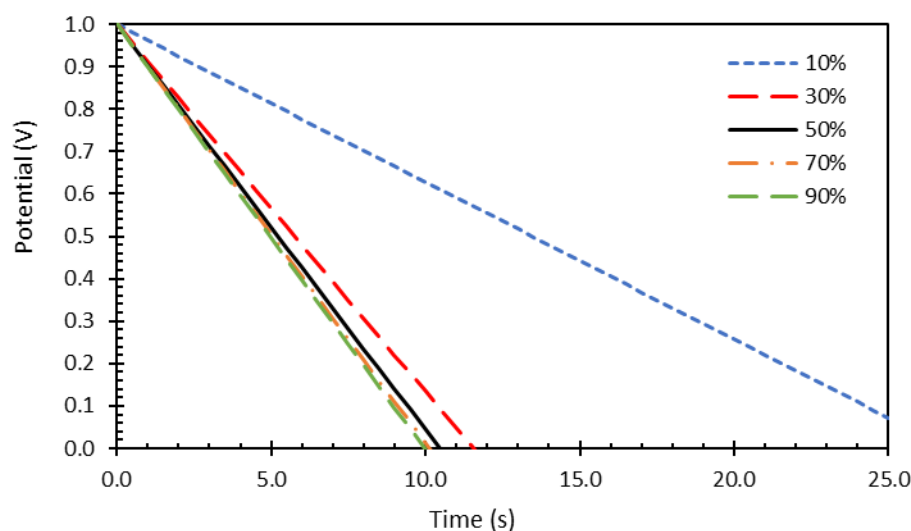


Figure 52: Effect of porosity (%) on discharge behavior. Model generated with $D = 120$ nm at 1 A/g current density; changes in porosity represent changes in total mass present as well as a reduction in average pore size.

Above ~50 %, porosity changes have little effect on the electrode performance. As porosity decreases, a rapid increase in t_d and, correspondingly, energy density is observed. The increased discharge time is partially due to restriction of electrolyte conductivity as discussed with regards to Figure 45; however, the change in energy density is primarily the result of increased active mass and surface area. When decreasing porosity without modifying fiber diameter, the effect is a simulation wherein the packing density of the fibers is increased to consume void space in the electrode. In a low-porosity electrode, the active mass and energy density are greater. Unlike the changing fiber diameters observed in Figure 45, the simulation in Figure 52 retains the high specific surface area associated with low-diameter fibers, without increased dead space in the fiber interiors. Thus, increasing the packing density of the electrospun fibers is an important route towards optimization of freestanding electrospun electrodes.

3.5.5. Modeling Energy Storage Oxides

A significant application for modeling electrospun electrodes is predicting performance of various energy storage oxides without the investment necessary to successfully produce electrospun oxide structures from various materials systems, which can be time-consuming and expensive. Because of the unique structure and high porosity of electrospun electrodes, the interplay between the capacitance and electrical conductivity of materials cannot be directly compared for the purposes of material selection. Rather, by gathering literature values for several commonly measured material properties, the model can be used for qualitative comparison of the suitability of various oxides (Table IV).

Table IV: Material parameters used to predict performance of energy storage oxides in freestanding electrospun electrodes.

| Oxide | Capacitance (mF/cm ²) | Crystal Lattice Length (Å) | Electrical Conductivity (S/cm) |
|--------------------------------|-----------------------------------|----------------------------|--------------------------------|
| α -MnO ₂ | 1.39 ¹²⁸ | 2.40 ¹²⁸ | 1.00e-5 ⁵⁵ |
| Fe ₂ O ₃ | 18.4 ¹⁵² | 6.37 ¹⁵² | 1.00e-12 ^{152,153} |
| Co ₃ O ₄ | 1.05 ¹⁵⁴ | 2.00 ¹⁵⁴ | 3.35e-4 ¹⁵⁵ |
| V ₂ O ₅ | 2.63 ¹⁵⁶ | 2.76 ¹⁵⁶ | 1.00e-4 ¹⁵⁷ |
| WO ₃ | 2.14 ¹⁵⁸ | 3.82 ¹⁵⁸ | 3.16e-7 ¹⁵⁹ |

Five commonly investigated energy storage oxides were added to the model for comparative purposes. Because real systems rarely produce values near the theoretical maximums, measured capacitance, conductivity, and lattice parameters were selected over theoretical values. The electrical conductivity of the electrospun electrode matrices is lower than measured values for bulk or continuous materials due to the high porosity and many disruptions in the charge transfer pathways, but it is assumed that the structure will affect the conductivity of all materials similarly and the values remain useful for qualitative comparison. For all the oxides,

literature examining their performance as nanostructures was used as the behavior was assumed to be more representative of their theoretical behavior in a nanostructured web configuration.

Several assumptions were made to simplify the comparison. Identical electrode geometries were used for all simulations, and identical faradaic kinetics were assumed for all materials.⁵⁹ Because the literature capacitance values did not distinguish between DL capacitance and pseudocapacitance in their reported measurements, the faradaic component of the model was rendered negligible by assuming no exchange current and attributing all the discharge to DL capacitance. The removal of the faradaic component was necessary to avoid overestimating total capacitance of the materials by adding an additional pseudocapacitive component to the measured total capacitance. Fortunately, by assuming the faradaic component of energy storage to be negligible, the inaccuracies introduced by other assumptions such as transfer coefficients and faradaic equilibrium potentials become less significant to the model performance. The assumed system parameters which are identical for all the modeled systems are presented in Appendix A.

It is notable that the voltage window of 0 – 1 V used in the modeled electrodes is not universally compatible and that several of these energy storage oxides, especially V_2O_5 , exhibit high dissolution rates and narrow electrochemical stability windows in aqueous electrolyte.^{156,160} For real device construction and testing, the 0 – 1 V window and 1.0 M Na_2SO_4 electrolyte used in the model would not be suitable for most oxides and modifications to the testing conditions or implementation of an asymmetrical system would be necessary to achieve optimal performance. However, the parameters presented in Table IV were collected under conditions appropriate to the materials, so the qualitative predictions of discharge behavior and energy density provided by

the model (Figure 53) can be assumed to be representative of how the materials would compare when tested in their respective suitable systems.

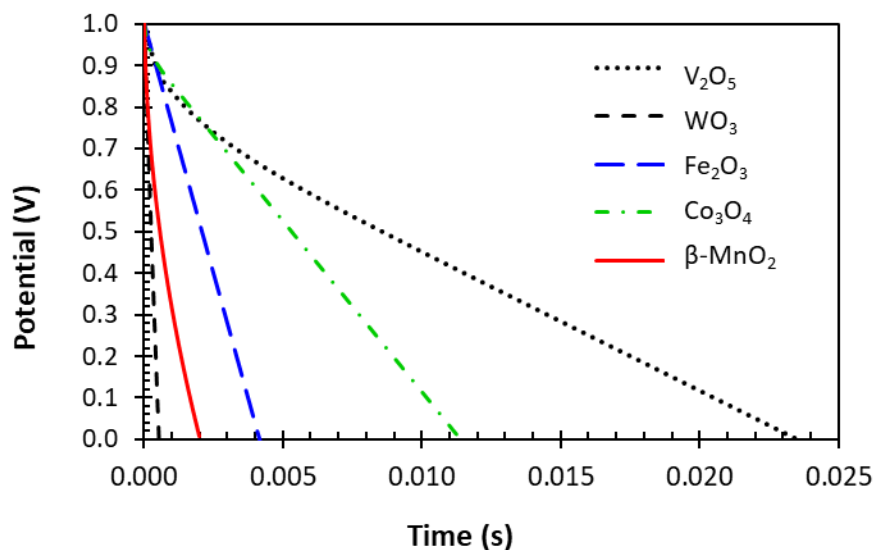


Figure 53: Predicted discharge curves for freestanding electrospun electrodes fabricated from different energy storage oxides. Discharge curves modeled with 150 nm fibers, 750 nm electrode thickness, and porosity of 0.5 assumed. Discharge is modeled at 1 mA/cm² current density.

The complex relationship between the material parameters described in Table IV can be observed in the modeled discharge curves in Figure 53. While V₂O₅ is predictably superior due to its high capacitance and electrical conductivity, Co₃O₄ performs unexpectedly well despite having the lowest capacitance of the examined materials, owing to its high electrical conductivity. WO₃, on the other hand, has a relatively high areal capacitance, but its poor electrical conductivity makes it one of the lowest-performing oxides examined. For a low-cost electrode with relatively good energy density, Fe₂O₃ may be a promising material. Direct comparison of the discharge curves produced for geometrically identical electrodes with varying compositions shows that neither capacitance nor electrical conductivity can be independently

optimized for a high-performance electrospun electrode, and that a balance of the two properties is required to maximize the energy and power densities of the structures.

The simplifying assumptions used for predicting the performance of various materials based on literature values for material parameters render the predicted energy densities useful only for qualitative purposes, but it is highly useful for materials selection and finding an electrode material for which capacitance and conductivity are properly balanced to maximize the potential energy density of electrospun electrodes. By using the model for such predictive purposes, the time and financial investments necessary for constructing high-performance electrospun electrodes will be decreased.

4. Conclusions

4.1. Electrode Fabrication Parameters

Freestanding web electrodes were fabricated via a facile electrospinning and direct calcination procedure, and the effects of several fabrication parameters on electrochemical storage performance were examined. Electrospinning solution composition, deposition time, and calcination duration were varied between low and high conditions, and a statistical model was fit to the effects of each parameter on areal capacitance. Increasing polymer concentration was found to result in improved capacitance due to the high surface area of the fibrous morphologies. Precursor concentration has a negative correlation with capacitance due to decreasing structure porosity with increasing $\text{Mn}(\text{ac})_2$ content. The high-concentration samples exhibit an average decrease in capacitance of 27 % as compared to those prepared with low precursor concentrations. Increasing deposition time and calcination time both have consistent positive effects on capacitance (34 % and 62 % improvements between the low and high values) from increased active mass and improved charge transfer, respectively. However, past 240 minutes,

increasing calcination time ceases to improve energy storage performance as fiber densification drastically slows. Within the range of conditions studied, performance was maximized at 20 % PVP, 8 % $\text{Mn}(\text{ac})_2$, 30 min deposition, and 240 min calcination, which resulted in a highly porous fiber-based electrode with greater active mass and improved electrical qualities.

Modifications to calcination environment pressure and composition were tested for their effects on capacitive performance. By decreasing calcination pressure in air to sub-atmospheric pressures, mixed-phase Mn_2O_3 - Mn_3O_4 fibers were prepared and showed enhanced specific capacitance as compared to single-phase Mn_2O_3 or Mn_3O_4 fibers. Cross-sectional fiber morphology changed dramatically at sub-atmospheric pressures, contributing to increased surface area and muddling the trends in specific capacitance between Mn_2O_3 and Mn_3O_4 fibers. While controlled calcination pressure can be used to prepare mixed-phase MnO_x fibers for supercapacitor electrodes, the simultaneous effect on fiber morphology prevents single-parameter tunability for high-performance supercapacitor electrodes. Calcining the fibers in a pure oxygen environment produces a surface oxidation to MnO_2 , a higher-performing phase of manganese oxide. However, the surface oxidation does not have a significant effect on electrochemical performance, indicating that the freestanding electrospun structures tested are limited by their low bulk conductivity rather than the capacitive properties of the surface oxide.

The effects of hot pressing and vapor melting steps prior to calcination were examined, and while hot pressing had a negative effect on performance due to fiber loss, vapor melting in a humidity-controlled chamber resulted in performance improvements of up to 57 % over electrodes that were calcined without additional processing. Vapor melting treatments additionally improved the wettability of electrode surfaces, which indicates better electrolyte-

electrode contact and accounts for some of the improved performance. Structural changes, with improved fiber mat stability and through-layer connectivity, also improved performance.

The production of freestanding electrospun electrodes with ultrahigh specific surface areas via a facile and direct route has the potential to improve the performance of low-cost electrodes with reduced weight. It was found that fabrication methods including low oxide precursor and high polymer concentrations, lengthened electrospinning times, at least 4 h calcination, and a pre-calcination vapor melting step improve performance of electrospun electrodes, with potential further improvement from using low pressure to induce a mixed-phase structure.

Further increasing mass of fibers in the electrode via greater electrospun mat thickness will further increase the energy storage capacity by increasing active mass and the number of available charge transfer pathways. Optimizing post-processing treatments to improve charge transfer through the electrospun structures and to the charge collecting substrate will provide a route for improved performance. Further investigation into the effects of electrospinning and calcination conditions is necessary to optimize the performance of manganese oxide free-standing electrodes. While current capacitance values are lower than high-performance Mn_2O_3 electrodes reported in literature, further work into improving the electrical properties of the calcined oxide structures via controlled processing may improve performance to levels comparable to current nanostructure-based electrodes, providing a route to low-cost, high-performance supercapacitors.

4.2. Electrospun Electrode Modeling

A mathematical model with experimentally-derived parameters was produced to describe the performance of Mn_2O_3 -based freestanding electrospun electrodes. A theoretical model based on

capacitive and faradaic energy storage processes was used to examine the effects of fiber diameter and current density on discharge time, energy density, and power density. The unique effects of freestanding web electrode geometry on performance were evident by way of their discharge behavior: with constant current density scaled to electrode mass, discharge time decreases with increasing fiber diameter up to 230 nm, then increases rapidly as porosity approaches zero. It is apparent that the optimized structure will combine small fiber diameters with a smaller interfiber spacing to maximize active surface area while maintaining high porosity. The electrode structures exhibit remarkably high theoretical energy density retention with increasing power density, which is a major problem to be solved with supercapacitors. Comparison to real discharge curves shows that the model underestimates the capacitive response during initial discharge and the importance of the faradaic reactions over the remainder of the discharge period, rendering it more useful for qualitative comparison than quantitative predictions. A primary difficulty in producing an experimentally-based theoretical model is the necessity of mixing characterization techniques, but further characterization will improve model fidelity to result in greater accuracy and flexibility.

Individual manipulation of the model parameters reveals the relative importance of different aspects of electrode optimization. Faradaic exchange current density and electrolyte conductivity have only minor effects on the manganese oxide electrodes, with lower exchange current densities and electrolyte conductivities slightly improving performance. Matrix conductivity was modeled over several orders of magnitude and provides a significant performance improvement only at high conductivities. Electrode porosity likewise only greatly improves performance when it is very low; otherwise, its effect is minor. Areal capacitance of the active surface has a large and direct effect on energy storage capacity over the entire range examined, with higher

capacitances directly resulting in increased energy densities. A simplified version of the model was also applied to a variety of energy storage oxides to predict suitability for use as freestanding electrospun electrodes. By inserting material capacitance, electrical conductivity, and lattice spacing, the model gives a qualitative prediction of the relative performances of each oxide. It demonstrates that neither conductivity nor capacitance can be individually optimized, and a balance of the two is necessary to achieve high energy densities in electrospun web electrodes.

4.3. Future work

The work presented herein is intended to provide a starting point for the investigation and optimization of oxide-based energy storage devices produced via electrospinning and post-processing.

4.3.1. Improving Electrode Performance

The freestanding electrospun electrodes presented herein exhibit energy storage performance far below their theoretical maximums and therefore require significant improvements prior to implementation. Several structural modifications are suggested for future work:

- Using a Ni or Cu foil for the current collecting substrate;
- Laying down an oxide film prior to electrospinning and calcination;
- Using slower ramp rates during calcination to decrease sloughing from thermal stress;
- Using low-pressure calcination to produce freestanding web electrodes with mixed phase;
- Combining post-processing with improved fabrication conditions; and
- Increase mass loading and decrease interfiber spacing of electrospun fibers.

The suggested modifications are based on experimental results and literature observations and provide a starting point for improving the freestanding electrospun structures.

4.3.2. Improving Model Fidelity

While the mixed mathematical and experimental model presented herein is an initial step towards theoretical optimization of freestanding electrospun electrodes, inaccurate estimations of system values have led to poor overall predictions of discharge time for real systems (Figure 47 and the MnO₂ equivalent). Increased accuracy in parameter measurement and estimation will therefore be critical to improving the predictive power of the model. A nonlinear equation for the relationship between state of charge and potential should be developed and implemented in the model, which may improve the shape of the modeled discharge curve to be more realistic. The real electrical resistivity of the electrode matrix should also be measured, as it is one of the only parameters assumed from literature values rather than measured directly and is shown in Figure 49 to have a large effect on electrode discharge.

Additionally, the model assumes perfectly symmetrical behavior at the anode and cathode and neglects any side reactions or self-discharge. Tafel plots of the electrodes, as well as the asymmetrical transfer coefficients show that the Mn₂O₃ electrodes have different affinities for positive and negative polarization. Therefore, incorporation of asymmetrical models^{64,161,162} should be considered to produce a more realistic simulation. Leakage should also be added to the simulations for maximum model fidelity, especially at low current densities where slow charging and discharge rates allow for self-discharge to have a greater impact on device performance.

Because the model is based on mathematical equations, theoretical optimization of the electrodes based on geometric parameters would be highly useful in reducing the time necessary for experimental optimization. Simultaneous optimization of fiber diameter, porosity, and electrode thickness will allow for predicting structures with the most ideal characteristics for

energy storage. Calculating theoretical energy and power densities for the structures will also allow for easier comparison to devices that exist commercially and in literature.

4.3.3. Solid State Electrolytes

Freestanding electrospun electrodes experience significant capacity fading due to Mn^{3+} dissolution into aqueous electrolyte and structural deformation from the heating associated with charging. A route towards stabilizing the structures exists in solid electrolytes, where aqueous solubility becomes irrelevant and expansion of the electrode and electrolyte due to heating would result in fiber compression, which may decrease the degree of capacity fading observed in the electrodes. Ensuring full permeation of the solid electrolyte into the electrospun web electrode would be paramount to stabilizing the structures and would be one of the primary difficulties associated with this work.

4.3.4. Fiber Alignment

This work was produced with chaotically deposited fibers, which may not be the most effective geometry. Investigation of uniaxially and biaxially aligned fibers should be performed in order to determine the effect of fiber alignment on performance. Fiber alignment will likely improve the conductivity of the electrode matrix, as regular points of fiber connectivity will result in shorter charge transfer pathways from the charge collector to the electrode surface. As a route towards improving the matrix conductivity of the electrospun electrodes, fiber alignment may be promising; however, the effect of alignment on wettability of the calcined electrodes should also be carefully investigated. Uniaxially aligned fibers will have a greatly improved packing density, but during calcination may lose their permeable web structure, becoming a solid mass with inaccessible surface area locked beneath an impermeable top layer. However, the improved

conductivity may improve performance sufficiently to overcome any potentially deleterious effects.

5. References Cited

1. Pachauri, R. K., Mayer, L. & Intergovernmental Panel on Climate Change. *Climate change 2014 : synthesis report*.
2. IPCC. *Climate Change 2007: The Physical Science Basis. Contribution of Working Group I to the Fourth Assessment Report of the Intergovernmental Panel on Climate Change*. (Cambridge University Press, 2007).
3. Administration, U. E. I. Annual Energy Outlook 2021. (2021). Available at: <https://www.eia.gov/outlooks/aeo/>.
4. Wang, G., Ciobotaru, M. & Agelidis, V. G. Power smoothing of large solar PV plant using hybrid energy storage. *IEEE Trans. Sustain. Energy* **5**, 834–842 (2014).
5. Murray, D. B., Hayes, J. G., O’Sullivan, D. L. & Egan, M. G. Supercapacitor testing for power smoothing in a variable speed offshore wave energy converter. *IEEE J. Ocean. Eng.* **37**, 301–308 (2012).
6. Howlader, A. M., Urasaki, N., Yona, A., Senjyu, T. & Saber, A. Y. A review of output power smoothing methods for wind energy conversion systems. *Renewable and Sustainable Energy Reviews* **26**, 135–146 (2013).
7. Pegueroles-Queralt, J., Bianchi, F. D. & Gomis-Bellmunt, O. A power smoothing system based on supercapacitors for renewable distributed generation. *IEEE Trans. Ind. Electron.* **62**, 343–350 (2015).
8. Jayasinghe, S. D. G. & Vilathgamuwa, D. M. Flying supercapacitors as power smoothing elements in wind generation. *IEEE Trans. Ind. Electron.* **60**, 2909–2918 (2013).
9. Vazquez, S., Lukic, S. M., Galvan, E., Franquelo, L. G. & Carrasco, J. M. Energy storage systems for transport and grid applications. *IEEE Trans. Ind. Electron.* **57**, 3881–3895 (2010).
10. Zhang, Z. *et al.* A high-efficiency energy regenerative shock absorber using supercapacitors for renewable energy applications in range extended electric vehicle. *Appl. Energy* **178**, 177–188 (2016).
11. Mastragostino, M. & Soavi, F. Strategies for high-performance supercapacitors for HEV. *J. Power Sources* **174**, 89–93 (2007).
12. Conway, B. E. *Electrochemical Supercapacitors: Scientific Fundamentals and*

- Technological Applications*. (Springer Science and Business Media LLC, 1999).
13. Eftekhari, A. The mechanism of ultrafast supercapacitors. *Journal of Materials Chemistry A* **6**, 2866–2876 (2018).
 14. Kim, B. K., Sy, S., Yu, A. & Zhang, J. Electrochemical Supercapacitors for Energy Storage and Conversion. in *Handbook of Clean Energy Systems* 1–25 (John Wiley & Sons, Ltd, 2015). doi:10.1002/9781118991978.hces112
 15. González, A., Goikolea, E., Barrena, J. A. & Mysyk, R. Review on supercapacitors: Technologies and materials. *Renewable and Sustainable Energy Reviews* **58**, 1189–1206 (2016).
 16. Kötz, R. & Carlen, M. Principles and applications of electrochemical capacitors. *Electrochim. Acta* **45**, 2483–2498 (2000).
 17. Chuang, C. M., Huang, C. W., Teng, H. & Ting, J. M. Effects of carbon nanotube grafting on the performance of electric double layer capacitors. *Energy and Fuels* **24**, 6476–6482 (2010).
 18. Hu, Y., Zhu, H., Wang, J. & Chen, Z. Synthesis of layered birnessite-type manganese oxide thin films on plastic substrates by chemical bath deposition for flexible transparent supercapacitors. *J. Alloys Compd.* **509**, 10234–10240 (2011).
 19. Daggetti, A., Lodi, G. & Trasatti, S. Interfacial properties of oxides used as anodes in the electrochemical technology. *Mater. Chem. Phys.* **8**, 1–90 (1983).
 20. Lee, H. Y. & Goodenough, J. B. Supercapacitor Behavior with KCl Electrolyte. *J. Solid State Chem.* **144**, 220–223 (1999).
 21. Toupin, M., Brousse, T. & Bélanger, D. Charge storage mechanism of MnO₂ electrode used in aqueous electrochemical capacitor. *Chem. Mater.* **16**, 3184–3190 (2004).
 22. Wang, S.-Y., Ho, K.-C., Kuo, S.-L. & Wu, N.-L. Investigation on Capacitance Mechanisms of Fe₃O₄ Electrochemical Capacitors. *J. Electrochem. Soc.* **153**, 75–80 (2005).
 23. Hu, C. C., Huang, C. M. & Chang, K. H. Anodic deposition of porous vanadium oxide network with high power characteristics for pseudocapacitors. *J. Power Sources* **185**, 1594–1597 (2008).
 24. Xia, X. H., Tu, J. P., Wang, X. L., Gu, C. D. & Zhao, X. B. Mesoporous Co₃O₄

- monolayer hollow-sphere array as electrochemical pseudocapacitor material. *Chem. Commun.* **47**, 5786–5788 (2011).
25. Gamby, J., Taberna, P. L., Simon, P., Fauvarque, J. F. & Chesneau, M. Studies and characterisations of various activated carbons used for carbon/carbon supercapacitors. *J. Power Sources* **101**, 109–116 (2001).
 26. Gogotsi, Y. *et al.* Nanoporous carbide-derived carbon with tunable pore size. *Nature Materials* **2**, 591–594 (2003).
 27. Chmiola, J., Yushin, G., Dash, R. & Gogotsi, Y. Effect of pore size and surface area of carbide derived carbons on specific capacitance. *J. Power Sources* **158**, 765–772 (2006).
 28. Pandolfo, A. G. & Hollenkamp, A. F. Carbon properties and their role in supercapacitors. *Journal of Power Sources* **157**, 11–27 (2006).
 29. Pumera, M. Graphene-based nanomaterials and their electrochemistry. *Chem. Soc. Rev.* **39**, 4146–4157 (2010).
 30. Wang, G., Zhang, L. & Zhang, J. A review of electrode materials for electrochemical supercapacitors. *Chem. Soc. Rev.* **41**, 797–828 (2012).
 31. Yang, K. S., Joo, Y. W., Kim, T., Hyu Kim, J. & Lee, W. J. Performances of Electrochemical Hybrid Supercapacitor of RuO₂/Activated Carbon Nanofibers from Electrospinning. in *WSEAS/IASME Int. Conf. on Electrosience & Technolog for Naval Engineering* 6–10 (2006).
 32. Yoon, Y. S., Cho, W. I., Lim, J. H. & Choi, D. J. Solid-state thin-film supercapacitor with ruthenium oxide and solid electrolyte thin films. *J. Power Sources* **101**, 126–129 (2001).
 33. Prasad, K. R. & Miura, N. Electrochemically deposited nanowhiskers of nickel oxide as a high-power pseudocapacitive electrode. *Appl. Phys. Lett.* **85**, 4199–4201 (2004).
 34. Patil, U. M., Salunkhe, R. R., Gurav, K. V. & Lokhande, C. D. Chemically deposited nanocrystalline NiO thin films for supercapacitor application. *Appl. Surf. Sci.* **255**, 2603–2607 (2008).
 35. Srinivasan, V. & Weidner, J. W. Capacitance studies of cobalt oxide films formed via electrochemical precipitation. *J. Power Sources* **108**, 15–20 (2002).
 36. Kandalkar, S. G., Gunjekar, J. L. & Lokhande, C. D. Preparation of cobalt oxide thin films and its use in supercapacitor application. *Appl. Surf. Sci.* **254**, 5540–5544 (2008).

37. Sanchez-Gonzalez, J., Stoeckli, F. & Centeno, T. A. The role of the electric conductivity of carbons in the electrochemical capacitor performance. *J. Electroanal. Chem.* **657**, 176–180 (2011).
38. Wu, H.-C., Chang, X., Liu, L., Zhao, F. & Zhao, Y. Chemistry of carbon nanotubes in biomedical applications. *J. Mater. Chem.* **20**, 1036–1052 (2010).
39. Xuan Wang, Zhi, L. & Müllen, K. Transparent, Conductive Graphene Electrodes for Dye-Sensitized Solar Cells. *Nano Lett.* **8**, 323–327 (2007).
40. Hu, C. C. & Chen, W. C. Effects of substrates on the capacitive performance of RuO_x·nH₂O and activated carbon-RuO_x electrodes for supercapacitors. *Electrochim. Acta* **49**, 3469–3477 (2004).
41. Lokhande, C. D., Dubal, D. P. & Joo, O.-S. Metal oxide thin film based supercapacitors. *Curr. Appl. Phys.* **11**, 255–270 (2011).
42. Park, C. *et al.* Electronic, Optical and Electrical Properties of Nickel Oxide Thin Films Grown by RF Magnetron Sputtering. *Appl. Sci. Conver. Technol.* **24**, 72–76 (2015).
43. Hassan, A. J. Study of Optical and Electrical Properties of Nickel Oxide (NiO) Thin Films Depo-sited by Using a Spray Pyrolysis Technique. *J. Mod. Phys.* **5**, 2184–2191 (2014).
44. Makhoulouf, S. A., Bakr, Z. H., Aly, K. I. & Moustafa, M. S. Structural, electrical and optical properties of Co₃O₄ nanoparticles. *Superlattices Microstruct.* **64**, 107–117 (2013).
45. Sukeji, K., Tosio, T. & Koji, K. Electrical Conductivity of Vanadium Oxides. *J. Phys. Soc. Japan* **18**, 1839–1840 (1963).
46. Lan, B. *et al.* The art of balance: Engineering of structure defects and electrical conductivity of α -MnO₂ for oxygen reduction reaction. *Electrochim. Acta* **283**, 459–466 (2018).
47. Simon, P. & Gogotsi, Y. Materials for electrochemical capacitors. *Nat. Mater.* **7**, 845–854 (2008).
48. Fang, H., Yue, B., Hirao, N., Liu, Z. & Chen, B. Significant improvement in Mn₂O₃ transition metal oxide electrical conductivity via high pressure. *Nat. Publ. Gr.* **7**, 44078 (2017).
49. Bhagwan, J., Sahoo, A., Yadav, K. L. & Sharma, Y. Porous, One dimensional and High Aspect Ratio Mn₃O₄ Nanofibers: Fabrication and Optimization for Enhanced

- Supercapacitive Properties. *Electrochim. Acta* **174**, 992–1001 (2015).
50. Zhu, J. *et al.* The application of graphene in lithium ion battery electrode materials. *SpringerPlus* 2014 31 **3**, 1–8 (2014).
 51. Hu, Y., Wu, Y. & Wang, J. Manganese-Oxide-Based Electrode Materials for Energy Storage Applications: How Close Are We to the Theoretical Capacitance? *Adv. Mater.* **30**, 1802569 (2018).
 52. Radhamani, A. V., Krishna Surendra, M. & Ramachandra Rao, M. S. Tailoring the supercapacitance of Mn₂O₃ nanofibers by nanocompositing with spinel-ZnMn₂O₄. *Mater. Des.* **139**, 162–171 (2018).
 53. Logothetis, E. M. & Park, K. The electrical conductivity of Mn₃O₄. *Solid State Commun.* **16**, 909–912 (1975).
 54. Hall, P. J. *et al.* Energy storage in electrochemical capacitors: Designing functional materials to improve performance. *Energy Environ. Sci.* **3**, 1238–1251 (2010).
 55. Hong, F., Yue, B., Hirao, N., Liu, Z. & Chen, B. Significant improvement in Mn₂O₃ transition metal oxide electrical conductivity via high pressure. *Sci. Rep.* **7**, 44078 (2017).
 56. Tiedemann, W. & Newman, J. Double-Layer Capacity Determination of Porous Electrodes. *J. Electrochem. Soc.* **122**, 70 (1965).
 57. Srinivasan, V. & Weidner, J. W. Mathematical Modeling of Electrochemical Capacitors. *J. Electrochem. Soc.* **146**, 1650–1658 (1999).
 58. Pillay, B. & Newman, J. The Influence of Side Reactions on the Performance of Electrochemical Double-Layer Capacitors. *J. Electrochem. Soc.* **143**, 1806–1814 (1996).
 59. Lin, C., Ritter, J. A., Popov, B. N. & White, R. E. A Mathematical Model of an Electrochemical Capacitor with Double-Layer and Faradaic Processes. *J. Electrochem. Soc.* **146**, 3168–3175 (1999).
 60. Kim, H. & Popov, B. N. A Mathematical Model of Oxide/Carbon Composite Electrode for Supercapacitors. *J. Electrochem. Soc.* **150**, A1153 (2003).
 61. Lin, C., Popov, B. N. & Ploehn, H. J. Modeling the Effects of Electrode Composition and Pore Structure on the Performance of Electrochemical Capacitors. *J. Electrochem. Soc.* **149**, A167–A175 (2002).
 62. Girard, H. L., Wang, H., D'Entremont, A. L. & Pilon, L. Enhancing Faradaic Charge

- Storage Contribution in Hybrid Pseudocapacitors. *Electrochim. Acta* **182**, 639–651 (2015).
63. Hao, C., Wang, X., Yin, Y. & You, Z. Modeling and Simulation of a Lithium Manganese Oxide/Activated Carbon Asymmetric Supercapacitor. *J. Electron. Mater.* **45**, 515–526 (2016).
 64. Staser, J. A. & Weidner, J. W. Mathematical Modeling of Hybrid Asymmetric Electrochemical Capacitors. *J. Electrochem. Soc.* **161**, E3267–E3275 (2014).
 65. Sikha, G. & Popov, B. N. Modeling and application studies of an electrochemical hybrid system. *Funct. Mater. Lett.* **1**, 155–165 (2008).
 66. Sikha, G., White, R. E. & Popov, B. N. A Mathematical Model for a Lithium-Ion Battery/Electrochemical Capacitor Hybrid System. *J. Electrochem. Soc.* **152**, A1682 (2005).
 67. Aghamirzaie, N., Esfahanian, V., Jafari, A. & Dalakeh, M. T. Mathematical Modeling of Ultra-Battery. *J. Electrochem. Soc.* **166**, A3660–A3667 (2019).
 68. Mei, B.-A., Li, B., Lin, J., Pilon, L. & Samuelli, H. Multidimensional Cyclic Voltammetry Simulations of Pseudocapacitive Electrodes with a Conducting Nanorod Scaffold. *J. Electrochem. Soc.* **164**, 3237–3252 (2017).
 69. Dai, K., Wang, X., Lv, W. & You, Z. Study on a planar interdigitated MEMS supercapacitor using modeling and simulation method. *Key Eng. Mater.* **645**, 513–516 (2015).
 70. Kashkooli, A. G., Farhad, S., Chabot, V., Yu, A. & Chen, Z. Effects of structural design on the performance of electrical double layer capacitors. *Appl. Energy* **138**, 631–639 (2015).
 71. Ike, I. S., Iyuke, S. E. & Kalu, E. E. Comparative Studies of Solutions of Homogeneous Electrochemical Capacitors Models. *J. Energy Storage* **35**, 102221 (2021).
 72. Ike, I. S., Sigalas, I. & Iyuke, S. E. The influences of operating conditions and design configurations on the performance of symmetric electrochemical capacitors. *Phys. Chem. Chem. Phys.* **18**, 28626–28647 (2016).
 73. Wang, H. & Pilon, L. Accurate Simulations of Electric Double Layer Capacitance of Ultramicroelectrodes. *J. Phys. Chem. C* **115**, 16711–16719 (2011).

74. Kadyk, T. & Eikerling, M. Charging Mechanism and Moving Reaction Fronts in a Supercapacitor with Pseudocapacitance. *J. Electrochem. Soc.* **161**, A239–A246 (2014).
75. Faranda, R., Gallina, M. & Son, D. T. A new simplified model of Double-Layer Capacitors. in *2007 International Conference on Clean Electrical Power* 706–710 (2007). doi:10.1109/ICCEP.2007.384288
76. Dunn, D. & Newman, J. Predictions of Specific Energies and Specific Powers of Double-Layer Capacitors Using a Simplified Model. *J. Electrochem. Soc.* **147**, 820–830 (2000).
77. Hao, C., Wang, X., Yin, Y. & You, Z. Modeling and Simulation of a Lithium Manganese Oxide/ Activated Carbon Asymmetric Supercapacitor. *J. Electron. Mater.* **45**, (2016).
78. Nilson, R. H., Brumbach, M. T. & Bunker, B. C. Modeling the Electrochemical Impedance Spectra of Electroactive Pseudocapacitor Materials. *J. Electrochem. Soc.* **158**, A678 (2011).
79. Somasundaram, K., Birgersson, E. & Mujumdar, A. S. Analysis of a Model for an Electrochemical Capacitor. *J. Electrochem. Soc.* **158**, A1220 (2011).
80. Chang, J. H., Dawson, F. P. & Lian, K. A first principles approach to develop a dynamic model of electrochemical capacitors. in *2010 International Power Electronics Conference - ECCE Asia -, IPEC 2010* 2382–2389 (2010). doi:10.1109/IPEC.2010.5543632
81. Verbrugge, M. W. & Liu, P. Microstructural Analysis and Mathematical Modeling of Electric Double-Layer Supercapacitors. *J. Electrochem. Soc.* **152**, D79 (2005).
82. Mundy, A. & Plett, G. L. Reduced-order physics-based modeling and experimental parameter identification for non-Faradaic electrical double-layer capacitors. *J. Energy Storage* **7**, 167–180 (2016).
83. Formhals, A. Process and apparatus for preparing artificial threads. 1–3 (1934).
84. Bhardwaj, N. & Kundu, S. C. Electrospinning: A fascinating fiber fabrication technique. *Biotechnol. Adv.* **28**, 325–347 (2010).
85. Skinner, J. L., Andriolo, J. M., Murphy, J. P. & Ross, B. M. Electrospinning for nano-to mesoscale photonic structures. *Nanophotonics* **6**, 765–787 (2017).
86. Han, T., Yarin, A. L. & Reneker, D. H. Viscoelastic electrospun jets: Initial stresses and elongational rheometry. *Polymer (Guildf)*. **49**, 1651–1658 (2008).
87. Wei, K., Kim, H.-R., Kim, B.-S. & Kim, I.-S. Electrospun Metallic Nanofibers Fabricated

- by Electrospinning and Metallization. in *Nanofibers - Production, Properties and Functional Applications* (ed. Lin, T.) 117–133 (InTech, 2011). doi:10.5772/24594
88. Chen, S. *et al.* Polymeric Nanosprings by Bicomponent Electrospinning. *Macromol. Mater. Eng.* **294**, 265–271 (2009).
 89. Lee, K. H., Kim, H. Y., Bang, H. J., Jung, Y. H. & Lee, S. G. The change of bead morphology formed on electrospun polystyrene fibers. *Polymer (Guildf)*. **44**, 4029–4034 (2003).
 90. Dror, Y. *et al.* One-Step Production of Polymeric Microtubes by Co-electrospinning. *Small* **3**, 1064–1073 (2007).
 91. Nezarati, R. M., Eifert, M. B. & Cosgriff-Hernandez, E. Effects of humidity and solution viscosity on electrospun fiber morphology. *Tissue Eng. - Part C Methods* **19**, 810–819 (2013).
 92. Huang, L., Nagapudi, K., Apkarian, P. R. & Chaikof, E. L. Engineered collagen - PEO nanofibers and fabrics. *J. Biomater. Sci. Polym. Ed.* **12**, 979–993 (2001).
 93. Zhao, Z. *et al.* Preparation and properties of electrospun poly(vinylidene fluoride) membranes. *J. Appl. Polym. Sci.* **97**, 466–474 (2005).
 94. Jiang, H., Fang, D., Hsiao, B. S., Chu, B. & Chen, W. Optimization and Characterization of Dextran Membranes Prepared by Electrospinning. *Biomacromolecules* **5**, 326–333 (2004).
 95. Demir, M. M., Yilgor, I., Yilgor, E. & Erman, B. Electrospinning of polyurethane fibers. *Polymer (Guildf)*. **43**, 3303–3309 (2002).
 96. Jun, Z., Hou, H., Schaper, A., Wendorff, J. H. & Greiner, A. Poly-L-lactide nanofibers by electrospinning - Influence of solution viscosity and electrical conductivity on fiber diameter and fiber morphology. *E-Polymers* **3**, 1–9 (2003).
 97. Larrondo, L. & Manley, R. S. J. Electrostatic fiber spinning from polymer melts. III. Electrostatic deformation of a pendant drop of polymer melt. *J. Polym. Sci. Polym. Phys. Ed.* **19**, 933–940 (1981).
 98. Demir, M. M., Yilgor, I., Yilgor, E. & Erman, B. Electrospinning of polyurethane fibers. *Polymer (Guildf)*. **43**, 3303–3309 (2002).
 99. Zhang, C., Yuan, X., Wu, L., Han, Y. & Sheng, J. Study on morphology of electrospun

- poly(vinyl alcohol) mats. *Eur. Polym. J.* **41**, 423–432 (2005).
100. Reneker, D. H. & Chun, I. Nanometre diameter fibres of polymer, produced by electrospinning. *Nanotechnology* **7**, 216 (1996).
 101. Zong, X. *et al.* Structure and process relationship of electrospun bioabsorbable nanofiber membranes. *Polymer (Guildf)*. **43**, 4403–4412 (2002).
 102. Yuan, X., Zhang, Y., Dong, C. & Sheng, J. Morphology of ultrafine polysulfone fibers prepared by electrospinning. *Polym. Int.* **53**, 1704–1710 (2004).
 103. Mit-uppatham, C., Nithitanakul, M. & Supaphol, P. Ultrafine Electrospun Polyamide-6 Fibers: Effect of Solution Conditions on Morphology and Average Fiber Diameter. *Macromol. Chem. Phys.* **205**, 2327–2338 (2004).
 104. Reneker, D. H. & Chun, I. Nanometre diameter fibres of polymer, produced by electrospinning. *Nanotechnology* **7**, 216 (1996).
 105. Beachley, V., Katsanevakis, E., Zhang, N. & Wen, X. Highly Aligned Polymer Nanofiber Structures: Fabrication and Applications in Tissue Engineering. in *Biomedical Applications of Polymeric Nanofibers* (eds. Jayakumar, R. & Nair, S.) 171–212 (Springer-Verlag Berlin Heidelberg, 2012). doi:10.1007/978-3-642-27148-9
 106. Chen, D., Wang, R., Tjiu, W. W. & Liu, T. High performance polyimide composite films prepared by homogeneity reinforcement of electrospun nanofibers. *Compos. Sci. Technol.* **71**, 1556–1562 (2011).
 107. Beilke, M. C., Zewe, J. W., Clark, J. E. & Olesik, S. V. Aligned electrospun nanofibers for ultra-thin layer chromatography. *Anal. Chim. Acta* **761**, 201–208 (2013).
 108. Aminu, T. Q., Brockway, M. C., Skinner, J. L. & Bahr, D. F. Well-adhered copper nanocubes on electrospun polymeric fibers. *Nanomaterials* **10**, 1982 (2020).
 109. Fennessey, S. F. & Farris, R. J. Fabrication of aligned and molecularly oriented electrospun polyacrylonitrile nanofibers and the mechanical behavior of their twisted yarns. *Polymer (Guildf)*. **45**, 4217–4225 (2004).
 110. Li, D., Wang, Y. & Xia, Y. Electrospinning Nanofibers as Uniaxially Aligned Arrays and Layer-by-Layer Stacked Films. *Advanced Materials* 361–366 (2004). Available at: <https://onlinelibrary.wiley.com/doi/epdf/10.1002/adma.200306226>. (Accessed: 27th January 2020)

111. He, G., Song, Y., Chen, S. & Wang, L. Porous carbon nanofiber mats from electrospun polyacrylonitrile/polymethylmethacrylate composite nanofibers for supercapacitor electrode materials. *J. Mater. Sci.* **53**, 9721–9730 (2018).
112. Cheng, Y. *et al.* Flexible and cross-linked N-doped carbon nanofiber network for high performance freestanding supercapacitor electrode. *Nano Energy* **15**, 66–74 (2015).
113. Vidhyadharan, B. *et al.* High performance supercapacitor electrodes from electrospun nickel oxide nanowires. *J. Alloys Compd.* **610**, 143–150 (2014).
114. Kim, C. H. & Kim, B. H. Zinc oxide/activated carbon nanofiber composites for high-performance supercapacitor electrodes. *J. Power Sources* **274**, 512–520 (2015).
115. Inagaki, M., Yang, Y. & Kang, F. Carbon nanofibers prepared via electrospinning. *Adv. Mater.* **24**, 2547–2566 (2012).
116. Schneider, C. A., Rasband, W. S. & Eliceiri, K. W. NIH Image to ImageJ: 25 years of image analysis. *Nat. Methods* **9**, 671–675 (2012).
117. Core Team, R. *R: A language and environment for statistical computing*. (R Foundation for Statistical Computing, 2021).
118. Soetaert, K., Petzoldt, T. & Setzer, R. W. Solving Differential Equations in R: Package deSolve. *J. Stat. Softw.* **33**, 1–25 (2010).
119. Brockway, M. C. & Skinner, J. L. Variable Phase and Electrochemical Capacitance of Electrospun MnOx Fibers Via Controlled Calcination. *MRS Adv.* **4**, 2383–2390 (2019).
120. Tschöpe, A. & Birringer, R. Grain Size Dependence of Electrical Conductivity in Polycrystalline Cerium Oxide. *J. Electroceramics* **7**, 169–177 (2001).
121. Mayadas, A. F. & Shatzkes, M. Electrical-resistivity model for polycrystalline films: The case of arbitrary reflection at external surfaces. *Phys. Rev. B* **1**, 1382–1389 (1970).
122. Liang, J., Bu, L.-T., Cao, W.-G., Chen, T. & Cao, Y.-C. Facile fabrication of coaxial-cable like Mn₂O₃ nanofiber by electrospinning: Application as electrode material for supercapacitor. *J. Taiwan Inst. Chem. Eng.* **65**, 584–590 (2016).
123. Nagarajan, N., Humadi, H. & Zhitomirsky, I. Cathodic electrodeposition of MnOx films for electrochemical supercapacitors. *Electrochim. Acta* **51**, 3039–3045 (2006).
124. Gu, X. *et al.* General Synthesis of MnOx (MnO₂, Mn₂O₃, Mn₃O₄, MnO) Hierarchical Microspheres as Lithium-ion Battery Anodes. *Electrochim. Acta* **184**, 250–256 (2015).

125. Nathan, T., Cloke, M. & Prabakaran, S. R. S. Electrode Properties of Mn₂O₃ Nanospheres Synthesized by Combined Sonochemical/Solvothermal Method for Use in Electrochemical Capacitors. *J. Nanomater.* **2008**, Article 81, 8 pages (2008).
126. Chen, W., Fan, Z., Gu, L., Bao, X. & Wang, C. Enhanced capacitance of manganese oxide via confinement inside carbon nanotubes. *Chem. Commun.* **46**, 3905 (2010).
127. Lee, E., Lee, T. & Kim, B.-S. Electrospun nanofiber of hybrid manganese oxides for supercapacitor: Relevance to mixed inorganic interfaces. *J. Power Sources* **255**, 335–340 (2014).
128. Devaraj, S. & Munichandraiah, N. Effect of Crystallographic Structure of MnO₂ on Its Electrochemical Capacitance Properties. *J. Phys. Chem. C* **112**, 4406–4417 (2008).
129. Dong, Y. *et al.* Simple hydrothermal preparation of α-, β-, and γ-MnO₂ and phase sensitivity in catalytic ozonation. *RSC Adv.* **4**, 39167 (2014).
130. Sheng, Q., Sun, J., Wang, Q., Wang, W. & Wang, H. S. On the onset of surface condensation: Formation and transition mechanisms of condensation mode. *Sci. Rep.* **6**, 30764 (2016).
131. Khandekar, S. & Muralidhar, K. *Dropwise Condensation on Inclined Textured Surfaces.* (SpringerBriefs in Applied Science and Technology, 2014).
132. Chen, Z. *et al.* 3D printing of ceramics: A review. *Journal of the European Ceramic Society* **39**, 661–687 (2019).
133. Kolathodi, M. S., Voigt, V. & Singh, G. Beaded Mn₂O₃ Nanofibers by Electrospinning for Supercapacitor Applications. *Journal Mater. Chem. A* **4**, 7883–7891 (2016).
134. Vadiyar, M. M. *et al.* Contact angle measurements: A preliminary diagnostic tool for evaluating the performance of ZnFe₂O₄ nano-flake based supercapacitors. *Chem. Commun.* **52**, 2557–2560 (2016).
135. Liu, T., Wang, K., Chen, Y., Zhao, S. & Han, Y. Dominant role of wettability in improving the specific capacitance. *Green Energy Environ.* **4**, 171–179 (2019).
136. Julien, C. M. & Mauger, A. Nanostructured MnO₂ as electrode materials for energy storage. *Nanomaterials* **7**, 396 (2017).
137. Chen, S., Liu, F., Xiang, Q., Feng, X. & Qiu, G. Synthesis of Mn₂O₃ microstructures and their energy storage ability studies. *Electrochim. Acta* **106**, 360–371 (2013).

138. Pal, P., Giri, A. K., Mahanty, S. & Panda, A. B. Morphology mediated tailoring the performance of porous nanostructured Mn₂O₃ as anode material. *CrystEngComm* **16**, 10560–10568 (2014).
139. Li, W. *et al.* Facile synthesis of porous Mn₂O₃ nanocubics for high-rate supercapacitors. *Electrochim. Acta* **157**, 108–114 (2015).
140. Jovic, V. D. Determination of the correct value of Cdl from the impedance results fitted by the commercially available software. *Gamry Application Notes* (2021). Available at: <https://www.gamry.com/application-notes/EIS/correct-value-of-cdl/>. (Accessed: 13th October 2021)
141. Diffusion. *Gamry Framework* (2021). Available at: <https://www.gamry.com/FrameworkHelp/HTML5-Tripane-AudienceA/Content/EIS/Theory/PhysicalElectrochemistryandCircuitElements/Diffusion.htm>. (Accessed: 13th October 2021)
142. Basics of Electrochemical Impedance Spectroscopy. *Gamry Application Notes* (2021). Available at: <https://www.gamry.com/application-notes/EIS/basics-of-electrochemical-impedance-spectroscopy/>. (Accessed: 13th October 2021)
143. Guidelli, R. *et al.* Defining the transfer coefficient in electrochemistry: An assessment (IUPAC Technical Report). *Pure Appl. Chem.* **86**, 245–258 (2014).
144. Iamprasertkun, P. *et al.* Charge storage mechanisms of manganese oxide nanosheets and N-doped reduced graphene oxide aerogel for high-performance asymmetric supercapacitors. *Nat. Publ. Gr.* **6**, 37560 (2016).
145. Jow, T. R. & Zheng, J. P. Electrochemical Capacitors Using Hydrous Ruthenium Oxide and Hydrogen Inserted Ruthenium Oxide. *J. Electrochem. Soc.* **145**, 49–52 (1998).
146. Geller, S. Structure of α -Mn₂O₃, (Mn_{0.983}Fe_{0.017})₂O₃ and (Mn_{0.37}Fe_{0.63})₂O₃ and relation to magnetic ordering. *Acta Crystallogr. Sect. B Struct. Crystallogr. Cryst. Chem.* **27**, 821–828 (1971).
147. Pal, B., Yang, S., Ramesh, S., Thangadurai, V. & Jose, R. Electrolyte selection for supercapacitive devices: A critical review. *Nanoscale Adv.* **1**, 3807–3835 (2019).
148. Farsi, H. & Gobal, F. A mathematical model of nanoparticulate mixed oxide pseudocapacitors; Part I: Model description and particle size effects. *J. Solid State Electrochem.* **13**, 433–443 (2009).

149. Farsi, H. & Gobal, F. Theoretical analysis of the performance of a model supercapacitor consisting of metal oxide nano-particles. *J Solid State Electrochem* **11**, 1085–1092 (2007).
150. Subramanian, V. R., Devan, S. & White, R. E. An approximate solution for a pseudocapacitor. *J. Power Sources* **135**, 361–367 (2004).
151. Devaraj, S. & Munichandraiah, N. High Capacitance of Electrodeposited MnO₂ by the Effect of a Surface-Active Agent. *Electrochem. Solid-State Lett.* **8**, A373–A377 (2005).
152. Zhu, M., Wang, Y., Meng, D., Qin, X. & Diao, G. Hydrothermal Synthesis of Hematite Nanoparticles and Their Electrochemical Properties. *J. Phys. Chem. C* **116**, 16276–16285 (2012).
153. Kim, Y. J., Gao, Y. & Chambers, S. A. Selective growth and characterization of pure, epitaxial α -Fe₂O₃(0001) and Fe₃O₄(001) films by plasma-assisted molecular beam epitaxy. *Surf. Sci.* **371**, 358–370 (1997).
154. Liu, Z. *et al.* Facile synthesis of homogeneous core-shell Co₃O₄ mesoporous nanospheres as high performance electrode materials for supercapacitor. *J. Alloys Compd.* **774**, 137–144 (2019).
155. Beg, S. & Varshney, P. Study of electrical conductivity changes and phase transitions in Co₃O₄ doped ZrO₂. *Phase Transitions* **80**, 867–873 (2007).
156. Zhang, Y. *et al.* Three-dimensional porous V₂O₅ hierarchical spheres as a battery-type electrode for a hybrid supercapacitor with excellent charge storage performance. *Dalt. Trans.* **46**, 15048–15058 (2017).
157. Honma, K., Yoshinaka, M., Hirota, K. & Yamaguchi, O. Fabrication, Microstructure and Electrical Conductivity of V₂O₅ Ceramics. *Mater. Res. Bull.* **31**, 531–537 (1996).
158. Shinde, P. A. *et al.* Temperature dependent surface morphological modifications of hexagonal WO₃ thin films for high performance supercapacitor application. *Electrochim. Acta* **224**, 397–404 (2017).
159. Al-Mohammad, A. Microstructural analysis and electrical conductivity of hexagonal WO₃ thin films during annealing. *phys. stat. sol.* **205**, 2880–2885 (2008).
160. Jeong, Y. U. & Manthiram, A. Amorphous Tungsten Oxide/Ruthenium Oxide Composites for Electrochemical Capacitors. *J. Electrochem. Soc.* **148**, A189 (2001).
161. Kadyk, T. & Eikerling, M. Charging Mechanism and Moving Reaction Fronts in a

- Supercapacitor with Pseudocapacitance. *J. Electrochem. Soc.* **161**, A239–A246 (2014).
162. Lu, W., Wang, X., Li, X., Yin, Y. & You, Z. Modeling and simulating a microelectromechanical system microsupercapacitor. *Proc. Inst. Mech. Eng. Part N J. Nanoeng. Nanosyst.* **228**, 93–97 (2014).

6. Appendix A

Table V: Areal capacitance values of the nineteen standards tested, as described in the DOE table in the Experimental section. Each reported value is the average of three samples prepared for each standard.

| Standard | 25 mV/s ($\mu\text{F}/\text{cm}^2$) | 50 mV/s ($\mu\text{F}/\text{cm}^2$) | 100 mV/s ($\mu\text{F}/\text{cm}^2$) | 200 mV/s ($\mu\text{F}/\text{cm}^2$) |
|----------|--|--|---|---|
| 1 | 235.4 | 151.2 | 114.3 | 92.5 |
| 2 | 173.9 | 124.3 | 134.9 | 82.2 |
| 3 | 129.0 | 85.3 | 62.0 | 48.1 |
| 4 | 195.6 | 134.9 | 109.1 | 91.0 |
| 5 | 219.8 | 141.3 | 105.8 | 84.5 |
| 6 | 234.2 | 144.0 | 114.3 | 92.1 |
| 7 | 68.0 | 88.7 | 72.2 | 55.0 |
| 8 | 131.2 | 100.6 | 87.0 | 72.8 |
| 9 | 97.8 | 86.8 | 82.5 | 69.3 |
| 10 | 225.5 | 156.9 | 117.0 | 90.5 |
| 11 | 229.5 | 134.6 | 102.4 | 83.1 |
| 12 | 268.2 | 118.7 | 93.0 | 74.7 |
| 13 | 389.4 | 267.8 | 218.3 | 183.6 |
| 14 | 560.0 | 289.3 | 308.6 | 239.4 |
| 15 | 279.5 | 164.2 | 127.7 | 102.8 |
| 16 | 203.7 | 130.2 | 97.2 | 76.3 |
| 17 | 248.7 | 156.6 | 116.5 | 92.1 |
| 18 | 321.2 | 168.6 | 145.2 | 123.4 |
| 19 | 244.0 | 156.4 | 128.4 | 102.5 |

Table VI: Assumed model values used for comparison of various metal oxide electrode materials. Separator porosity and thickness are taken from measured values; all other are based on the assumptions made in the exemplary model by Lin, et al.⁵⁹

| Parameter | Assumed Value |
|---|-----------------|
| Exchange current density for Faradaic Reaction, i_0 (A/cm^2) | 0 |
| Anodic transfer coefficient of Faradaic reaction, α_a | 0.5 |
| Cathodic transfer coefficient of Faradaic reaction, α_c | 0.5 |
| Equilibrium potential for the Faradaic reaction at positive electrode, U_{pos} (V) | $0.5(1+\theta)$ |
| Equilibrium potential for the Faradaic reaction at negative electrode, U_{neg} (V) | 0.50 |
| Separator Porosity, ϵ_s | 0.661 |
| Separator thickness, L_s (cm) | 0.042 |

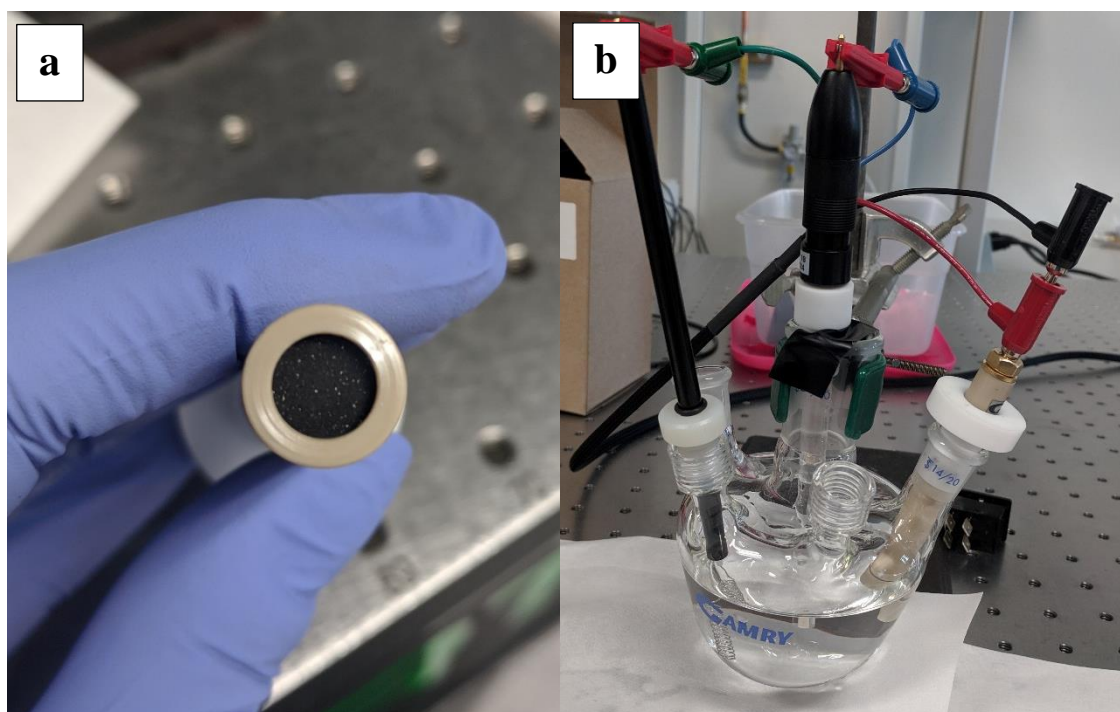


Figure 54: Experimental setup for testing composite electrodes in three-electrode cell. (a) Composite electrode in electrode holder with defined area. (b) Fully assembled three-electrode cell with composite working electrode, Ag/AgCl reference electrode, and Pt wire counter electrode.

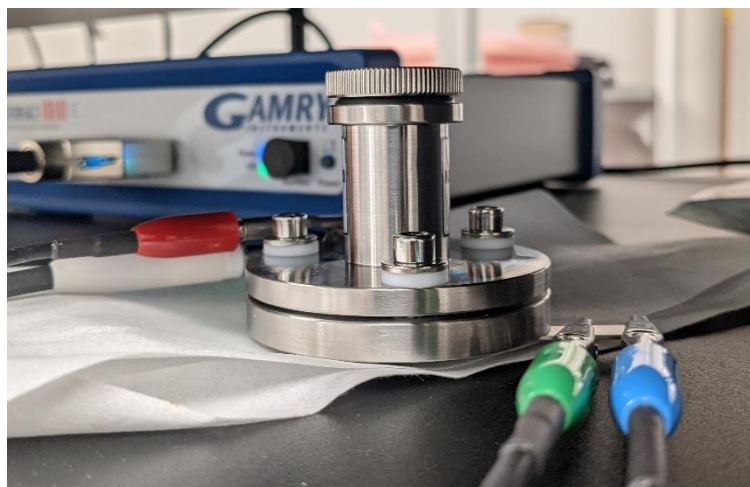


Figure 55: Two-electrode split cell used for testing freestanding web electrodes. Blue and green leads are working electrode and working sense, respectively, and red and white leads are counter and reference leads.

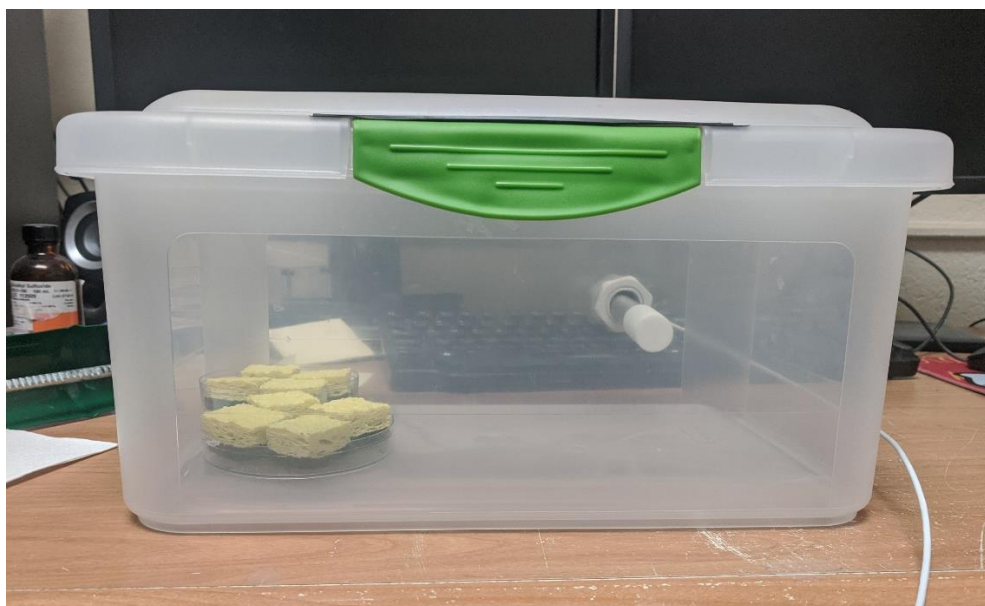


Figure 56: Vapor chamber used for post-processing electrospun fiber mats. Absorbent substrate is used to increase relative humidity, which is monitored with the humidity and temperature sensor.



Figure 57: Manual hot press used for post-processing of electrospun fibers. To tighten uniformly, the press is turned 1/4 rotation after first contact with the sample.



Figure 58: Tube furnace setup used for calcination in oxygen environment. After flowing through the furnace, gases are flowed through a bubbler tube to prevent backflow into the tube and maintain pure oxygen atmosphere. For reactions in air, the bubbler is removed and the flange vents are opened to the ambient atmosphere.

7. Appendix B: R Code for Electrospun Fiber Modeling

```

library(deSolve)

set_vars <- list(
  ## constants that will not change at all
  La = 6.02E+23, ## Avogadro's Number
  Far = 96485, ## Faraday Constant
  R = 8.3143, ## Ideal Gas Constant
  Temp = 298.15, ## Temperature
  f = Far / (R * Temp), ## F/RT
  A = 1.767145868, ## Electrode Area of a 15 mm electrode (cm2)
  ## measured and set values. User input and any of these could
  ##be varied to look at their effect on discharge.
  xd = 112e-7, ##measured diameter (cm)
  porxd = 0.83713, ##measured porosity
  Lxd = 4.076e-5, ##thickness (cm)
  es = 0.661, ##separator porosity
  Ls = 0.042, ##separator thickness (cm)
  Cd = 1.07e-2, ##DL capacitance per unit SA
  h = 9.41e-8, ##length of surface lattice (cm)
  sig = 0.001, ## matrix conductivity (S/cm)
  ko = 0.0667, ##electrolyte conductivity (S/cm)
  Vo = 0.5, ##initial voltage per electrode
  rho = 4.5, ##matrix density (g/cm3)
  dimicell = 5, ##current density (A/g)
  dimicellB = 1, ##areal density (A/cm2)
  io = seq(1e-7, 1e-6, length = 10), ##exchange current density (A/cm2)
  ac = 0.7674, ##cathodic transfer coefficient
  aa = 0.2326, ##anodic transfer coefficient
  D = seq(100e-7, 250e-7, length = 10), ##Fiber diameter (cm)
  Qred = 0 #charge of a fully reduced electrode
)

set_df <- expand.grid(set_vars)
# Derived Values
der_val <- function(La, Far, R, Temp, f, A,
  xd, porxd, Lxd,
  es, Ls,
  Cd, h, sig, ko, Vo,
  rho, dimicell, dimicellB,
  io, ac, aa, D, Qred) {
  l <- (1 - porxd) * (4 / pi) / ((xd)^2) ## constant length of deposited
  fiber
  Dpor0 <- sqrt(4 / (pi * l)) ##diameter where porosity is zero. Not used in
  the model but is
  ##useful to determine fiber range of interest.
  L <- D * (Lxd / 1.12e-5) ##electrode thickness
  por <- 1 - ((pi / 4) * (D^2) * l) ## porosity
  Sv <- 4 * (1 - por) / D ##surface area per unit volume of fiber
}

```

```

Qox <- Sv * 0.371 * Far / ((h^2) * La) ##charge of a fully oxidized
electrode
kp <- ko * (por^1.5) #electrolyte conductivity in the electrode pores
ks <- ko * (es^1.5) # electrolyte conductivity in the separator pores
Tau <- Sv * Cd * L^2 * 1 * ((1 / sig) + (1 / kp)) #time constant
icell <- dimicell * (1 - por) * L * A * rho ## constant A/g current
density
icellB <- dimicellB * A * L * Sv ## constant A/cm2 current density

# Computed values for ODE solving
icell_L_kp <- icell * L / kp
icell_L_sig <- icell * L / sig
coef1 <- Sv * io / (Qox - Qred)
coef2 <- Tau * io / Cd
aaf <- aa * f
acf <- ac * f
return(c(1, Dpor0, L, por, Sv, Qox, kp, ks, Tau, icell, icellB,
icell_L_kp, icell_L_sig, coef1, coef2, aaf, acf))
}

der_df <- as.data.frame(t(do.call(mapply, c(der_val, unname(set_df)))))
colnames(der_df) <- c("1", "Dpor0", "L", "por", "Sv", "Qox", "kp",
"ks", "Tau", "icell", "icellB",
"icell_L_kp", "icell_L_sig",
"coef1", "coef2", "aaf", "acf")

values_df <- cbind(set_df, der_df)

BVmod <- function(time, state, parms, N, dx) {
  with(as.list(parms), {
    E <- state[1:N]
    U <- state[-(1:N)]

    BV <- exp(aaf * (E - 0.371 * (U))) -
      exp(-acf * (E - 0.371 * (U - 0.4061)))

    FluxE <- diff(c(
      (E[1] - icell_L_sig),
      E, (E[N] + icell_L_kp)
    )) / dx
    FluxU <- diff(c(U[1], U, U[N])) / dx

    ## Eqn 8 and 12

    dE <- (diff(FluxE) / dx - (coef2 * BV)) / Tau # dE/dt, Eqn 12
    dU <- coef1 * BV # dU/dt, Eqn 8

    return(list(c(dE, dU)))
  })
}

```

```

# Initial and Boundary Conditions
R <- 1
N <- 50
dx <- R / N
Vo <- 0.5
timestep <- 0.1

yini <- rep(0, 2 * N)
yini[1:N] <- 2 * Vo
yini[(N + 1):(2 * N)] <- 1 ## Leave this ALONE!
times <- seq(0, 3, by = timestep)
## this time step needs to stay small or it gives NaN!

out <- data.frame()
for (i in 1:nrow(values_df)) {
  out <- rbind(
    out,
    cbind(
      ode(
        y = yini,
        times = times,
        func = BVmod,
        parms = values_df[i, ],
        N = N,
        dx = dx
      ),
      do.call("rbind", replicate(length(times), values_df[i,], simplify =
FALSE))
    )
  )
}
# Statisticians, and by extension most R functions, like to work with data
in a "long" format where each
# observation is its own row. The following code uses functions from the
"tidyverse" to convert the
# desolver output to a nicer format.
library(tidyverse)
output <- out %>%
  pivot_longer(
    2:(2*N + 1),
    names_to = "position",
    values_to = "value"
  ) %>%
  mutate(
    position = as.numeric(position),
    type = case_when(
      position > N ~ "E",
      position <= N ~ "U"
    )
  )
)

```

```
# Plots are a bit more clear to make using GGplot which is also a part of
the tidyverse
output
output %>%
  filter(position == 2) %>%
  mutate(D = factor(D)) %>%
  ggplot(aes(
    x = time,
    y = value,
    color = D,
    group = D
  )) +
  geom_line() +
  facet_wrap(~io)
```